THE UNIVERSITY OF CHICAGO

CHARACTERIZATION OF SPIN PROPERTIES IN NOVEL SILICON CARBIDE DEFECTS AND MATERIAL PLATFORMS

A DISSERTATION SUBMITTED TO
THE FACULTY OF THE PRITZKER SCHOOL OF MOLECULAR ENGINEERING
IN CANDIDACY FOR THE DEGREE OF
DOCTOR OF PHILOSOPHY

BY
CHRISTINA WICKER

CHICAGO, ILLINOIS
DECEMBER 2024

TABLE OF CONTENTS

LIST OF FIGURES

LIST OF TABLES

ACKNOWLEDGMENTS

I would like to thank Prof. David Awschalom for letting me transfer to his lab group during my fifth year of the PhD.

I am also thankful to Joseph Heremans, Scientist at Argonne National Laboratory. Without his help it is unlikely that I would have compiled enough content for a dissertation in two years.

I would also like to thank my committee members for their support. In particular, I appreciate the advice on my career I received from David, Joe, and Supratik Guha. I also enjoyed smooth and efficient collaboration with Supratik and Connor Horn, a student in his group, on the spalled films project.

My fellow grad students in the Awschalom lab helped make the PhD an unforgettable experience. I appreciated getting to work with Nolan Bitner on the vanadium T_1 and strain experiments, among a number of other exciting projects in progress. Additionally I am grateful to Cyrus for his help on the spalled film project and his working knowledge of much of the equipment in the lab.

ABSTRACT

Silicon carbide is a crystalline semiconductor with wide availability in the form of commercially produced wafers, due to it's application in the power electronics industry. Silicon carbide has many properties that make it an ideal platform for quantum information science, in particular it is a host to many optically-active spin defects that can be used as qubits. These optically active spin qubits may be used for quantum computing, communication, and sensing, by leveraging silicon carbide's wide electronic band gap, low abundance of nuclear spins, optical transparency, and mature fabrication techniques. Optically active spins in solids consist of crystal point defects, with an electronic or nuclear spin degree of freedom that can be driven by magnetic resonance, and optical transitions that can be used for spin initialization and readout. However, interactions with the surrounding silicon carbide lattice has an influence on qubit operating conditions, control schemes, and host material engineering. Interactions with phonons, spins, charges, strain, and electric and magnetic fields can cause relaxation and decoherence of the qubit's state. However, such interactions can also be used to drive transitions and engineer resonance conditions in the system. This thesis explores how we can use such interactions as a tuning knob for quantum science and technology applications, while minimizing their detrimental effect on quantum states. This thesis focuses on the study of two defects in silicon carbide, the vanadium impurity and the divacancy. Using all-optical methods, we studied the spin-relaxation processes of vanadium at milikelvin temperatures and observed a temperature dependent contribution of the direct or Orbach phonon relaxation processes between 50-1900mK. Furthermore, we characterized the orbital strain susceptibility and predicted the spin-strain susceptibility of the vanadium defect. On the other hand, the divacancy is a well characterized spin defect that can be used to benchmark silicon carbide material environments. We compared the spin T_2, and T_2^* of divacancy defect ensembles in thin films and bulk wafers to benchmark and optimize a novel silicon carbide spalling process.

CHAPTER 1

INTRODUCTION

1.1 Quantum computers, networks, and sensors

Quantum systems have historically been studied to gain insights into fundamental physics. More recent interest has developed around possible quantum technologies that leverage the properties of quantum systems and states to provide an advantage over classical technologies. In particular, quantum two-level systems, or qubits, have been suggested as a means to realize an alternative paradigm of information science, where instead of a binary representation, information is represented as a normalized vector along a continuum of superposed basis states. The main applications suggested for quantum systems are in quantum computing, quantum networking, and quantum sensing [76]. Thus more recent research has emphasized the coherent manipulation of quantum states as well as the individual properties of quantum systems that are suitable for these technologies.

One paradigm that will be discussed in this thesis is the use of optically-active spins in solids as a qubit. Optically active spins can be deployed for the aforementioned applications. For quantum computing we can envision performing quantum logic operations that leverage the coupling between neighboring spins in a crystal. For quantum communication, we can imagine using the optical transitions to entangle remote spins over long distances, and use these entangled states as resources in quantum key distribution and teleportation. For quantum sensing, we have the nanoscale footprint of these atomic systems and susceptibility of the spin state to environmental perturbations that allow us to use the spin as a quantum-advantaged sensor of local degrees of freedom.

Perhaps the most promising application for this system specifically is quantum communication, specifically towards developing *quantum networks*. Quantum networks are poised to shift paradigms of communication, sensing, and computing [40]. A quantum network

is a collection of local quantum information processors, called *quantum nodes* and optical links between them. Instead of conventional bits used for digital information encoding, information is shared across quantum networks in the form of quantum bits or *qubits*. The use of qubits confers certain advantages, such as preventing the cloning of quantum states for unconditional security, but also challenges, such as limiting amplification in lossy optical channels.

One elegant way to use quantum networks is to create long-distance entangled states. Long distance entangled states are particularly useful for teleporting quantum information over long distances. Two possible platforms have emerged for the development of quantum networks. The first consists of free space optical links, where entanglement between remote locations is mediated by satellites. The second is to use the existing global fiber-optic telecommunications infrastructure. Particularly for the fiber-optic case, since single photon quantum states cannot be traditionally amplified, it is necessarily to employ a scheme to create long distance entanglement that is robust to transmission losses.

Long distance entanglement can be created by first creating entanglement between pairs of neighboring quantum nodes. Then, successive *entanglement swapping* operations transfer entanglement in the outermost nodes. In this scheme the nodes may be referred to as *quantum repeaters*. The advantage of this scheme is that photons participating in entanglement generation don't necessarily have to travel long distances in optical fiber, and the creation of entangled states allows for quantum information to be transferred by *quantum teleportation*. Here, optically active spin qubits can be used as a source of single photons that participate in the entanglement process. Furthermore, in this scheme, the entanglement is projected onto the spin state of the defects, for storage and manipulation of the entanglement.

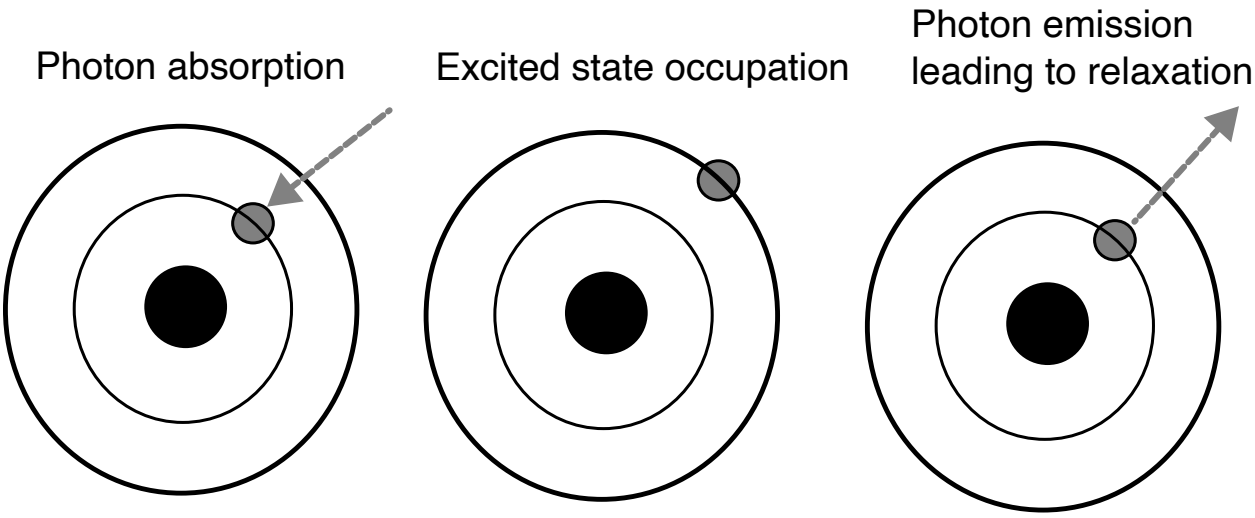

Figure 1.1: Electromagnetic fields can excite electrons to higher energy states in an atom. Conversely, emission of photons can allow electrons to relax to lower energy levels.

1.2 Different types of quantum systems

There are many physical systems currently being studied for quantum information science applications. Here I will overview the classes where two level systems with energetically separated eigenstates form a qubit. In these systems the formation of of a qubit ground state is naturally feasible due to the atomic or atomic-like spacing of energy levels in the system. These include defect qubits, neutral atoms and trapped ions, and superconducting circuits.

At a high level, the operational principle of defect spin qubits and neutral atoms and trapped ions is very similar. That is, the qubit states are defined by the electronic structure of a naturally occurring atomic system, and by sending energy into the system in the form of light or magnetic fields (as shown in Figure 1.1). Electromagnetic fields can excite electrons to higher energy states in an atom. Conversely, emission of photons can allow electrons to relax to lower energy levels. We can use this reshuffling of electrons among different electronic states to perform quantum logic operations.

Fundamentally, a defect qubits consists of an impurity or lattice defect with bound elec-

tronic structure. Generally speaking, for a crystal, it is necessary for the qubit to exist in a material with an electronic bandgap, such as an insulator or semiconductor, otherwise the defect's electrons will not be well localized. The qubit states could be formed by discrete electronic or nuclear spin sub-levels. For example consider the example of a defect with an unpaired 1/2 electron spin, (i.e. the Praseodymium ion in YSO), clearly an electron spin qubit could be formed by applying a magnetic field and taking advantage of the energy gap introduced by the Zeeman effect. In some systems it it not necessary to apply an external field to create an energy gap, one may be formed at zero field due to hyperfine interactions. Qubit states could also be formed by multi-electron systems with higher total spin quantum number. Famous examples include the NV-center in diamond, and the neutral divacancy defect (VV0) in silicon carbide. Qubit states do not necessarily need to consist of a spin; optical sub-levels where the spin is not resolved or remains in a mixed state can also be coherently addressed, as has been shown in the coherent control of optical transitions of rare-earth ions. However coherent control of optical transitions remains difficult due to relatively fast optical dephasing times, and much research is focused on spins.

The capabilities of defect spin qubits are largely determined by their interaction with the surrounding host. In practice the local environment around the defect will be subject to random imperfections in the lattice or even other impurities that can interact with the spin. On the other hand, the existence of a surrounding host for solid-state spin qubits is advantageous in the sense that it enables the fabrication of devices to interface the defects. For semiconducting substrates micro- or nano- structuring might be possible with conventional lithography techniques. Alternatively, one can envision addressing an atom free of these interactions, in vacuum, as is the case with neutral atoms and trapped ions. Neutral atoms may alternatively be referred to as Rydberg atoms. The charged nature of ions allow them to be trapped and manipulated by lasers using electric dipole interactions [57]. Likewise, a neutral atom does not have a natural electric dipole and is excited to a high lying *Rydberg*

state, in order to induce this electric dipole.

In contrast to the case of defect qubits, where transitions are broadened due to the strain or spectral diffusion caused by interaction with the host, the transitions of neutral atoms and trapped ions have extremely narrow transition linewidths. These very long coherence and relaxation times are a significant advantage for these systems. On the other hand, neutral atoms and trapped ions require very stable laser sources to address these narrow optical transitions, as well as UHV to motionally isolate the atoms, leading to technical challenges with scaling the system.

Superconducting circuits used to form qubits are similar to an LC oscillator, except for the additional of Josephson junctions which create nonlinearities in the system and a resultant anharmonicity of the energy structure (that would otherwise be harmonic). A Josephson junction consists of a thin insulator sandwhiched between two superconducting elements [28]. In this sense the level structure is like an *artificial atom*. Superconducting circuits are typically lithographically defined and designed to have resonances below 6 GHz. The most common architectures employ circuit-QED, which is analogous to cavity-QED, where the qubit is coupled to on-chip microwave resonators. Like some spin defect systems, superconducting circuits must be operated at sub-Kelvin temperatures.

1.3 Thesis outline

This thesis discusses the vanadium and divacancy defects in silicon carbide and shows the characterization of vanadium T_1 and divacancy T_2 and T_2^* in spalled silicon carbide films. In this thesis, I first motivate the exploration of optically active spin defects with a discussion of quantum networks. In Chapter 2, I will discuss spin defects, their ideal spin properties, and measurement techniques that can be used to study them. In Chapter 3 I will discuss the electronic structure of transition metal defects in silicon carbide. Relevant to this discussion, I will describe the structure of the silicon carbide lattice, the effects of point

symmetry and the crystal field interaction, and the effects of spin-orbit coupling. In chapter 4, I describe our characterization of the vanadium spin T_1 at milikelvin temperatures. This discussion will include the optical spectroscopy and charge properties of V^{4+} in silicon carbide, measurements of optical spin polarization, readout, and spin relaxation times, and the mechanism driving the defect's temperature dependent spin relaxation. In Chapter 5 I will discuss characterization of the orbital- strain coupling parameters of vanadium in silicon carbide. I describe details of the experimental setup, show the measured orbital strain susceptibilities and modulation of the transition brightness, and present an estimate of the spin-strain coupling based on the orbital results. Chapter 5 discusses the electronic structure of the divacancy defect, including the defect's charge states, spin singlet states, off-resonant optical excitation, and spin properties. In Chapter 6, I describe our efforts to benchmark spalled 4H-SiC films as a qubit host material, including details of the spalling process theory, optimization, and characterization, and the measuremment of divacancy qubit properties in the films. Finally, Chapter 7 concludes with an outlook for the vanadium and divacancy defect systems and spalled film material platform.

CHAPTER 2

SPIN DEFECTS

2.1 Spin relaxation and decoherence

To explore applications of quantum information science with spin defects it is important to understand the interaction rates of the system with the environment and external control fields. Defects in crystalline materials have interactions with the surrounding lattice, spins, and charges, resulting in decay of the quantum state. Whether these decay rates are destructive to the system also depends on the timescale of the experiment as well as the rate at which the qubit can be manipulated. From a quantum science perspective we can generalize these interactions by the relaxation rates, labeled T_1, and decoherence rates T_2, and T_2^*.

For a given application it is necessary to choose a defect with sufficiently long decay rates. However, many tradeoffs exist in terms of host material and operating wavelengths of different defects. Also, practically, what determines a sufficiently long T_2 or T_2^* will be set by the rate of interaction with external fields, which will be determined in part by the electric and magnetic dipole matrix elements between different energy levels. Crystal field interactions with the surrounding atoms determine the local symmetry of the defect, and in conjunction with other terms in the Hamiltonian, they determine the spacing of energy levels and coupling strength and resonance condition with different fields. Furthermore, defects with relatively slow relaxation or long coherence may have these properties as a result of weak coupling to external fields, making them unsuitable for coherent manipulation. It is clear that we cannot use spin defects for quantum applications without a nuanced understanding of the underlying physical properties determined by the defect's interaction with the lattice.

In a quantum two-level system, relaxation processes couple to off-diagonal terms in the Hamiltonian (when expressed in the basis of the energy eigenstates) (See Fig. 2.1). The T_1 relaxation time ultimately imposes a limit on the coherence time T_2. Furthermore, terms

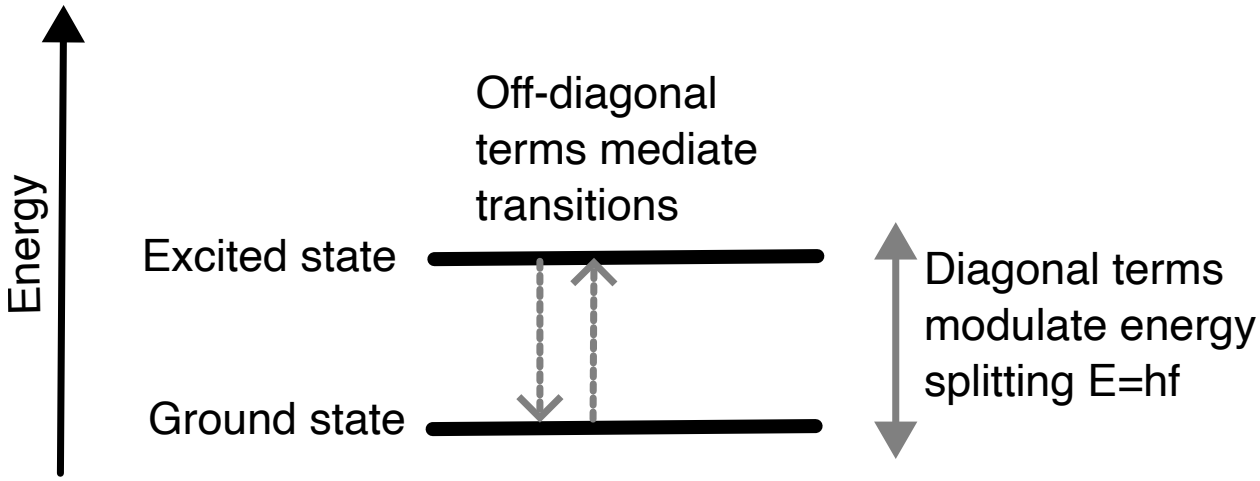

Figure 2.1: In a quantum two-level system, interactions that are diagonal in the energy eigenbasis modulate the energy level splitting, while off-diagonal terms contribute to transitions between the levels.

which are diagonal in the Hamiltonian basis contribute to changing the resonance condition, but can cause decoherence through spectral diffusion.

T_1 of a quantum state describes the energetic relaxation of a quantum state. To clarify notation, we can define T_1 for any two-level quantum system with an energy gap. So we could study the relaxation processes of an optical transition and define a T_1 just as well as we can define the T_1 relaxation of a spin sublevel. However it is common in the field of optically active spin systems, where a defect has both optical and spin transitions that interact, to refer to spin lifetime as T_1, and the optical lifetime by some other labeling such as T_{opt}. However the treatment is analogous. Two possibilities exist for processes that cause T_1 decay in solid-state defects, defect-lattice relaxation, and defect-defect relaxation. In defect-lattice relaxation, energy is transferred from the defect to the lattice. This commonly occurs due to elastic and non-elastic phonon scattering processes. Examples of spin-lattice relaxation processes include the Direct, Raman, and Orbach phonon processes described further in Section 4. In defect-defect relaxation, energy can be directly to a neighboring defect through photon emission and absorption. For spin transitions this could be through a spin-spin flip flop process. For optical transitions, such energy transfer can manifest in

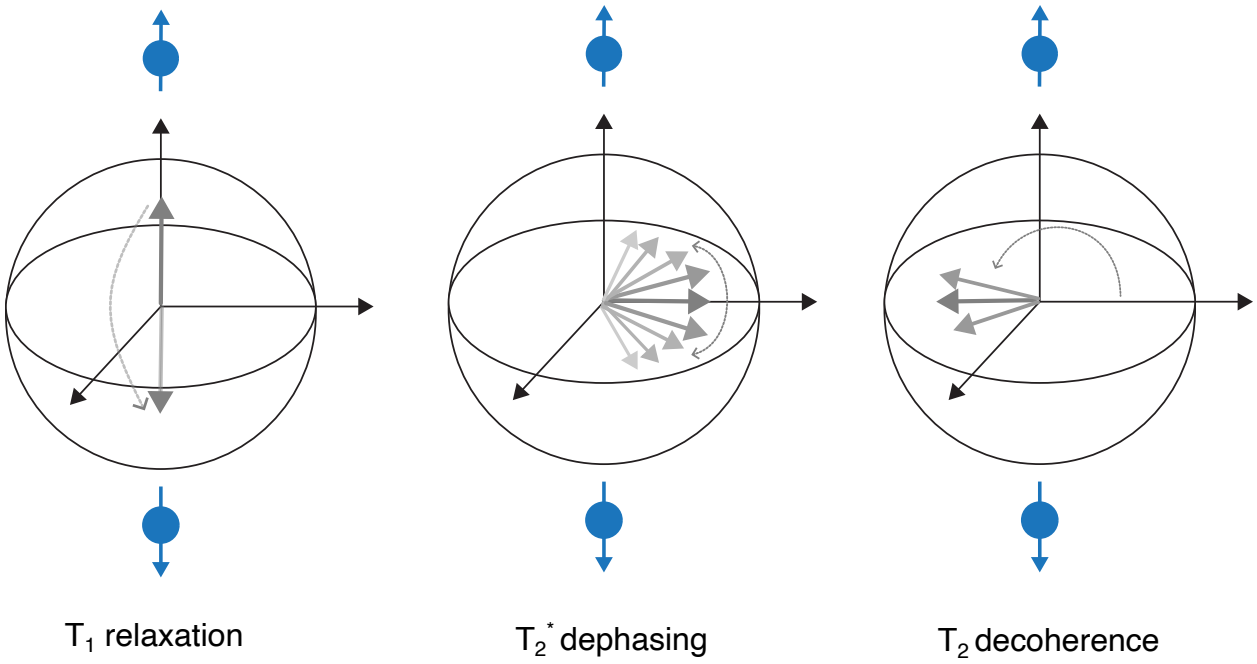

Figure 2.2: Illustration of T_1, T_2^* and T_2 processes on the Bloch sphere.

optical quenching for systems with high densities of neighboring defects.

T_1 is defined as a population relaxation rate. This is different from the rate that the system emits photons, for instance. In general, the the T_1 process will occur through multiple relaxation pathways, both radiative and non-radiative. The amount each of these different relaxation processes contributes to the T_1 can be specified by a *branching ratio*. This is particularly relevant for optical transitions in atomic defects where the system has the potential to decay to multiple auxiliary ground states (defined by different spin, or orbitals for instance, see Section 4). The T_1 process is probabilistic such that an ensemble of two-level systems does not decay simultaneously. T_1 decay means that the probability of finding a single defect or a population of defects in an energetically excited state goes down exponentially with time.

Spin decoherence times include T_2^* and T_2. Decoherence generally happens through interactions with electric and magnetic field noise in the lattice that randomly changes the phase of a qubit when in a coherent superposition. The relaxation process T_1 decreases the

phase and imposes a limit on the coherence time. T_2^* is shorter than T_2 because it includes contributions that can be reversed by a refocusing pulse. T_2 measurements generally perform refocusing of the ensemble coherence, this can adjust for effects such as inhomogeneous broadening, that reduces ensemble coherence. Random processes that don't have a well-defined phase evolution, such as spectral diffusion from randomly varying fields in the lattice cannot be refocused as well. T_2^* times are extracted from the decay envelope of Ramsey experiments, while T_2 times are extracted from the decay envelope of Hahn-echo experiments.

2.2 Measurement techniques

Multiple techniques can be used to interface spin defects. The main techniques used in this thesis are photoluminescence (PL), photoluminescence excitation (PLE), and optically detected magnetic resonance (ODMR), optical spectral hole burning (SHB) recovery.

In most of our experiments the collection was through a confocal setup. A Gaussian beam is focused on the surface of the sample, but the collection of light depends on the defect's emitted photons scattering into the solid angle defined by the objective. The amount of collected photons can be a relatively small percentage of all the photons emitted, when you consider that the defect can also emit isotropically, with at least half of the photons being emitted into the sample, in a solid angle 4π. This does not even consider effects such as Fresnel reflection off of the interface between the host crystal and silicon, which will also reduce the number of photons that can escape the crystal due to a discontinuous refractive index at the interface. Losses in the collection path also occur through the finite transmission of optics, and through the fiber-optic coupling efficiency, which for single-mode fiber also depends on Gaussian mode matching.

A setup for a photoluminescence experiment to characterize divacancy defects as in 7 is shown in Fig. 2.3 In a PL experiment, higher energy light is sent to the sample, and filtered from the collection path by a long pass filter. While the amount of filtering depends

on the laser power, collection efficiency of the setup, and detector efficiency, two or more long-pass filters are required to provide >100dB of filtering. The high energy light can excite the defect if it falls on the defect's phonon absorption band, or be transferred to the defect by free charge carriers if the energy is larger than the electronic bandgap. The energy and mechanism of excitation is important consider because the conduction band and absorption bands will couple to different transitions and sites for a defect with different efficiencies.

There are three types of optical detectors used in the experiments in this thesis: InGaAs pixel arrays, high-gain photodiodes, and single-photon detectors. The InGaAs pixel array detector was used for PL spectroscopy measurements, and combined with a spectrometer to spatially separate different wavelengths of emitted light, such that individual pixel readings correspond to the wavelength of interest. One shortcoming of this approach for spectral filtering is that the detected light corresponds to the first diffraction order of the grating in the spectrometer, and diffraction into higher order is lost, making it difficult to measure weak fluorescence. Furthermore, InGaAs detectors require cooling to -100 degrees Celsius to get the lowest dark count rates, but these rates, and the quantum efficiency of the detector are orders of magnitudes worse than single photon detectors. Therefore, they are best used to measure relatively bright defects. Photodiodes and single photon detectors can also be combined with a monochromator for frequency resolution of light. However, this requires nuanced tuning and calibration of the monochromator across the wavelength spectrum of interest. Another option of spectral filtering relies on the use of a tunable interferometer, many commercially available options exist, particularly in the telecom bands, that rely on electrically or mechanically tunable fabry perot interferometers.

High gain photodiodes can be used to measure ensembles of relatively bright defects (such as vanadium ions, and divacancies). Individual photodiodes do not have frequency resolution and are generally operated at room temperature. A high gain photodiode paired with a transimpedance amplifier can measure down to femtowatts. However these diodes

have a large noise floor, about ~ 2 percent of their dynamic range. Use of a lock-in techniques can deconvolve experimental signals from a noise background that would maket hem difficult to observe directly, as was done in 7.

For measurements requiring the highest detection sensitivity we used superconducting-nanowire single photon detectors (SNSPDs). SNSPDs are a lithographically defined device consisting of a superconducting nanowire biased near it's critical current. They are typically operated at temperatures $\sim 2 - 4$ K, below the superconductor's critical temperature, and at temperatures low enough to avoid detrimental effects such as the formation of vortices. Heating caused by incident photons causes a region of the nanowire to become resistive. This resistance results in a voltage pulse that can be detected with fast time-tagging logic. Modulation of the bias current can also be used as a form of temporal gating of the detector in experiments with laser pulsing, where a strong incident laser pulse on the detector could cause undesirable quenching. The best detectors have a dark count background of ~ 10 Hz and detection efficiencies ~ 90 percent, with an increasing number of commercial options meeting these specs. SNSPDs are typically designed for a specific operating wavelength range by deposition of an optical Bragg mirror over top to reject certain wavelengths. To obtain the best performance with SNSPDs it is also critical to systematically eliminate excess sources of light that can leak into the experiment and increase the dark count background.

Emission from the defect is spatially filtered using a spectrometer and detected on a >1D pixel array detector. Because the excitation source is not selective to the different optical transitions, the PL measurement is a measurement of the defect's emission structure, and cannot provide information about the population distribution in the optical ground state manifold.

The PLE technique is similar to PL, except in PLE a resonant laser is scanned across the defect's zero phonon line long pass filtering at lower energies only collects the phonon sideband for each transition (see Fig. 2.4). Thus the PLE experiment is sensitive to the

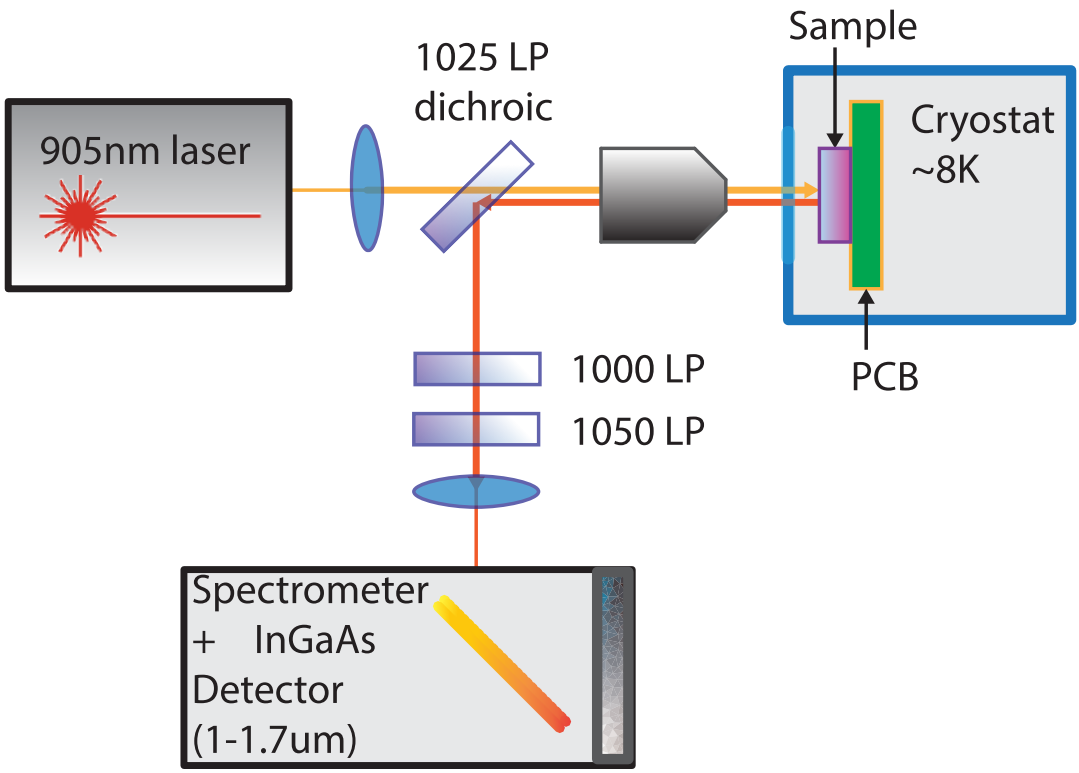

Figure 2.3: Schematic of PL spectroscopy setup used to measure divacancy photoluminescence spectra in Section 7.

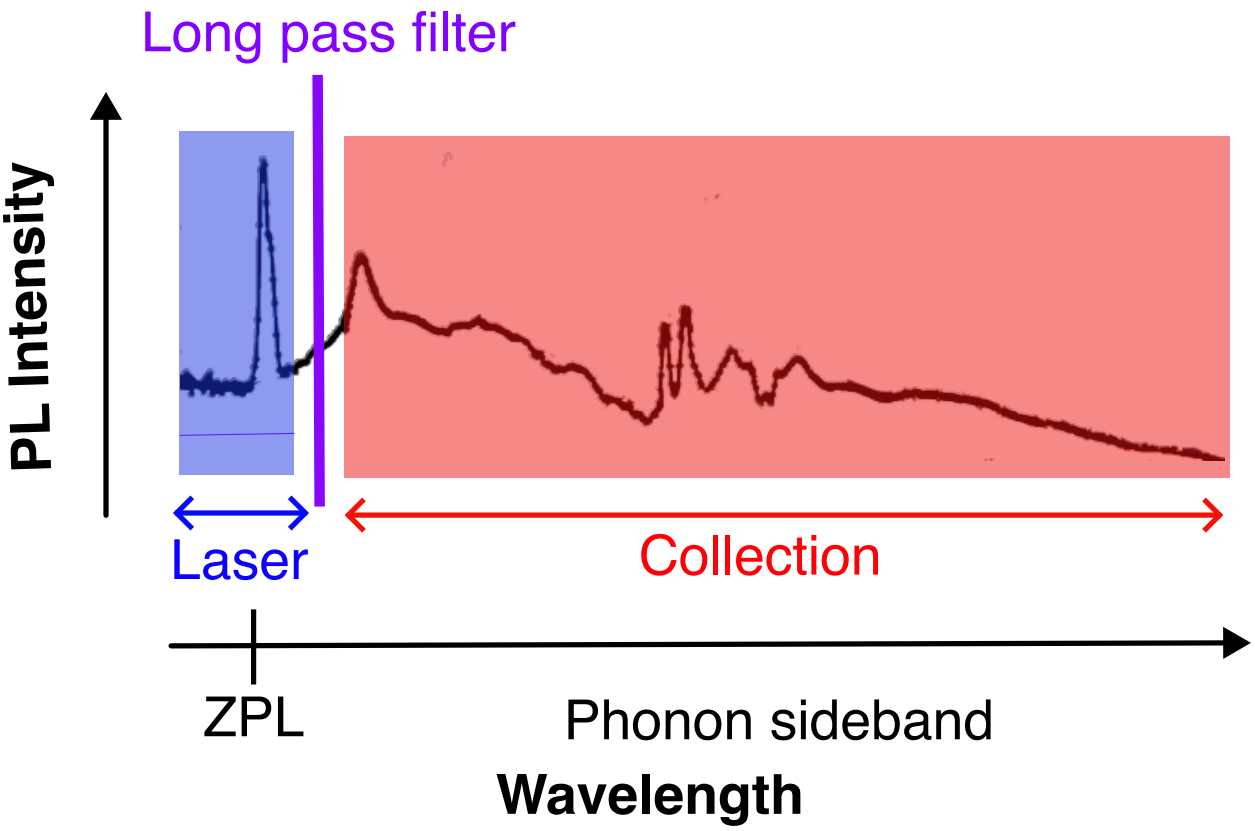

Figure 2.4: Illustration of PLE excitation and collection wavelengths.

ground state populations, but in contrast to PL does not give information about the different decay pathways, as there is no frequency domain filtering of the collected phonon sideband photons.

While a defect's spin state can be directly detected through electron or nuclear magnetic resonance (ESR and NMR), one advantage of optically active spin defects is the capability to readout the spin state with high efficiency photodetectors through ODMR. ODMR techniques can circumvent certain engineering challenges such as the need to engineer microwave resonators to enhance the spin polarization detection sensitivity. Emission from bright defects, such as the divacancy or vanadium defects in silicon carbide, can be read out at least on the ensemble level with high gain, and relatively inexpensive, photo detectors. For more noise sensitive applications, superconducting single-photon detectors can be used to detect emission from individual defects, with dark count backgrounds on the order of 10s of Hz.

ODMR measures the change in fluorescence driven by microwave resonance of the defects. Reshuffling of the spin populations is detectable as changes in optical fluorescence in the case where different spin ground states exhibit differences in fluorescence. Measuriing small ODMR signals may require lockin techniques, particularly in ensemble measurements. ODMR can be combined with pulsed microwave control sequences to perform coherent control and optical readout of the spin state.

Spectral hole burning recovery can be used to probe the spin lifetime. In spectral hole burning recovery an optical pulse pumps a spin population into a dark shelving state. This results in a decay in fluorescence during the hole burning pulse. After some delay time the initial ground state spin population is probed by a second pulse. The initial fluorescence of the second pulse will depend on the delay time from the first, with exponential recovery being driven by T_1 processes.

CHAPTER 3

ELECTRONIC STRUCTURE OF TRANSITION METAL DEFECTS IN SIC

3.1 Structure of the silicon carbide lattice

Much of the study of solid state spin qubits is focused on defects in silicon carbide. Silicon carbide is an ideal host due to its transparency, large electronic bandgap, and low abundance of nuclear isotopes. Silicon carbide is also promising because its use in power electronics has led to wide commercial availability and active complementary research in device development and materials science. Thus, researchers studying defects in silicon carbide have many different defects to study, ranging from intrinsic defects incorporated the growth process of silicon carbide substrates to those deterministically generated through methods such as ion implantation or irradiation.

Silicon carbide is a crystalline semiconductor that has found wide application in the power electronics industry. The chemical formula is SiC, but the precise arrangement of silicon and carbon bonds within a lattice give rise to multiple polytypes. In general, there are over 200 polytypes. However, the most common polytypes that may be obtained from comerical wafer vendors are 4H, 6H, and 3C. Here "H" indicates the *hexagonal* lattice structure, and "C" indicates the *cubic* lattice structure. The crystal may be considered to be formed of a series of 3 distinct bilayers, stacked along the crystal's *c-axis*. The bilayers are typically layered A, B and C. A and B bilayers are the same up to a translation. The C bilayer is rotated 60 degrees about the c-axis. The periodicity of stacking these bilayers within the crystal determines the numeric labeling of the polytype, i.e. 4H SiC consists of a repeating sequence of 4 bilayers, and the 6H layering is periodic every 6 bilayers. 4H silicon carbide has a repeated layering sequence of BABC shown in Fig. 3.2.

These differences between the lattice structure give rise to different properties. The

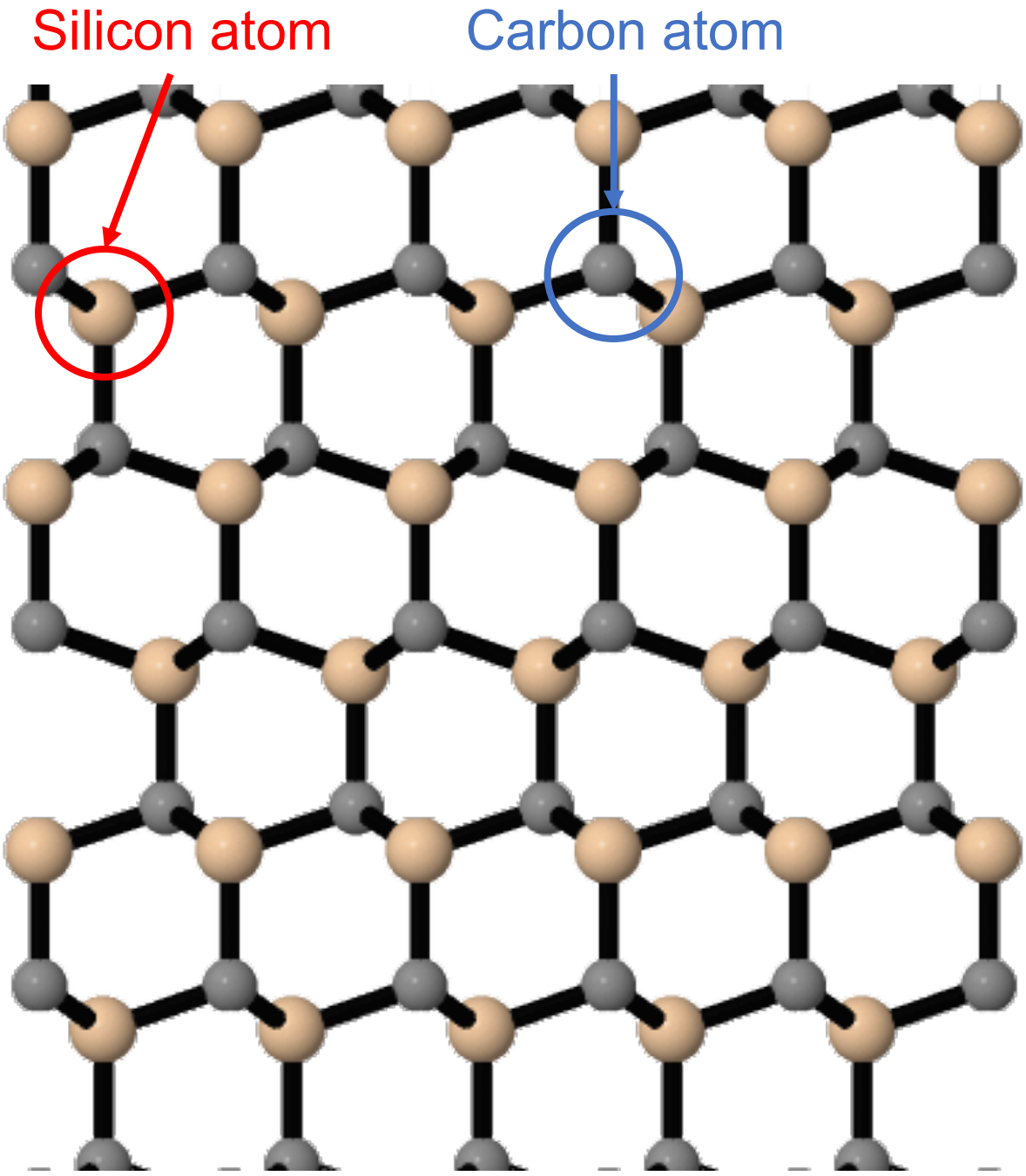

Figure 3.1: Crystal structure of 4H-SiC identifying silicon and carbon atoms.

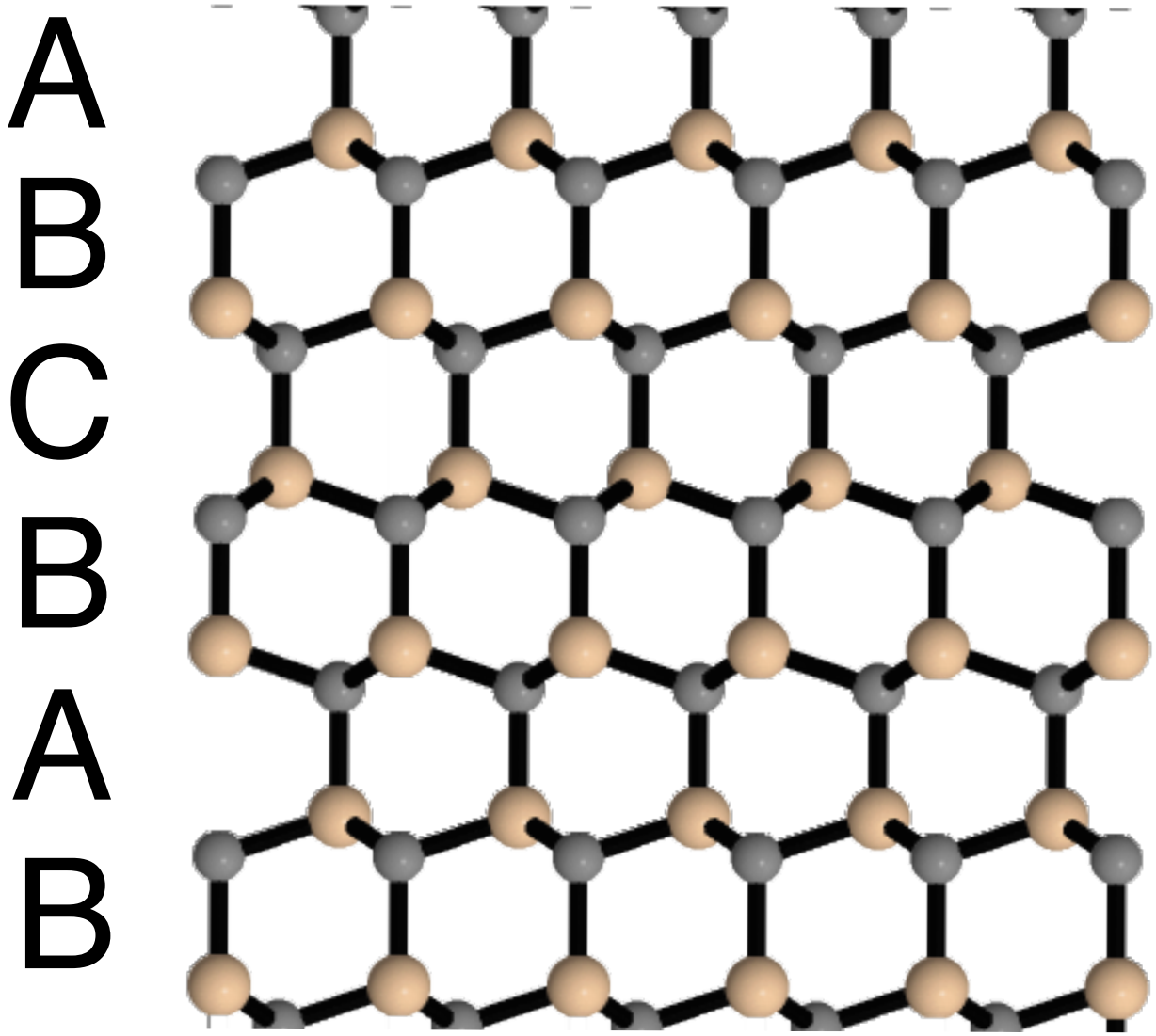

Figure 3.2: Crystal structure of 4H-SiC showing BABC periodic layering.

structure of the polytype will give rise to different symmetries and inequivalent forms of the defect, different dipole strengths, and interdistance bond lengths, modulating it's interaction with surrounding atoms. On the bulk scale, we see changes in the bandgap size, affecting the charge stability of the defect, it's transition to other charge states, as well as the defect's interaction with free carriers and other defects in the lattice. Additionally, due to the angle of bonds between silicon and carbon within the bilayers, we can find that the final layer of the crystal will contain either unterminated carbon atoms, or unterminated silicon atoms on opposite faces perpendicular to the c-axis. For commercially obtained silicon carbide, the wafer is typically labeled with one side as the *c-face* and one side as the *Si-face*. Due to silicon carbide's use in the power electronics industry, many commerically produced wafers will be manufactured with additional impurities to modify the crystal's resistivity and Fermi level. Common dopants include aluminum (p-type) and nitrogen (n-type). Additionally, some commercially obtained silicon carbide wafers are grown 4 degrees offset from the c-axis.

While there is great variability among silicon carbide polytypes and commercially produced substrates, silicon carbide materials share a few key properties. 4H, 6H, and 3C polytypes are generally opticall transparent down to 400nm. Therefore, at low optical powers, we can expect to resonantly address defects without significant absorption and heating within the lattice. However, conversely, if we wish to ionize a defect, we need to have an excitation source at shorter wavelengths, approaching the UV. Additionally silicon carbide is one of the hardest materials, with an average young's modulus of 400 GPa, (although values as high as 700GPa are also not uncommon). The relative hardness of silicon carbide compared to other materials has consequences for silicon carbide phononics, spalling, and defect-strain interactions.

3.2 Point symmetry and the crystal field interaction

In this section I will describe the role of lattice symmetry on the orbital energy structure of an atomic point defect in a lattice. I will also go in depth specifically for the case of transition metal ions, whose states are defined by their incompletely filled d-orbitals. This discussion will provide the foundation for understanding the interactions that define the energy structure of vanadium in silicon carbide and give rise to the physics described for that defect in the rest of this thesis. In crystal field theory, the electric field from surrounding atoms in the lattice act as perturbations to the free-ion energy structure defined by the atomic potential. Physically, this effect occurs due to the Coulomb interaction between the electron cloud of the defect and the electron cloud of surrounding atoms.

For lighter elements, the nuclear potential will be approximately spherical and the solutions are spherically symmetric superpositions of the spherical harmonic basis set. The spherical harmonics are themselves not spherically symmetric and the effect of surrounding electric charges will be to raise or lower the energy of specific orbitals while other orbitals are unaffected. While there are an infinite number of unoccupied orbitals for a given free atom, it will be relevant to consider the energetically equal states for the unperturbed atom. When looking at a spin defect this is typically the orbitals where the electron configuration is such that there is effectively a single unpaired electron spin (electron spin-1/2) or effective spin-1 system.

Furthermore, the orientation of specific orbitals in space is not well defined for a free ion in a symmetric potential. The prescence of the lattice will break this symmetry and the basis wavefunctions will be oriented to reduce the energy of these interactions. The effect of surrounding potentials therefore depends on specific locations of neighbor atoms within the lattice. The point symmetry of a defect substituting for a silicon atom in the silicon carbide lattice (as is the case for vanadium in silicon carbide) depends on the polytype. For a cubic polytype, the symmetry will be tetrahedral (T_d), while for a hexagonal polytype, the

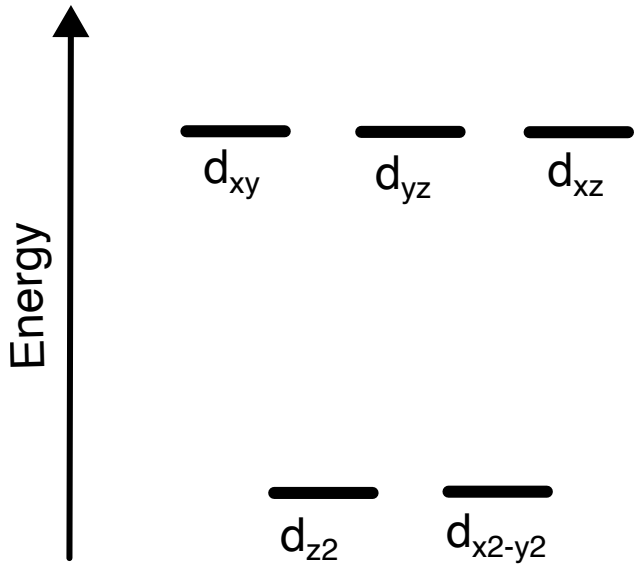

Figure 3.3: Change in energies of d-orbitals due to tetrahedral crystal field.

symmetry will be C_{3v} [77].

For transition metal defects in silicon carbide, such as vanadium, we are typically looking d-orbital states. The electron configuration of transition metals is such that the n=4 shell of the atom is partially occupied, but the defect assumes a 3+, 4+, or 5+ oxidation state when bonding with the lattice, leaving a partially occupied d-orbital.

For vanadium, the electron configuration is $[Ar]3d^3 4s^2$. Under the 4+ oxidation state we have a configuration $[Ar]3d^1$. Likewise, we have $[Ar]3d^2$ for 3+ and $[Ar]$ for 5+. For a defect with a d-orbital configuration, we have 5 spherical harmonics to consider, they are d_{xy}, d_{yz}, d_{xz}, d_{z^2}, and $d_{x^2-y^2}$. For a tetrahedral potential the d_{xy}, d_{yz}, d_{xz} orbitals will increase in energy due to their wavefunctions being closer to the surrounding atoms. This lifting of the degeneracy due to the crystal field interaction is illustrated in Figure 3.3. The orbital ground state doublet may be labeled by it's irreducible representation E while the excited state may be labeled by the three-dimensional irreducible representation T_1 [69].

For V_{4+} in silicon carbide, it is the addition of the C_{3v} potential that splits T_1 into another orbital doublet E and singlet state A_1

3.3 Spin-orbit coupling

The spin-orbit interaction plays an important role in the physics of transition metal defects in silicon carbide. The spin-orbit interaction is a well-known fine structure correction to the atomic energy structure characterized by the interaction of the electronic spin angular momentum degree of freedom (labeled S) and the orbital angular momentum degree of freedom (labeled L).

The spin-orbit interaction is a relativistic effect that originates from the a magnetic field induced by an electron with orbital angular moment in it's own rest frame[69]. This magnetic field couples to the electron's intrinsic spin angular momentum. Each angular momentum is described by a vector of angular momentum operators $\vec{L} = (L_x, L_y, L_z)$, and $\vec{S} = (S_x, S_y, S_z)$. The spin orbit interaction is characterized by the dot product of these two vectors $\lambda \vec{L} \cdot \vec{S}$, with the strength of the spin orbit interaction denoted by λ. This interaction is time-reversal symmetric [69].

The spin-orbit interaction has a couple effects. On one hand, it connects the orbital wavefunction to the spin degree of freedom. This manifests as a non-isotropic g-tensor where, in comparison to the case of the free electron, the magnitude of g can deviate from 2 and become dependent on the orientation of the magnetic field. The orbital angular momentum degree of freedom connects the crystal field interactions and spin orbit coupling, such that the symmetry of the lattice is influences the anisotropy of the g-tensor. This is evident in the different g-tensors observed for an atom in sites of different point symmetries.

The spin-orbit interaction may be understood as a perturbation acting on the orbital states of the defect's orbital eigenstates. Atoms with larger atomic number will have a larger spin-orbit coupling [69]. To leading order, the spin-orbit coupling lifts the degeneracy of V^{4+}'s ^2E doublets in the ground and excited state[71, 69]. The orbital doublets split into orbital states with irreducible representation Γ_4 and $\Gamma_{5,6} = \Gamma_5 \oplus \Gamma_6$. Furthermore, the spin-orbit interaction affects the selection rules of V^{4+} under an applied external magnetic field

[69], by allowing transitions that are otherwise forbidden by C_{3v} symmetry. As discussed in 4 the orbital transitions are spin conserving to the leading order, but the spin-orbit coupling and the hyperfine interaction cause mixing that makes spin-non conserving transitions weakly allowed[69, 68].

CHAPTER 4

SIC:V^{4+} SPIN T_1 AT MILIKELVIN TEMPERATURES

4.1 Introduction

A spin photon interface allows spins to be optically initialized and read-out using light, and can also be used to generate spin-photon entanglement. A spin photon interface would combbine a long lived spin memory with a spin-dependent optical transition for generating spin-photon entanglement [76, 32, 42]. A spin-photon interface that operates in the one of the telecom bands would be desirable for a couple of reasons. One reasonbecause of the availability of relatively inexpensive optical components operating in the telecom band. Another reason is because it enables the use of the low-loss band of fiber-optic cable - a pre-esiting platform on which to pursue long-distance entanglement. However, it is rare to find defects with both favorable spin properties and telecom band operation. Therefore many parallel efforts are exploring frequency conversion for defects that emit at shorter wavelengths, or the use of devices to tailor the properties of existing telecom defects [19, 21, 11].

The vanadium defect (V^{4+}) possesses several properties that make it particularly interesting for quantum technologies in silicon carbide (SiC). These include short optical lifetimes, emission in the telecom O-band, spin-dependent optical transitions, and encouraging spin properties at cryo- genic temperatures [64, 15, 5]. V^{4+} in silicon carbide is also advantageous for quantum technology due to the fact that it can be readily obtained as ensembles in commerically available wafers [47, 4, 74].

Here, I will describe our demonstration of optical spin polarization and readout of the vanadium defect in silicon carbide. I will also describe our efforts to characterize vanadium's ionization and repump rates under varying optical powers. Using ideal operating parameters obtained from our study of ionization rates, we are able to show high fidelity ensemble

spin initialization and readout, enabling the measurement of spin T_1 times and sub-Kelvin temperatures. High fidelity spin initialization and readout, and long sspin relaxation times were observed for both α and β sites in both 4H and 6H siilicon carbide.

While the spin relaxation time T_1 is not a direct measure of coherence, it is still important to characterize as it sets a fundamental limit on the spin T_2. We used all-optical spectral hole-burning recovery to measure the T_1. Performing this experiment at temperatures below 2K allowed us to measure T_1 times exceeding 20s. Therefore, we identified a temperature and set of operating parameters where the T_1 time will not limit coherent control of the vanadium defect's spin. We also studied the phonon relaxation mechanisms through measuring the temperature dependence of T_1. Between 1-2 K, we observe the Orbach process dominating the spin relaxation rate. We also identified the resonant level participating in the Orbach process as the next highest ground state orbital level $GS2$, and proposed to increase the $GS1 - GS2$ orbital splitting by the use of strain. This would tune the V^{4+} states out of resonance with phonons driving relaxation and ideally increase the T_1 time of the defect at elevvated temperatures. These experiments lay the groundwork for future studies of V^{4+} in SiC toward developing a spin-photon interface.

4.2 Optical spectroscopy and charge properties

Vanadium substitutes for a silicon (Si) atom in the SiC lattice. There are two possible inequivalent sites that vanadium can occupy within 4H silicon carbide (one hexagonal (h) and one quasi-cubic (k) site). In 6H silicon carbide, vanadium can sit in one of three inequivalent sites for the 6H polytype (one hexagonal (h) and two quasi-cubic (k_1, k_2) sites) (Fig. 4.2 (a)).

Figure 4.1 shows the electronic structure of the V^{4+} α site in 4H silicon carbide, when the Zeeman energy exceeds the hyperfine interaction. The spectrum is similar for the β site. In the β site the excited state singlet and doublet states are flipped in order energetically. For

the α site, the singlet lies in the conduction band, while for the β site both of the doublets lie in the conduction band.

The quadruply ionized vanadium ion (V^{4+}) possesses one active electron (spin 1/2) in its $3d^1$ orbital, forming a free ion ^2D state. The crystal field interaction with the surrounding silicon carbide lattice splits the ^2D state into an orbital doublet ground state and a triplet excited state. Further C_{3v} deformation of the point symmetry for the 4H and 6H polytypes (absent in 3C silicon carbide) breaks the exicted state triplet into an orbital singlet and doublet [44, 39, 6]. The spin-orbit interaction splits the energy of the orbital doublet states[69, 70]. The site symmetry and polytype will change the ordering of the orbital states and the magnitude of the splitting between them [64, 18]. We label the vanadium sites in 4H and 6H silicon carbide by α4, β, and γ, and label the orbital levels by GS1, GS2 and ES1-ES3 as in [77, 18] (see Fig. 4.2 (b)).

First, we experimentally investigate the orbital structure of the various sites of V^{4+} with resonant photoluminescence excitation (PLE) spectroscopy in the dilution refrigerator at 2.7 K. As in previous experiments [77], we use a tunable laser for resonant excitation and collect photoluminescence (PL) from the phonon sideband while filtering out the resonant laser. The PLE spectra displays clearly resolved optical transitions (Fig. 4.2 (c), (d)), allowing us to confirm the SO splitting of each site (see Table 4.3), related to the phonon-relaxation mechanism as we discuss in the following sections ('Phonon mediated spin relaxation' section). Furthermore, the site assignment and the irreducible representation of each orbital level can be determined from the orbital structure and the selection rules except for the 6H-γ site where the small SO splitting comparable to its inhomogeneous linewidth makes it a challenge to optically resolve the distinct orbital levels (Fig. 4.2 (d)).

The samples used in the experiment are 500um thick semi-insulating vanadium doped wafers from II-VI. Secondary-ion mass spectroscopy (SIMS) measurements were performed to identify the concentration of vanadium and other common impurities in the silicon car-

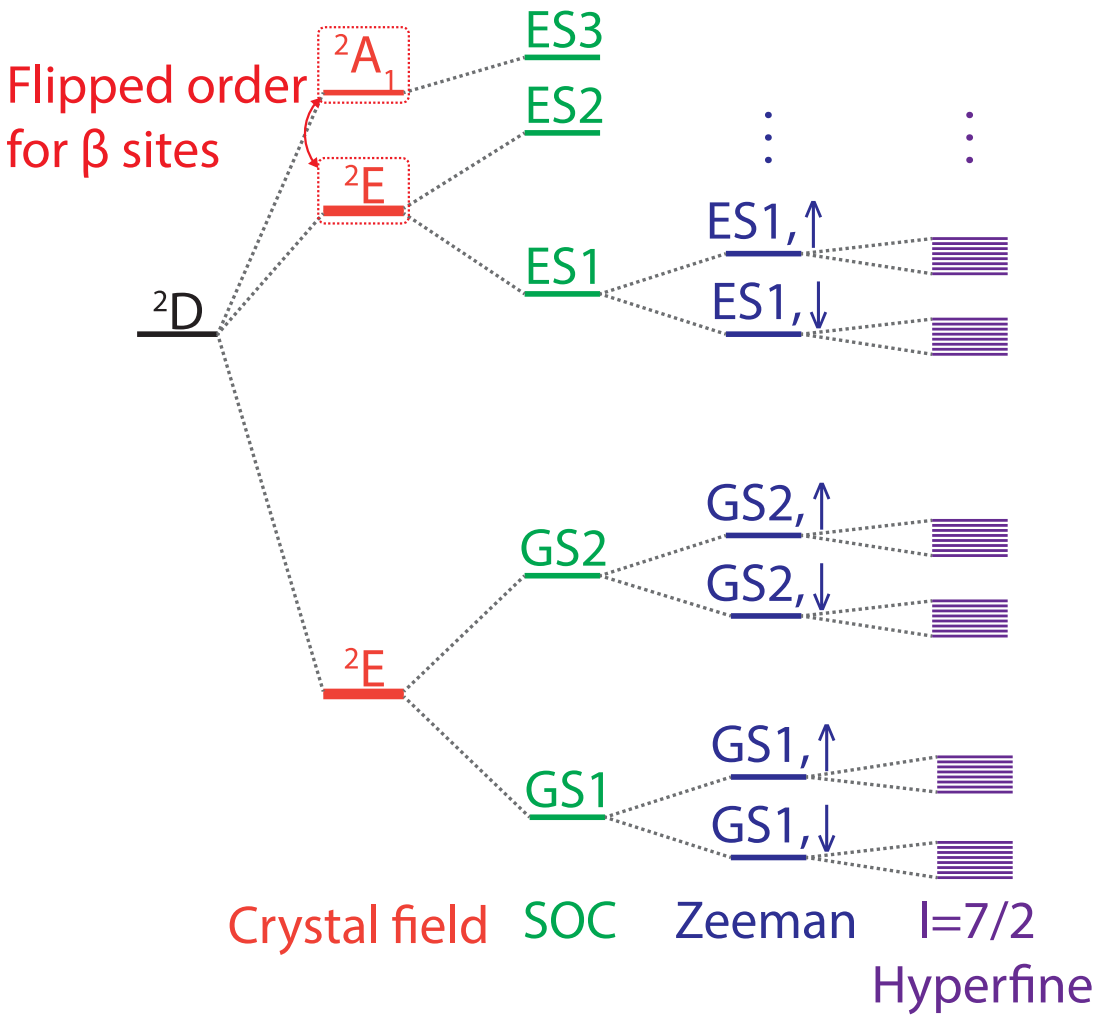

Figure 4.1: Schematic illustrating the interactions which form the electronic structure of V^{4+} α site in 4H silicon carbide, when the Zeeman energy exceeds the hyperfine interaction.

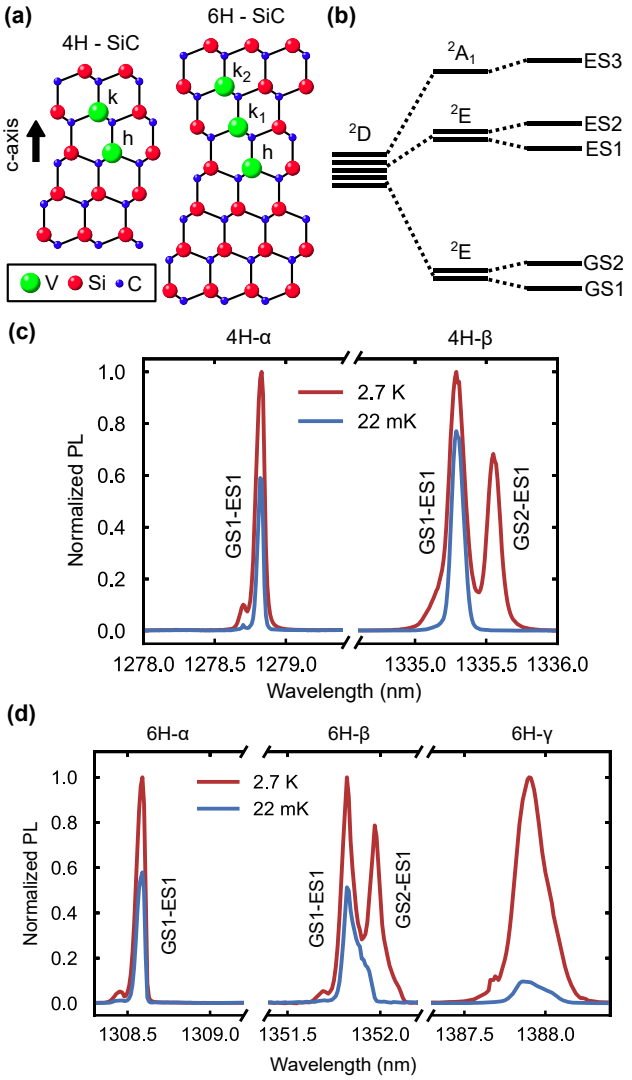

Figure 4.2: Optical spectroscopy of V^{4+} in 4H- and 6H-SiC. (a) Vanadium defects substitute inequivalent Si sites in the 4H- and 6H-SiC lattice. (b) Orbital level structure of V^{4+} in SiC. The crystal field from the SiC lattice splits the orbital d^1 states to an orbital doublet ground state and an excited state consisting of an orbital singlet and doublet state. The order of the orbital singlet and doublet depends on the site. Additionally, the spin orbit interactions lead to SO splitting in the orbital doublets. (c, d) Resonant PLE spectroscopy measurements at 2.7 K (red) and 22 mK (blue) for 4H- and 6H-SiC. The optical transitions in the 6H-γ site are within the inhomogeneous linewidth, and thus selective excitation on the GS1-ES1 transition is challenging.

bide lattice. For the 4H sample, the concentrations were [V]=1.3e17/cm^3, [N]=7e16/cm^3, [B]=3.1e15/cm^3, and [Al]=2.2e14/cm^3. For 6H sample the concentrations were [V]=1.4e17/cm^3, [N]=3.7e16/cm^3, [B]=6.2e15/cm^3, [Al]=1.6e14/cm^3. The samples were measured as-received without any additional processing.

Figure 4.3: Schematic showing the dimensions and vanadium concentrations of 4H and 6H silicon carbide samples used in this experiment.

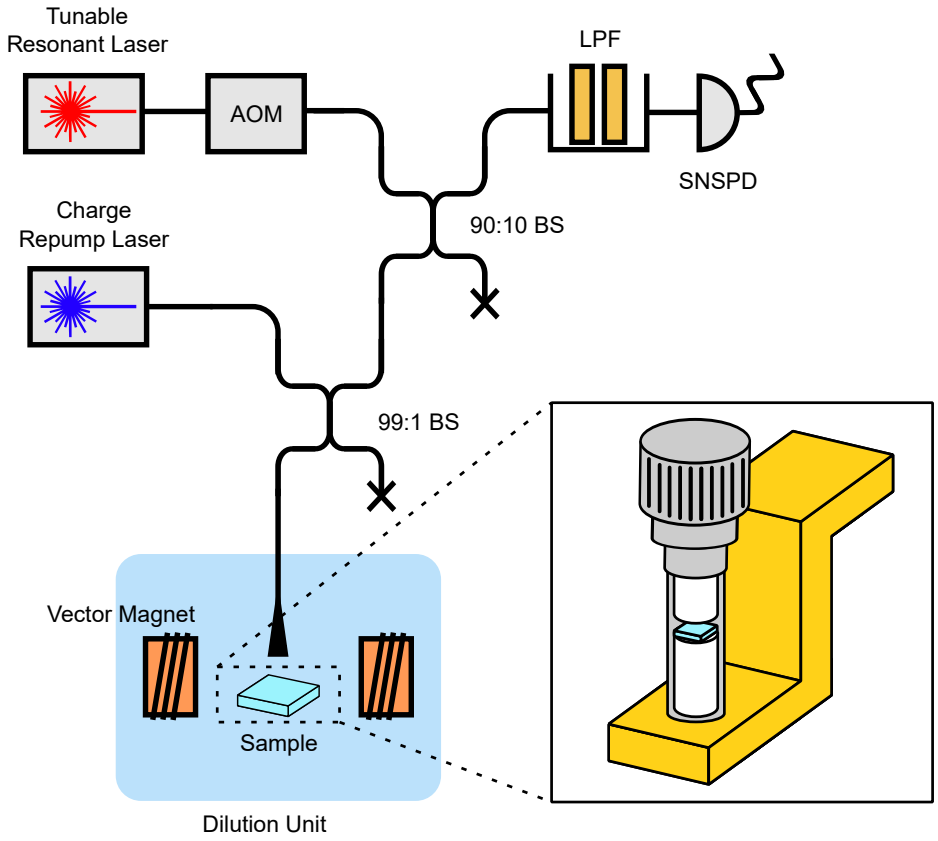

Figure 4.4: Schematic of experimental setup. Figure is reproduced from [3].

Figure 4.4 shows the experimental setup used to perform optical spectroscopy at dilution temperatures. The experiments were performed in a BluFors LD250 dilution refrigerator equipped with a 0.25/0.25/0.25 T superconducting vector magnet (American Magnetics Inc.). The excitation laser was a Santec TSL-570 and the acousto-optic modulator used was

the AA Optoelectronics MT110-MIR20-Fio-PM0,5-J1-A-VSF. The 405nm charge repump laser was a QPhotonics QFLD-405-20S. The 405nm laser and O-band laser were combined with a fiber 99:1 beamsplitter. The setup is configured such that 1 percent of the light from the 405nm laser is combined with 99 percent of hte light from the O-band laser. A second 90:10 fiber beamsplitter in the path was connected to the O-band laser (befor the 99:1 beamsplitter) to be used as a circulator to partially separate the collected PL from the excitation laser. These paths are connected through a feedthrough to single mode fiber in our fridge that is terminated on the mixing chamber. The laser power at the sample is 75nW for the reonant laser and 400nW for the charge stabilization laser. The collected light travels through both the 99:1 and 90:10 beamsplitter. After the beamsplitters the fiber is connected to a Thorlabs FBC-1310-APC U-bench which contains longpass filters (Thorlabs, FELH1350 for 4H-SiC and Thorlabs, FELH1400 for 6H-SiC) that filter out the laser excitation signal and collect fluorescence in the phonon sideband. The light that exits the U-bench is detected with a superconducting-nanowire single photon detector. Counts from the SNSPD are gated and detected with a Swabian Instruments, TimeTagger Ultra. The pulse sequences in our experiments were generated by an arbitrary waveform generator.

We simplify optical alignment in the dilution refrigerator by dicing the silicon carbide wafers to 1.69 mm x 1.69 mm squares. This enables the samples to fit within the area of a standard single mode fiber ferrule and align to a fiber using fiber ferrule sleeves. The sample is attached to a cylindrical sapphire puck with Apezion-N grease. The fiber is held above the sample and aligned to the c-axis using a ferrule coupling sleeve around the sapphire puck and fiber ferrule. The distance between the fiber ferrule and sample is $\sim 100\mu$m. In this configuration the optical polarization is perpendicular to the c-axis.

Photoluminescence excitation spectroscopy is performed by sweeping a tunable laser over the vanadium zero-phonon lines. We collect only emission in the phonon sideband using optical long pass filters. Weak 405nm laser excitation is also sent to the sample to compensate

for ionization effects in the 4H sample. Measurements of the 6H sample do not use the charge rempump laser. The experiments in this section were performed at 22 mK with no external magnetic field. A laser diode controller is used to slowly pulse the 405nm laser by gating the laser's current.

All measurements were performed in a dilution refrigerator. The samples are resonantly excited using a narrow-linewidth tunable O-band external cavity diode laser. The propagation of the laser beam in our setup in the dilution refrigerator is parallel to the silicon carbide c-axis, and the polarization of the light is in the plane perpendicular to the c-axis. Pulses are generated for transient spectral hole burning using a single fiber-coupled acousto-optic modulator. The 405nm laser power is approximately $\sim$400 nW at sample.

Lowering the temperature to 22 mK causes thermal polarization to the GS1 orbital ground state. For the 4H and 6H alpha sites this is a weaker effect, owing to the large GS1-GS2 splitting $>$ 500GHz, which enables polarization at elevated temperatures. We also found that the overall intensity of the PLE is decreased at the lower temperature (see Fig. 4.2). Two possibile effects could cause this decrease in PLE. The first is that the Debye-Waller factor could increase at these lower temperatures, but since we measure the phonon sideband our experiments will measure the corresponding decrease in phonon sideband emission. Another possibility is that the decrease in intensity is due to an increase in the electron spin lifetime, which causes some spectral hole burning as the laser is swept across the transition [29, 12, 10]. A zero-field splitting of the electron spin state exists due to the hyperfine interaction, and this may enable optical spin pumping of V^{4+} at zero magnetic field. Such a mechanism, in conjunction with the longer spin T_1 times at lower temperature could be responsible for the observed decrease in intensity of the PLE peaks at 22 mK. The 6H gamma site is excluded from the rest of this discussion as inhomogeneous broadening and a small spin-orbit coupling make it difficult to resolve the individual orbital transitions. Measurements in the rest of this section of the 4H and 6H beta site rely on the selective excitation of the GS1-ES1 transition.

The site assignments the irreducible representation of each orbital level, based off of the PLE measurements, are shown in (Fig. 4.5 (e)).

To determine the site assignments we consider the possible excited state orbital structures and magnitudes of the spin-orbit splitting. The k and k_2 sites have stronger C_{3v} symmetry, which causes the singlet $^2A_1$ level to sit abbove the ^2E levels (Fig. 4.5 (e)). The stronger C_{3v} symmetry also gives rise to a larger spin orbit coupling than the in the h and k_1 sites [64, 18].

In Fig.4.5 (a)-(d), we observed four optical transitions are observed for the 4H- and 6H-α sites, two transitions for the 4H-β site, and six transitions for the 6H-β site. The observation of four transitions for the 4H-α site suggests that the excited state consists of an orbital double. Similarities in splitting between GS1-ES1 and GS2-ES1 transitions between the 6H-β and 4H-4β sites, suggests that both transitions couple to an orbital singlet in the excited state. There are also similarities in the magnitude of the spin orbit coupling between the 4H and 6H α sites and the 4H and 6H β sites. Thus we label the site assignment of the 4H and 6H α sites as k and k_2 respectively. Since the Γ site has the smallest spin orbit splittings it has been assigned to the h site [77].

Past literature and the selection rules allow us to identify the irreducible representation labeling the orbital states for each site. For the selection rules, we consider whether a particular transition is allowed or forbidden to leading order. GS1 and GS2 correspond to the Γ_4 and $\Gamma_{5/6}$ irreducible representations for all sites [68, 26]. Selection rules between the and excited states can be used to determine the excited state assignment to the different irreducible representations. The selection rules we consider are specific to our excitation scheme, where excitation is polarized perpendicular to the c-axis. Optical transitions between the same irreducible representations ($|1,\Gamma_4\rangle$–$|2,\Gamma_4\rangle$ and $|1,\Gamma_{5/6}\rangle$–$|2,\Gamma_{5/6}\rangle$) are forbidden in the leading order citetissot2022nuclear. However, transitions between the excited singlet site couples to both irreducible representations in the ground state to leading order.

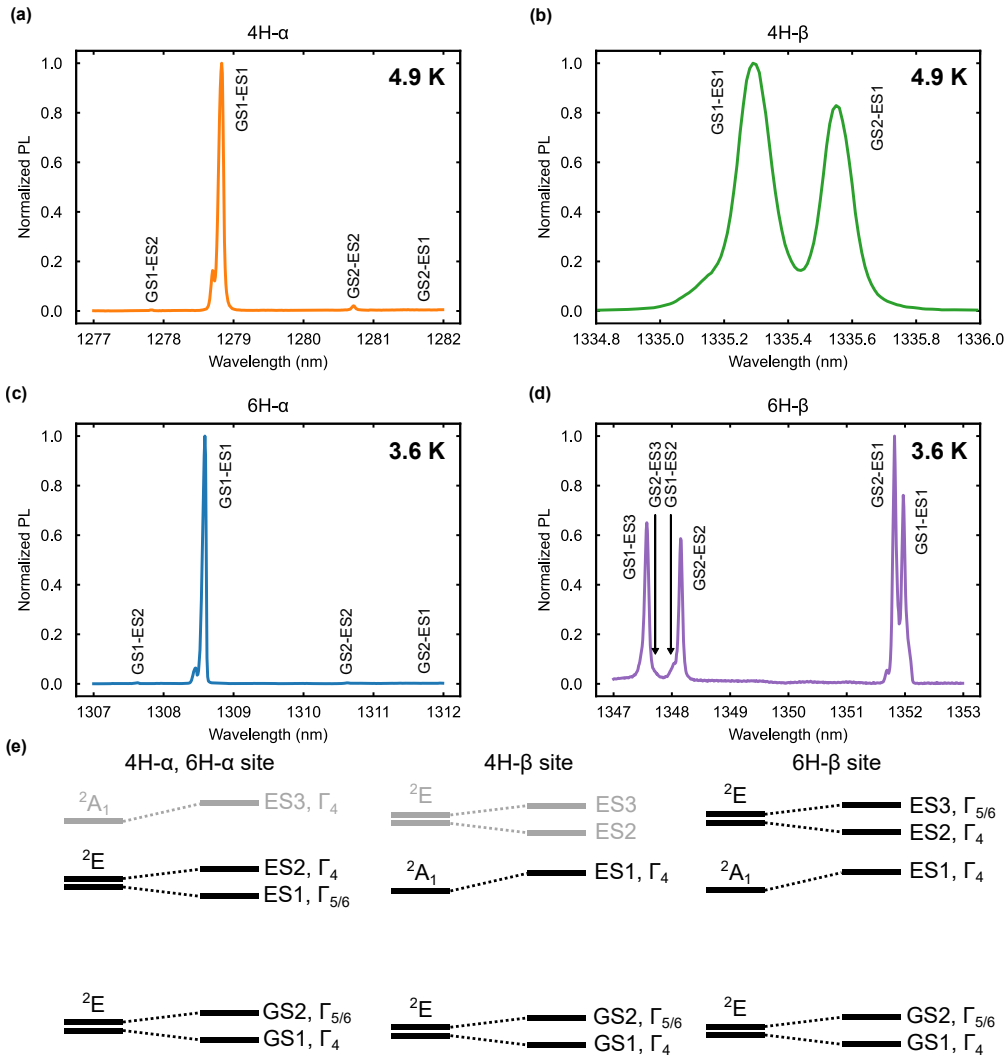

Figure 4.5: Photoluminescence excitation spectroscopy measurements of V^{4+} in 4H- and 6H-SiC. (a, b) Resonant PLE spectroscopy measurements for 4H-α and 4H-β site at 4.9 K. (c, d) Resonant PLE spectroscopy measurements for 6H-α and 6H-β site at 3.6 K. (e) Orbital level structure and corresponding irreducible representations of V^{4+} in SiC for different sites of 4H- and 6H-SiC. The energy levels in gray are positioned within the conduction band and are optically inaccessible. The results show similarity between the 4H-α and 6H-α sites, and 4H-β and 6H-β sites.

It is key to note that in Fig. 4.5 (c) and in [77] that the GS2-ES2 transition is strong at elevated temperatures. From this we can conclude that the GS2-ES2 transition is allowed, while GS2-ES1 is forbidden. Therefore ES1 may be labeled as $|2, \Gamma_{5/6}\rangle$, and ES2 may be labeled as $|2, \Gamma_4\rangle$. No ES3 transitions are observed for the α site, so it is assumed that this orbital singlet state is situated in the conduction band. Likewise, we can use the fact that GS2-ES1 is allowed at elevated temperatures, to assign the 4H-β ES1 to the Γ_4 irreducible representation for the excited singlet state. The orbital doublet for the 4H-β site 4.5 is also expected to lie in the conduction band (Fig. **??**c). The 6H-β site displays all six optical transitions.

Next I will describe the measured charge properties of V^{4+} in silicon carbide. For the current experiments on V^{4+} we wish to minimize unwanted transitions to other charge states. As an amphoteric defect used for charge compensation, vanadium has two additional charge states V^{3+} and V^{5+} (Fig. 4.6 (a), (b) reproduced from [51]). Additionally the V^{3+} is a spin-1 system that emits near 2 μm [73], making it potentially interesting for future studies. Previous work studying the V^{4+} defect observed a decrease in photoluminescence over time during resonant excitation [77, 16, 5, 75]. The decrease in photoluminescence is due to conversion to one or both of the V^{3+} and V^{4+} charge states. These same experiments also showed that the photoluminescence intensity could be recovered under weak continuous illumination with 405nm light. To try to understand the mechanism of ionization, we do a power dependent measurement of the resonant ionization rate for the α and β sites in both 4H and 6H silicon carbide.

While this experiment cannot conclusively identify the ionization process in Fig. 4.6 (a), (b), there are two possible mechanisms that may contribute. One mechanism is a two-photon ionization process promoting electrons from the V^{4+}/V^{5+} donor state to the conduction band. Another possibility is that a donor trap state may exist near the conduction band, and electrons are promoted from this trap state to the conduction band while we excite the

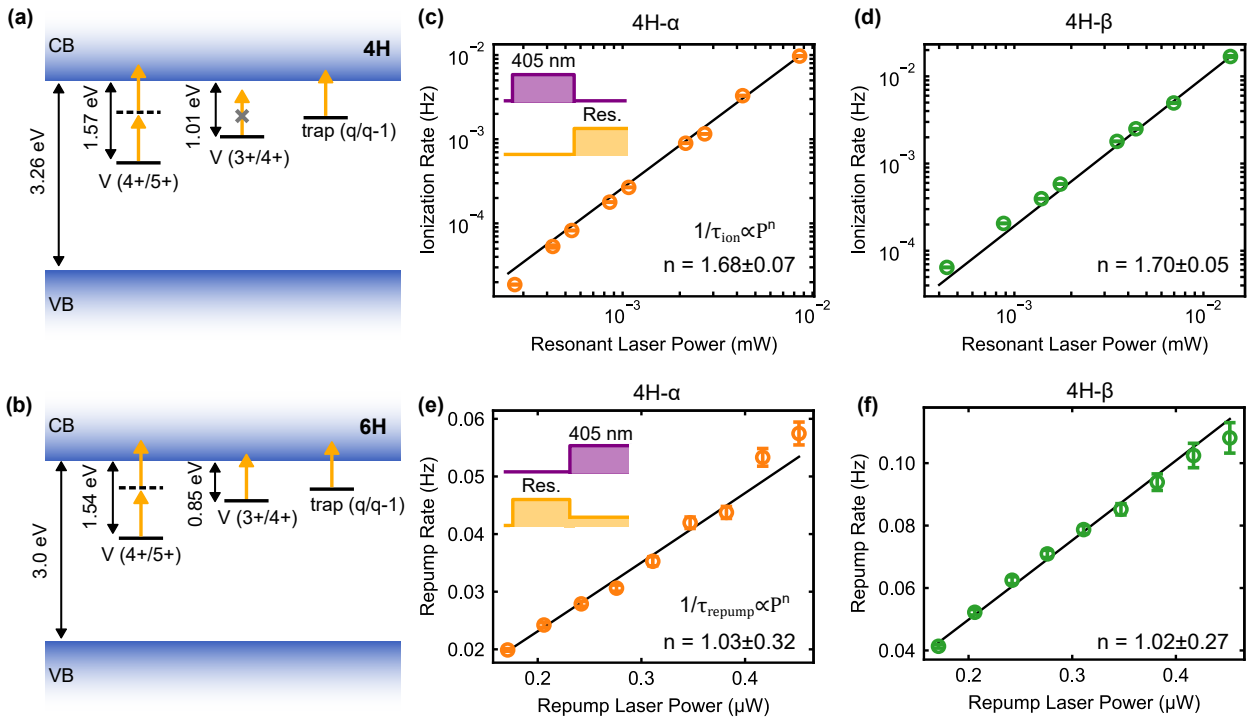

Figure 4.6: Figure reproduced from [3]. Ionization and repump rate experiments for V^{4+} in SiC.

vanadium defect. Then these electrons are subsequently recaptured by V^{4+} converting it to V^{3+}. It is possible that nitrogen, boron, or aluminum impurities can form these shallow donor states.

The effect of 405nm illumination was also characterized. First a long resonant pulse is used to ionize the ensemble. Then, 405nm excitation is applied to the sample. The PL recovery trace is read out afterward. The extracted recovery rates follow a linear dependence on the 405nm laser excitation power (see Fig.4.6 (e), (f)). This is consistent with the direct photionization of the dark charge state, since the 405nm laser has sufficent energy to promote an electron to the conduction band. To confirm that no ionization occurs in the dark we also perform an experiment where a 405nm laser pulse initializes the V^{4+} charge state and a resonant laser pulse reads the population in the V^{4+} charge state after a variable delay time.

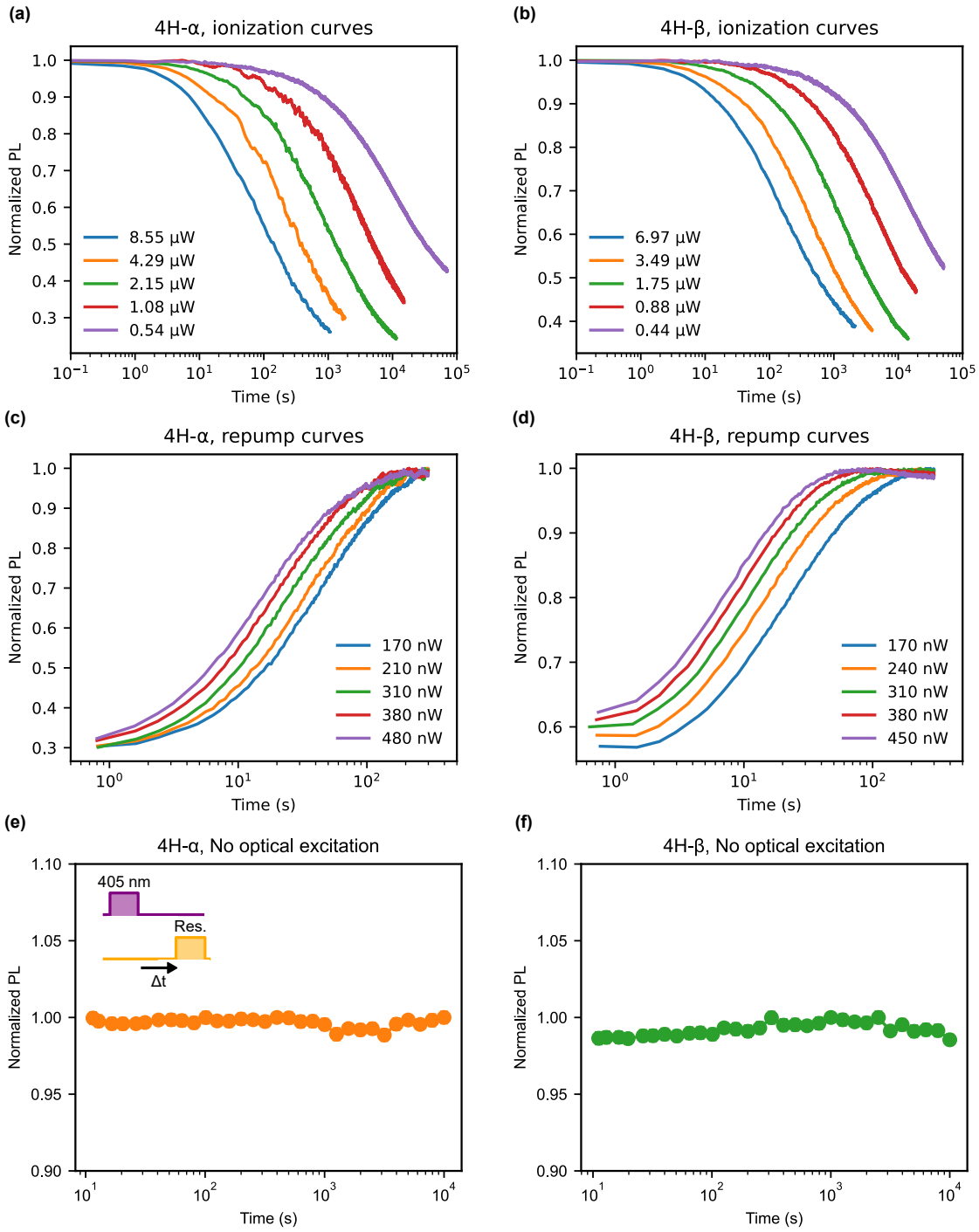

Figure 4.7: Charge dynamics during exposure to resonant laser, 405 nm laser, and no optical illumination. (a, b) PL decay curves from resonant laser-induced photoionization. (c, d) PL recovery curves from charge repump using 405 nm laser exposure. (e, f) V^{4+} charge state lifetime after 405 nm excitation (no laser illumination). No significant decay is observed after 10^4s, thus enabling spin T_1 studies with the hole burning recovery measurements. Inset shows pulse sequence for corresponding measurement.

4.3 Optical spin polarization, readout, and spin-relaxation times

The capability for optical spin polarization and readout are key requirements for a spin-photon interface. The short optical lifetimes of vanadium are advantageous because they enable detection of single defects [19, 53, 33], and efficient optical spin polarization. A short optical lifetime allows the spin to cycle through the excited state (under optical illumination) many times without spin relaxation. Cycling through the excite state allows the spin to flip following through a weakly allowed spin non-conserving transition, such that longer illumination times allow for transfer of the population to the inverted spin ground state. Optical readout is possible due to a decreased resonant fluorescence due to ground state spin population being shelved (see Fig. 4.8 (a)). For the vanadium defect, long spin relaxation times at milikelvin temperatures combine with sub-microsecond optical lifetimes to enable efficient optical spin polarization and readout.

The optical spin polarization experiments are performed at 23 mK under an applied magnetic field of 250 mT aligned to the c-axis. The magnetic field causes a Zeeman splitting of the electron spin states of magnitude $g\mu_B B$, where g is the Kramers doublet g-factor, μ_B is the Bohr magneton, and B is the static magnetic field. The Zeeman splitting at 250 mT is sufficiently large in this experiment to enable us to selectively drive a spin sublevel within the broadened ensemble[77], and the population will be shelved into the dark spin sublevel. We apply sufficiently low excitation power to avoid photoionization during the pulse, and observe the expected fluorescence decay resulting from optical shelving (see Ref. 4.8 (b)-(e)).

Due to being an all-optical method, the spectral hole burning recovery experiment is not selective to different shelving processes. Figure 4.9 shows the ideal orbital shelving scheme in our experiment under resonant illumination. In the ideal case, the population shelves to the inverted spin state within the same orbital, while the hyperfine spin remains mixed and unresolved. Optical shelving to or through other orbital states plays a minimal role. However, figure 4.10 shows other possibilities for a shelving state that may occur in the

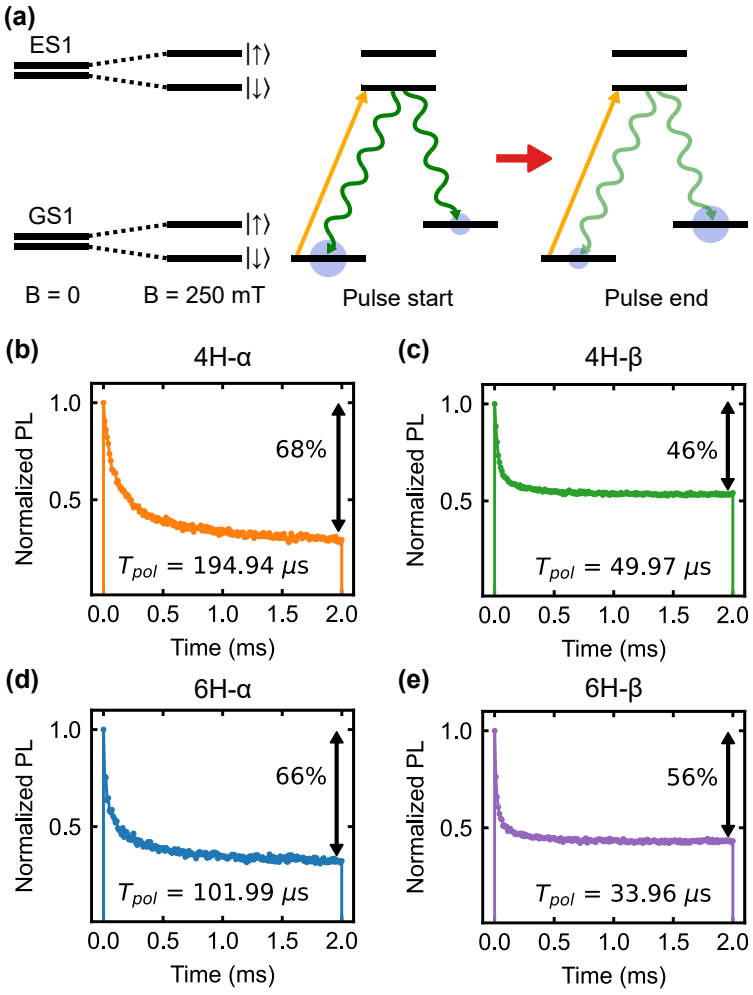

Figure 4.8: Figure reproduced from [3] Optical spin polarization of 4H and 6H α and β sites.

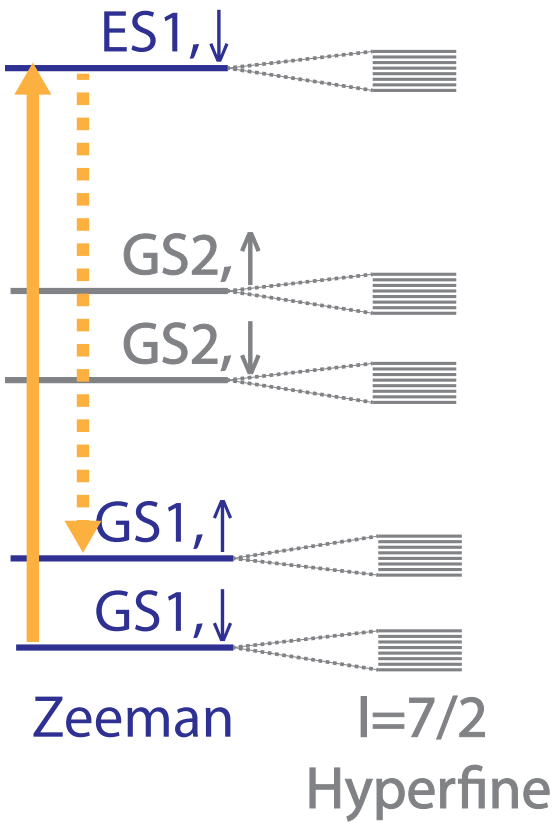

Figure 4.9: Schematic illustrating the ideal spin shelving under resonant illumination.

all-optical spectral hole burning experiment. The population could be shelved to a higher lying orbital or preferentially to another hyperfine level. Whether or not the spectral hole burning recovery method could be used effectively to measure the spin T_1 time depends on the relative magnitudes of transition and relaxation rates to and from each of the possible shelving states. In our experiments, the T_1 times have a dependence on magnetic field, indicating that the shelving state is a Zeeman sublevel.

Another complication comes from the effect of ensemble strain broadening on our optical initialization scheme, as depicted in 4.11. Strain shifts the transition energy of defects within the ensemble. This causes the different spin states within GS1 for different defects to overlap energetically. During the experiment the defects we excite will be preferentially in $GS1,\downarrow$ due to thermal polarization. Residual fluorescence from the opposite spin state will lower

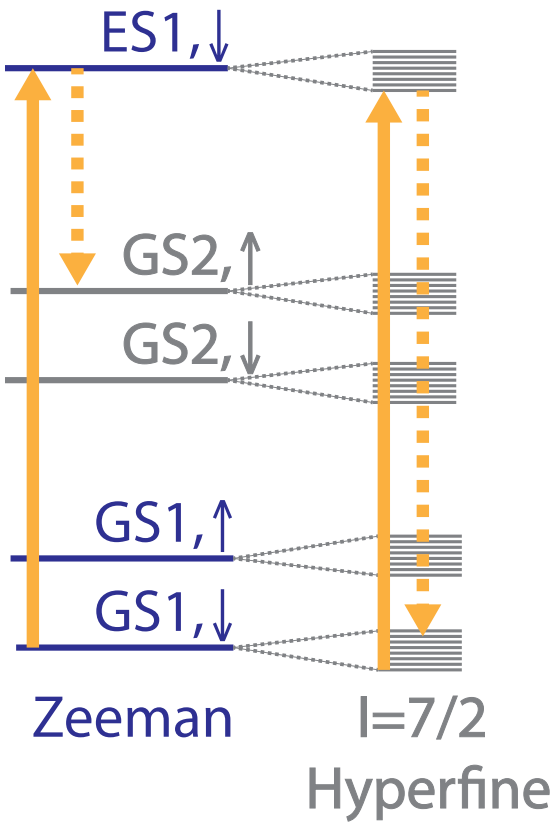

Figure 4.10: Other possible optical pumping schemes.

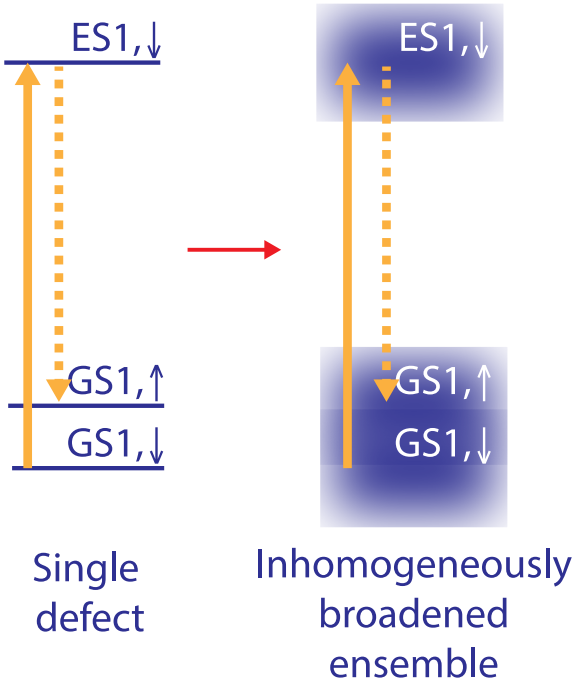

Figure 4.11: The effect of ensemble strain broadening on our optical initialization scheme.

the measured ensemble initialization contrast.

Based on the ionization experiments, a resonant laser power of $\sim$ 75 nW is selected to minimize charge effects during optical spin polarization. At the beginning of each experiment, a 405nm laser pulse is applied for >100 seconds at an optical power of $\sim$400 nW. 6H silicon carbide doesn't show any appreciable ionization under resonant excitation so the charge laser is omitted. The charge effects are also minimal due to the fact that the duration of our initialization measurements ($\sim$ ms) is much shorter than the ionization timescales.

The time-dependent fluorescence trace is fit to a single exponential, with exponential decay constant T_{pol}. T_{pol} was found to range from 35-195 μs, depending on the site. T_{pol} should depend on the spin relaxation rate, laser power, and transition strength of non-conserving transitions. However, we can simplify the analysis considering the fact that the spin T_1 greatly exceed T_{pol}, and the laser power was near the defect's saturation power. In order to identify the origin of the spin non-conserving transitions that allow for the optical

spin polarization, we consider the relative strengths of the allowed optical dipole transitions. We can compare T_{pol} to the optical lifetime, T_{opt}, to estimate the strength of the spin non-conserving transition. Different interactions are expected to play a role in inducing spin flips. Using perturbation theory, we calculated the strength of each process and find that hyperfine mixing interaction is of a comparable magnitude to T_{opt}/T_{pol} (see Table S1).

We can identify the origin of the spin-non conserving transitions by comparing the strengths of the strengths of spin flipping transitions relative to the main spin-conserving transitions.

This next section reproduces the analysis in [3]. For the spin-orbit interaction we can compute this strength by taking the ratio between the spin orbit splitting and the crystal field splitting:

$$\frac{\langle g,\downarrow|H_{SO}|e,\uparrow\rangle}{\langle g,\uparrow|H_{SO}|e,\uparrow\rangle} \approx \frac{\Delta_{SO}}{\Delta_{CR}} \tag{4.1}$$

Given that $g_{g,e}\mu_B B_z \gg a^x_{g,e}$ we can estimate the strength of the hyperfine interaction based off of [68], using the following equation:

$$\frac{\langle g,\downarrow|H_{HF,g}|e,\uparrow\rangle}{\langle g,\uparrow|H_{HF,g}|e,\uparrow\rangle} \approx \frac{a^x_g}{2g_g\mu_B B_z} I_{\mp} \frac{\langle g,\downarrow|H_{HF,e}|e,\uparrow\rangle}{\langle g,\uparrow|H_{HF,e}|e,\uparrow\rangle} \approx \frac{a^x_e}{2g_e\mu_B B_z} \begin{cases} I_z & \alpha,\ (2,\Gamma_{5/6}) \\ I_{\pm} & \beta,\ (3,\Gamma_4) \end{cases}$$

Here $4I_z$ and $I_{\pm}$ are the nuclear operators.

The decay rate for each transition is proportional ot the transition strength squared. For the hyperfine mixing we need to account for the different transition rates for each nuclear spin state. For this analysis we assume that the nuclear spin state is fully mixed and average

Table 4.1: Spin flip rates from hyperfine mixing and spin-orbit coupling compared to T_{opt}/T_{pol}.

Defect site	$\left(\frac{\Gamma_{\uparrow\to\downarrow}}{\Gamma_{\uparrow\to\uparrow}}\right)_{HF,g}$	$\left(\frac{\Gamma_{\uparrow\to\downarrow}}{\Gamma_{\uparrow\to\uparrow}}\right)_{HF,e}$	$\left(\frac{\Gamma_{\uparrow\to\downarrow}}{\Gamma_{\uparrow\to\uparrow}}\right)_{SO}$	T_{opt}/T_{pol}
4H-α	1.8e-3	1.3e-4	4e-6	8.6e-4
4H-β	1.3e-3	6.7e-4	4e-8	9.0e-4
6H-α	1.8e-3	5.3e-6	4e-6	1.04e-3
6H-β	1.1e-3	3.8e-4	1e-8	3.2e-4

all of the transition probabilities. The estimated transition rates are given by the following equations:

$$\left(\frac{\Gamma_{\uparrow\to\downarrow}}{\Gamma_{\uparrow\to\uparrow}}\right)_{HF,g} \approx \frac{1}{2I+1}\frac{a_g^x}{2g_g\mu_B B_z}^2 \sum_m \langle m \mp 1|I_\mp|m\rangle^2 \tag{4.4}$$

$$\left(\frac{\Gamma_{\uparrow\to\downarrow}}{\Gamma_{\uparrow\to\uparrow}}\right)_{HF,e} \approx \frac{1}{2I+1}\frac{a_g^x}{2g_g\mu_B B_z}^2 \sum_m \begin{cases} \langle m|I_z|m\rangle^2 & \alpha,\ (2,\Gamma_{5/6}) \\ \langle m \pm 1|I_\pm|m\rangle^2 & \beta,\ (3,\Gamma_4) \end{cases} \tag{4.5}$$

Plugging in nuclear spin $I = 7/2$ for the matrix elements we get:

$$\frac{1}{2I+1}\sum_m \langle m \pm 1|I_\pm|m\rangle^2 = \frac{1}{2I+1}\sum_{m=-I}^{I}[I(I+1) - m(m\pm 1)] = 10.5 \tag{4.6}$$

$$\frac{1}{2I+1}\sum_m \langle m|I_z|m\rangle^2 = \frac{1}{2I+1}\sum_{m=-I}^{I} m^2 = 5.25 \tag{4.7}$$

This yields the transition rates:

$$\left(\frac{\Gamma_{\uparrow\to\downarrow}}{\Gamma_{\uparrow\to\uparrow}}\right)_{HF,g} \approx 10.5\frac{a_g^x}{2g_g\mu_B B_z}^2 \tag{4.8}$$

$$\left(\frac{\Gamma_{\uparrow\to\downarrow}}{\Gamma_{\uparrow\to\uparrow}}\right)_{HF,e} \approx \begin{cases} 5.25\frac{a_e^x}{2g_e\mu_B B_z}^2 & \alpha,\ (2,\Gamma_{5/6}) \\ 10.5\frac{a_e^x}{2g_e\mu_B B_z}^2 & \beta,\ (3,\Gamma_4) \end{cases} \tag{4.9}$$

Parameters from [68, 77, 5] were used to calculate the numerical values in 4.1. The result of this analysis is that the hyperfine interaction is the primary perturbation causing electron spin flips in the excited state. Furthermore, the contrast in the optical initialization curves lower bounds the percent spin polarization [7, 20] and can be improved in future experiments by using large magnetic field or optimizing the ensemble linewidths. The current observed spin polarizatioins of 44 to 68 percent already suffice for hole burning recovery measurements, and allow us to probe V^{4+} spin T_1 times at sub-Kelvin temperatures.

We used optical spin polarization and readout to perform all optical measurements of the vanadium defect's spin T_1. Defects in solids are particularly susceptible to spin-lattice relaxation. Understanding the temperature dependent T_1 will allow us to understand the mechanism behind the vanadium defect's relaxation and also discover if there is an operating temperature feasible for coherent operation. Recent work has shown a T_1 of V^{4+} in the 4H-α site as long as 25 s at $\sim$100 mK [5]. In our experimments, all-optical hole burning recovery measurements were used to measure the spin T_1.

Figure 4.12 illustrates the evolution of the ground state spin populations and time-domain fluorescence signal during the spectral hole burning recovery experiment. At the beginning of the first hole burning pulse the fluorescence is large, due to a large ground state spin population. Towards the end of the pulse, the fluorescence has decayed due to the population having been shelved in a dark state. During the delay time between pulses relaxation according to a T_1 process occurs. At the beginning of the probe pulse, the fluorescence will increase due to partially recovery of the ground state population. After a time greater than a few T_1, the initial fluorescence of the probe pulse should match that of the pump pulse. At shorter times, it will not be as bright due to some of the population remaining in the dark state. The recovery of the probe pulse fluorescence will follow an exponential curve with time constant T_1. At the end of the probe pulse the fluorescence will have once again decayed due to repetition of the shelving process.

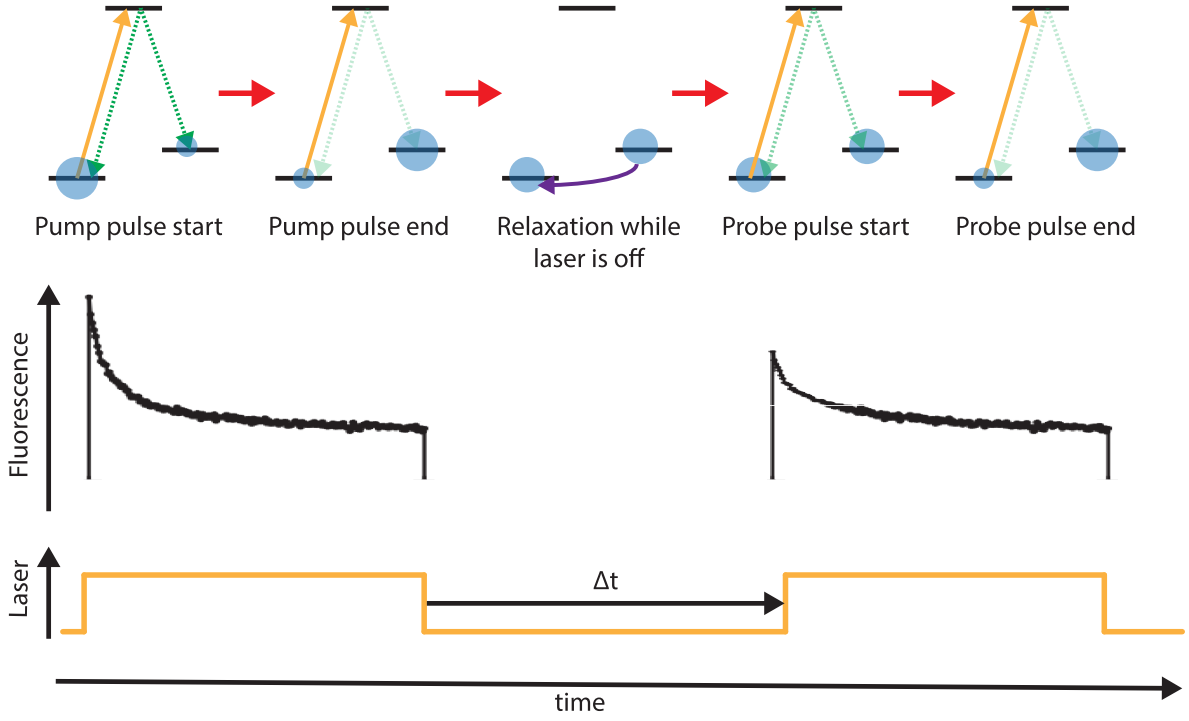

Figure 4.12: Schematic illustrating evolution of the ground state spin populations and time-domain fluorescence signal during the spectral hole burning recovery experiment.

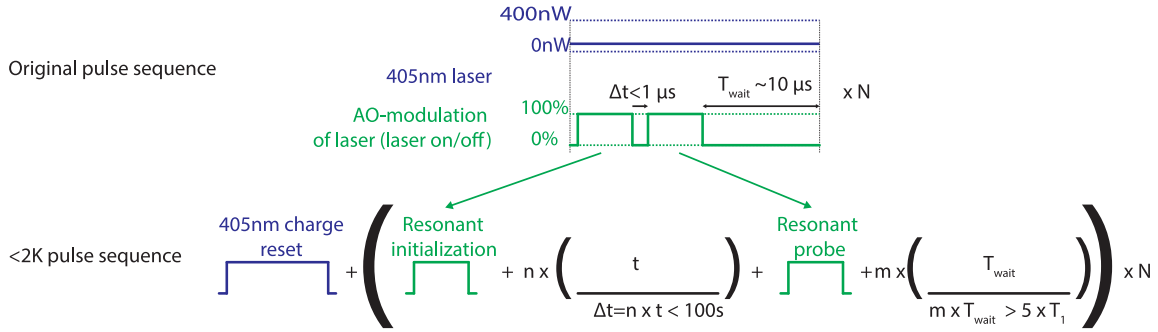

Figure 4.13: The pulse sequence used to measure T_1 is modified from the pulse sequence used to perform spectral hole burning recovery at elevated temperatures.

Figure 4.13 shows how the pulse sequence used to measure T_1 is modified from the pulse sequence used to perform spectral hole burning recovery at elevated temperatures. Previous experiments measuring $T_1 < 1\mu s$ at 3.6K [77] combined a pulsed a resonant laser with weak continuous-wave illumination at 405nm. Because the 405nm laser mixes the spin state and can therefore affect the measured T_1, we modified this sequence to pulse the 405nm laser every N repetitions. Furthermore, the spin lifetime is greater than 4 orders of magnitude longer at milikelvin temperatures, requiring pulse sequence delay times greater than 100s, and wait times between repetitions greater than 5 times the T_1. However, it is difficult to generate such a long waveform with sufficient resolution in the time domain without running into hardware memory limits. We solve this problem by breaking our sequence into a series of nested loops, where the wait and delay times are short null sequences repeated n and m times respectively.

Spectral hole burning recovery measurements are performed at different sample temperatures to extract the temperature dependent spin T_1. Efficient spin polarization was observed even at the highest temperatures reached in our experiments. This is due to a long T_1 even at the upper end of our temperature range of interest, which had $T_1 \sim 10\mu s$. Because this is significantly longer than the optical lifetime we can still perform efficient optical spin polarization and readout. The spin T_1 observed for the 4H-α site was also observed to increase

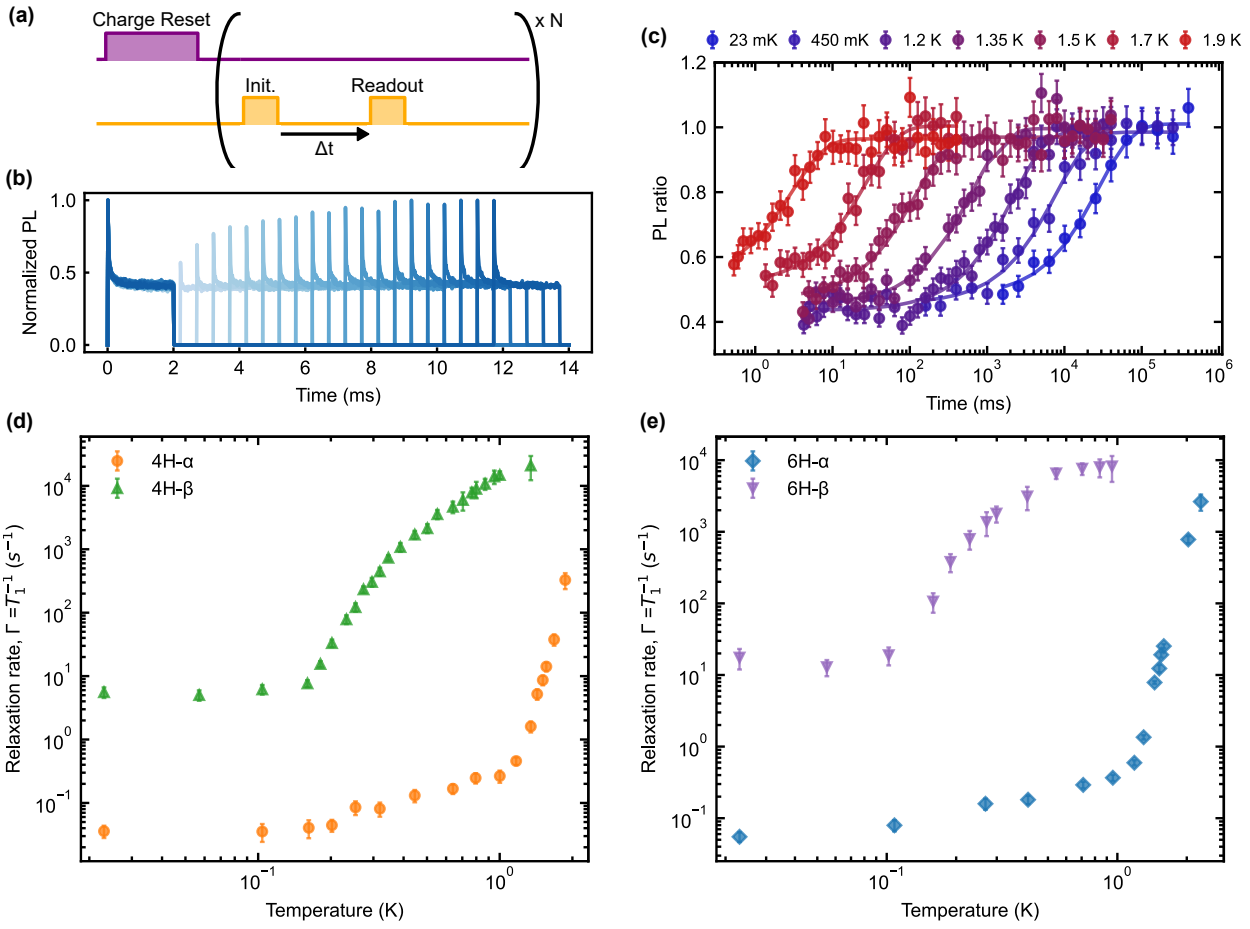

Figure 4.14: Figure reproduced from [3]. Hole burning recovery experiments and temperature dependent spin relaxation rates.

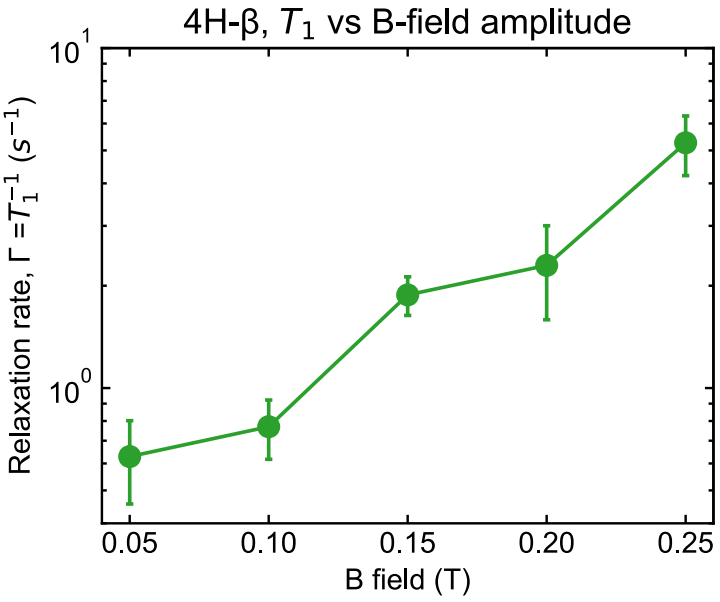

Figure 4.15: 4H-β spin relaxation rate $\Gamma = T_1^{-1}$ as a function of external magnetic field. Figure is reproduced from [3].

by four orders of magnitude over the temperature range of 1.9 K to 23 mK (see Fig. 4.14 (c)). The temperature dependent spin relaxation rates are plotted in Fig. 4.14 (d) and (e). A strong temperature dependence is observed acorss all sites, leading to long T_1 times. The 4H-α sites show a maximum T_1 of 27.9 s, and the 6H-β site shows the shortest T_1 of 57.1 ms. For the 4H-β site it is also possible to increase the T_1 time by lowering the magnitude of the external magnetic field, as shown in Fig. 4.15.

One concern with developing a spin-photon interface based on the vanadium defect is the fact that vanadium has 100 percent isotopic abundance of nuclear spin $I = 7/2$. The prescence of this additional nuclear spin could possible cause relaxation of the electron spin, through electron-nuclear spin flip flop operations. However, observation of long spin T_1 times suggest that the nuclear spin does not limit the T_1 times to a level that is unsufficient for coherent control. In fact, it is advantageous to have long T_1 times in the prescence of the vanadium hyperfine interaction, as the hyperfine interaction modifies magnetic selection

rules to permit magnetic resonance of the spin state with magnetic fields polarized along the c-axis [27, 26, 77]. Therefore, V^{4+} has potential for coherent microwave spin control in addition to optical initialization and readout.

4.4 Fitting temperature-dependent spin relaxation mechanisms

Understanding of the spin-relaxation mechanism can also be inferred from the temperature dependent T_1 data [62, 1]. Fitting the temperature dependent spin relaxation rates allows us to determine the mechanisms causing the spin relaxation. The three processes are the direct phonon process, the Raman process, and the Orbach process. These processes are depicted schematically in Fig. 4.16 (a).In the direct phonon process, the spin decays directly through emission of a phonon. In the Raman process relaxation occurs through phonon scattering off of a virtual excited state. In the Orbach process decay occurs through resonant absorption and emission of phonons with an excited state [52]. Each process has a different functional dependence with temperature. The direct phonon process has a $1/T_1 \propto T$ depdence. The Raman process has a power law dependence $1/T_1 \propto T^n$ where n = 5 or 9 for our Kramers doublet spin states [62, 27]. The Orbach process has a dependence $1/T_1 \propto e^{-\Delta/k_B T}$ where Δ is the energy splitting of the resonant excited state and k_B is the Boltzmann constant. The full model for the spin relaxation rate is given by :

$$1/T_1 = A_c + A_D T + A_R T^n + A_O e^{-\Delta/k_B T}, n = 5, 9 \tag{4.10}$$

where A_c is a temperature independent contribution and A_D, A_R, and A_O are the amplitude of the direct, Raman, and Orbach processes, respectively.

We fit the temperature dependent spin T_1 data for each site as shown in Fig. 4.16 (b)-(e). A statistical F-test was used to determine whether the terms in the model contribute statistically to the fit, justifying our fit of the direct, Orbach, and temperature-dependent

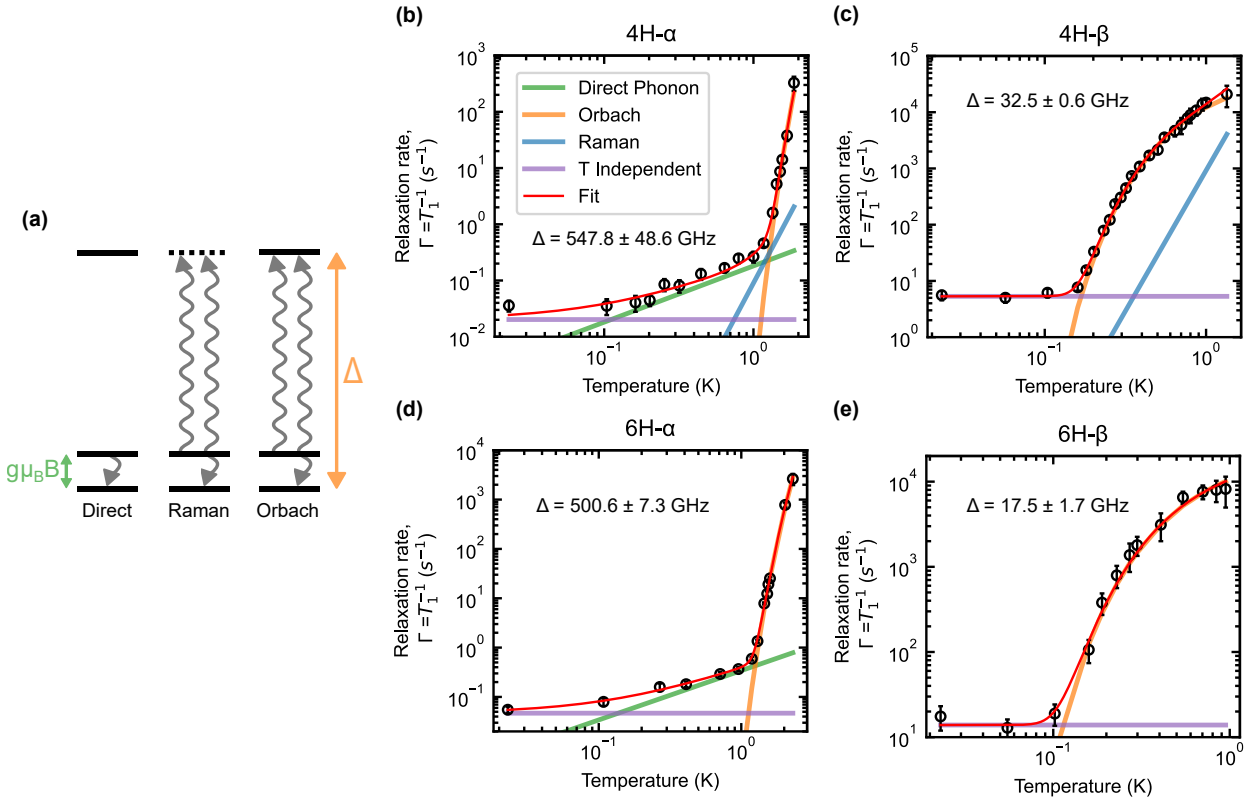

Figure 4.16: Spin relaxation processes for V^{4+} in SiC. Figure is reproduced from reference [3].

relaxation processes. number of data points and V is the number of fit parameters. However, the F-test suggests that the fit Raman terms do not contribute statistically. The F-ratio was computed using $F = \frac{(SS_1 - SS_2)/(df_1 - df_2)}{SS_2/df_2}$. Here SS_1 and SS_2 represent the residual sum of squares for each model. df_1 and df_2 are the degrees of freedom computed as $N - V$, where N is the. After calculating the F-ratio and degrees of freedom, we can look up the p-value and determine which model provides a better statistical fit.

We can see that below T < 100 mK, the measured spin T_1 saturates, which suggests that the sample does not thermalize well to the lowest temperatures reachable by the dilution refrigerator. We confirm the contribution of the direct phonon process at these temperatures by probing the magnetic field dependence of the T_1 for the 4H-β site [1, 19]. For the α sites, a linear dependence on temperature for 100 mK $< T <$ 1 K, indicates the direct phonon process, while it is clear that above 1 K the relaxation is dominated by the Orbach process. We are also able to compare the obtained energy splittings from the fit to the orbital state splittings observed in the PLE spetra (see Table 4.3), and can conclude that the higher lying ground state participating in the Orbach processes is the GS2 orbiital level.

The spin T_1 may be extended using similar techniques to the group-IV color centers in diamond [37, 58, 72]. One possible method would be to use nanostructures, such as phononic crystals or nanoparticles [45, 41], to modify the phononic density of states to restrict the number of available phonons resonant with the GS1-GS2 transition. This could be feasible since near surface V^{4+} ions were found to be stable [77, 16]. We propose the use of strain to

Table 4.2: Identification of the relevant excited state in the Orbach process. Fitting Eq. (1) to the temperature dependent spin relaxation rates ($1/T_1$), we obtain Δ from the Orbach term that is consistent with the GS1-GS2 splitting measured from PLE spectroscopy for all measured sites. All reported errors represent 1 SE from the fit.

Site	GS1-GS2 (GHz)	Δ (GHz)
4H-α	530	547.8 ± 48.6
4H-β	43	32.5 ± 0.6
6H-α	525	500.6 ± 7.3
6H-β	25	17.5 ± 1.7

increase the GS1-GS2 orbital splitting to, subsequently reduce the spin relaxation through the Orbach process and enable higher temperature operation [49, 63, 31, 65, 71]. Figure 4.18, computed from equation 4.10, shows the temperature and orbital splitting that can be used to achieve $T_1 > 1$ ms at elevated temperatures, and the strain required at 4K to achieve a given orbital splitting and relaxation rate.

Table 4.3: Table reproduced from [3]. Comparison of the fitted Orbach energy splitting and the GS1-GS2 splitting extracted from PLE data.

Site	GS1-GS2 (GHz)	Δ (GHz)
4H-α	530	547.8 $\pm$ 48.6
4H-β	43	32.5 $\pm$ 0.6
6H-α	525	500.6 $\pm$ 7.3
6H-β	25	17.5 $\pm$ 1.7

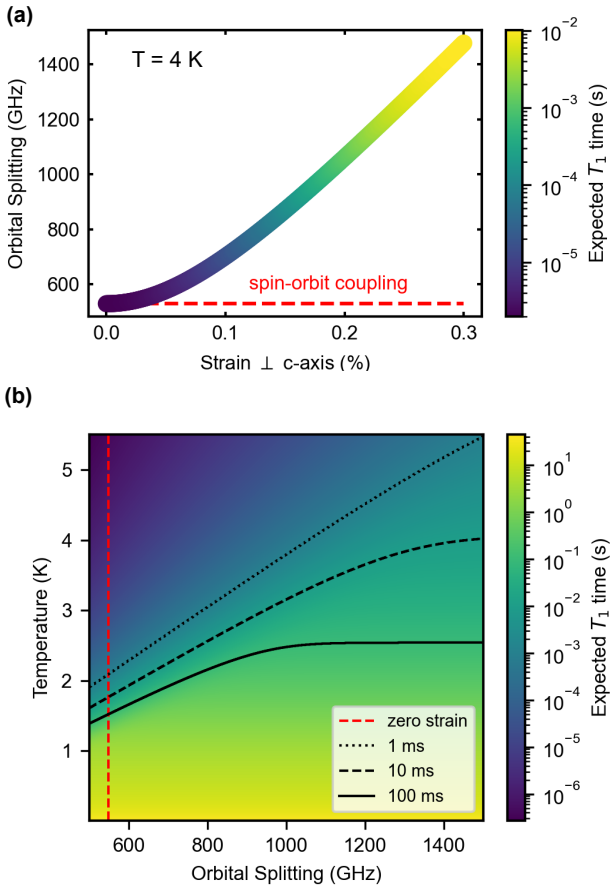

Figure 4.17: Figure reproduced from [3]. Larger orbital splittings can enable longer spin T_1 at higher operation temperatures.

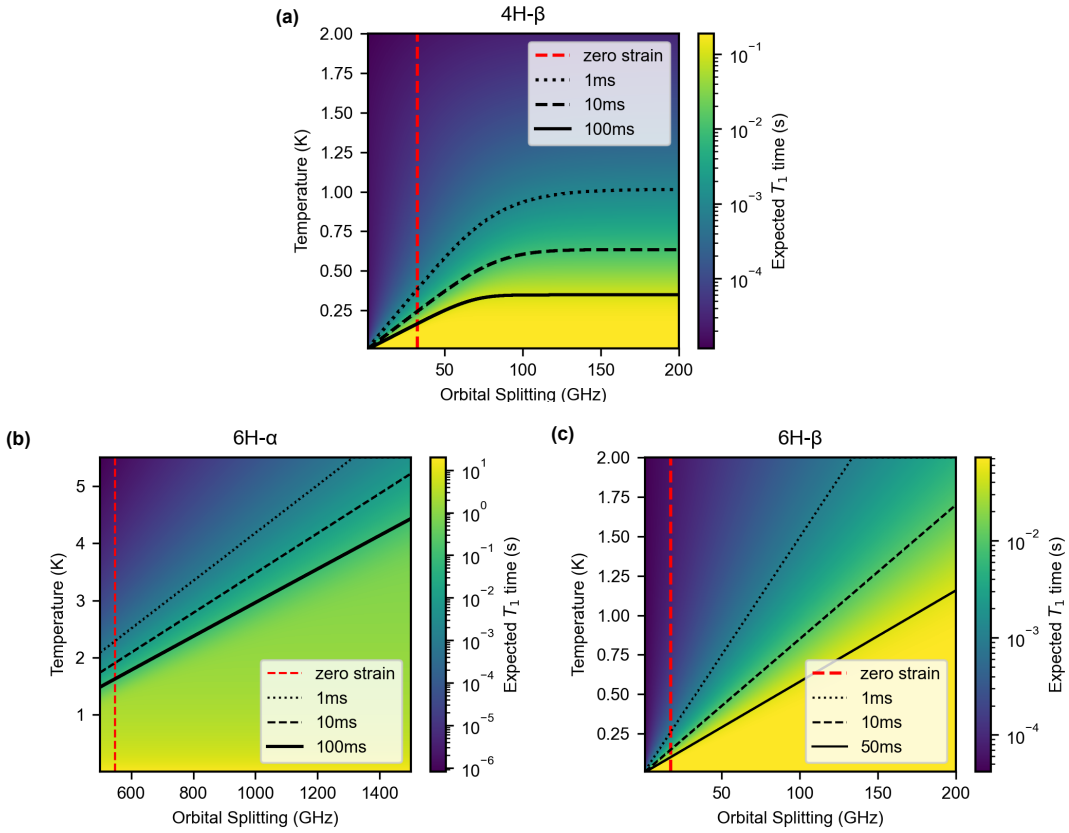

Figure 4.18: Figure reproduced from [3]. Strain required to achieve a given orbital splitting and T_1 at 4 Kelvin for the 4H-α site.

Table 4.4: Fit parameters for the phonon relaxation processes. The table is reproduced from reference [3].

site	A_c	A_D	A_R	n	A_O	Δ
4H-α	0.02±0.01	0.18±0.04	0.09±0.05	5	2.90e8±4.21e8	547.84±48.58
4H-β	5.32±0.60	0.00±7.29	9.21e2±6.00e2	5	5.80e4±4.42e3	32.51±0.56
6H-α	0.05±0.00	0.34±0.02	-	-	9.63e7±2.04e7	500.60±7.27
6H-β	13.89±5.50	0.00±9.65e1	-	-	2.45e4±8.95e3	17.51±1.71

CHAPTER 5

STRAIN SUSCEPTIBILITY OF V^{4+} IN SILICON CARBIDE

5.1 Introduction and theory

The vanadium defect in silicon carbide (SiC:V4+) has recently drawn interest for its potential application for quantum communication with its optical emission in the telecom O-band at wavelengths between 1278-1389 nm [77]. The SiC:V4+ substitutes for the silicon atom in SiC and therefore can be positioned at the quasi-hexagonal (h) or quasi-cubic (k) site in 4H:SiC, and at the quasi-hexagonal (h) or at two quasi-cubic (k1,k2) sites in 6H SiC. The quasi-cubic sites mainly have tetrahedral (Td) symmetry, and the quasi-hexagonal sites mainly have C3v symmetry. Here, we are interested in the interaction between the spin/orbital states of the vanadium defect and the strain environment in the SiC. The lattice deformation due to strain leads to a strong mixing or shift in the orbital states.

Identifying defects with large strain coupling is promising for optically-detected strain sensing and engineering novel hybrid quantum systems. Strain sensing has been shown with other defects such as the NV center and the silicon vacancy in diamond where dispersive readout of the phase imprinted on a spin during acoustic driving can be performed with ODMR. On the other hand, a hybrid optomechanical system can be formed by an optically active defect incorporated in an optomechanical cavity. This system can be used to acoustically drive the defect, acoustically modulate its coherence and relaxation properties, and prepare interesting phononic states with telecom light. Furthermore it is fundamentally interesting to identify an optically interfaced defect with large strain coupling from the perspective of engineering strong acoustic coupling with a resonator, which has yet to be shown. The telecom transition of SiC:V is promising for integration of such hybrid quantum systems with quantum networks. Possible experiments include the generation of acoustic sidebands on the microwave and optical transitions and acoustic Rabi and Ramsey experiments as have

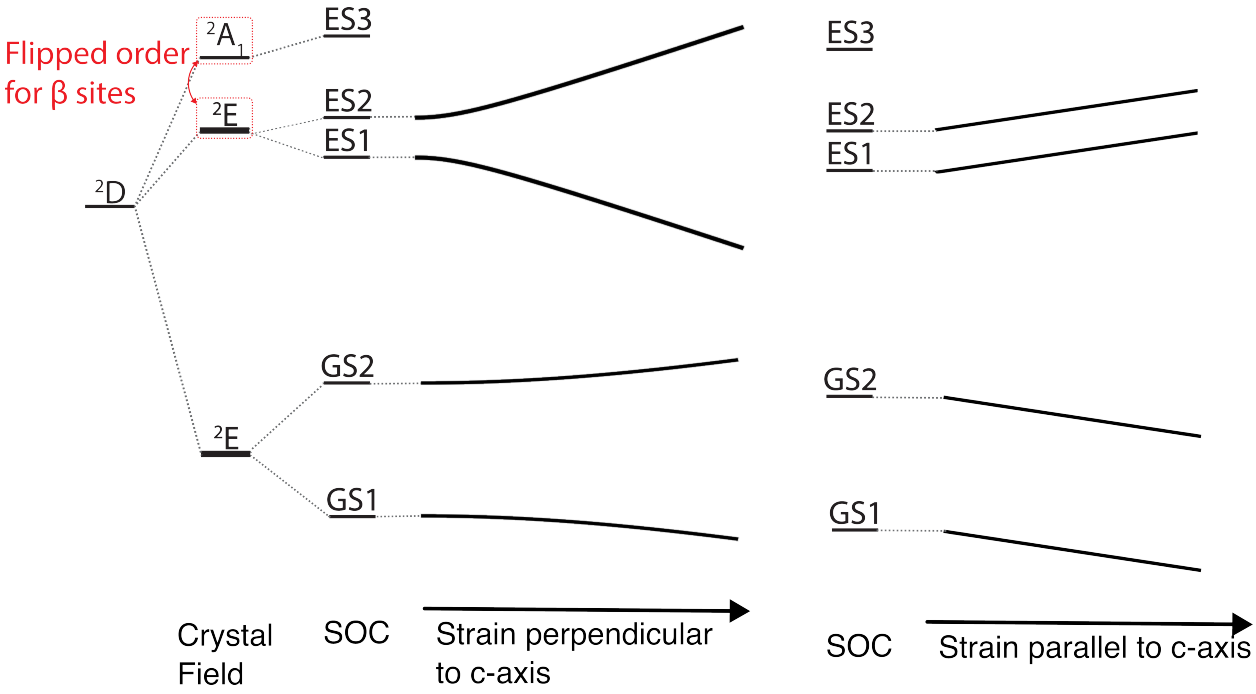

Figure 5.1: Illustration of interactions contributing to orbital level splitting in V^{4+} in silicon carbide.

been similarly performed for the silicon vacancy in diamond [48].

Figure 5.1 depicts the orbital level splitting due to strain in accordance with [71]. The optical ground and excited states are determined by C_{3v} crystal field of the lattice, giving rise to an orbital doublet in the ground state and an orbital singlet and doublet in the excited state. For the α sites in 4H and 6H silicon carbide, the orbital doublet lies below the orbital singlet. For the β sites the converse is true. The number of excited states also differ for each site, as in the α sites the singlet level lies above the conduction band, and in the 4H-β site the doublet lies above the conduction band. Spin orbit coupling further splits the degeneracy of the orbital doublet states. The effect of strain depends on the direction of applied strain. When the energy of the strain interaction with the orbital exceeds the spin orbit coupling, for strain applied perpendicular to the c-axis, the energy splitting between orbital doublet states increases linearly. Strain applied parallel to the c-axis increases the energy splitting between the ground and excited state orbitals.

5.2 Experimental setup and strain tuning optical transitions

To characterize the strain we applied controlled strain to a thin membrane mounted on a linear piezo. Commerical laser and mechanical polishing was used to create nominally 100 micron thick membranes of SiC for both the 4H and 6H polytypes, originating from bulk samples with vanadium densities of $1.3e^17cm^{-3}$ and $1.4e^17cm^{-3}$ respectively. We mounted the membranes to piezoelectric actuators using stycast 2850FT epoxy. A similar method with a linear piezo was used by our group to estimate the optical and spin-strain susceptibility of divacancy defects (VV0) in 4H silicon carbide[23]. The piezo in our setup applies a tensile force to the membrane and creates a resulting strain perpendicular to the SiC c-axis.

The experiments were performed in a cryostat at a temperature of 4K, and optical spectra was measured through photoluminescence excitation (PLE). The experimental setup is shown in Fig. 5.2.The strain applied by the piezos has been modeled using FEM simulations (Comsol).

By applying voltages between 0 and 150V we can observe distinct shifts of the optical spectral lines on the order of 10s of GHz. The capability to deterministically tune emission wavelengths is important for meeting resonance conditions between individual defects, for instance, if you wanted to perform two photon interference. For most transitions, can observe a shift of a few 10s of GHz or more for the individual optical transitions.

5.3 Measuring orbital strain susceptibilities and modulation of optical dipole

Using a model of the strain Hamiltonian on the basis of the orbital/pseudospin states, we fit this Hamiltonian to experimental shifts in the optical wavelength that we observe as a function of controlled strain, and extract the fitted susceptibilities. We find close agreement with theoretical model based on the defect symmetry and susceptibilities estimated from

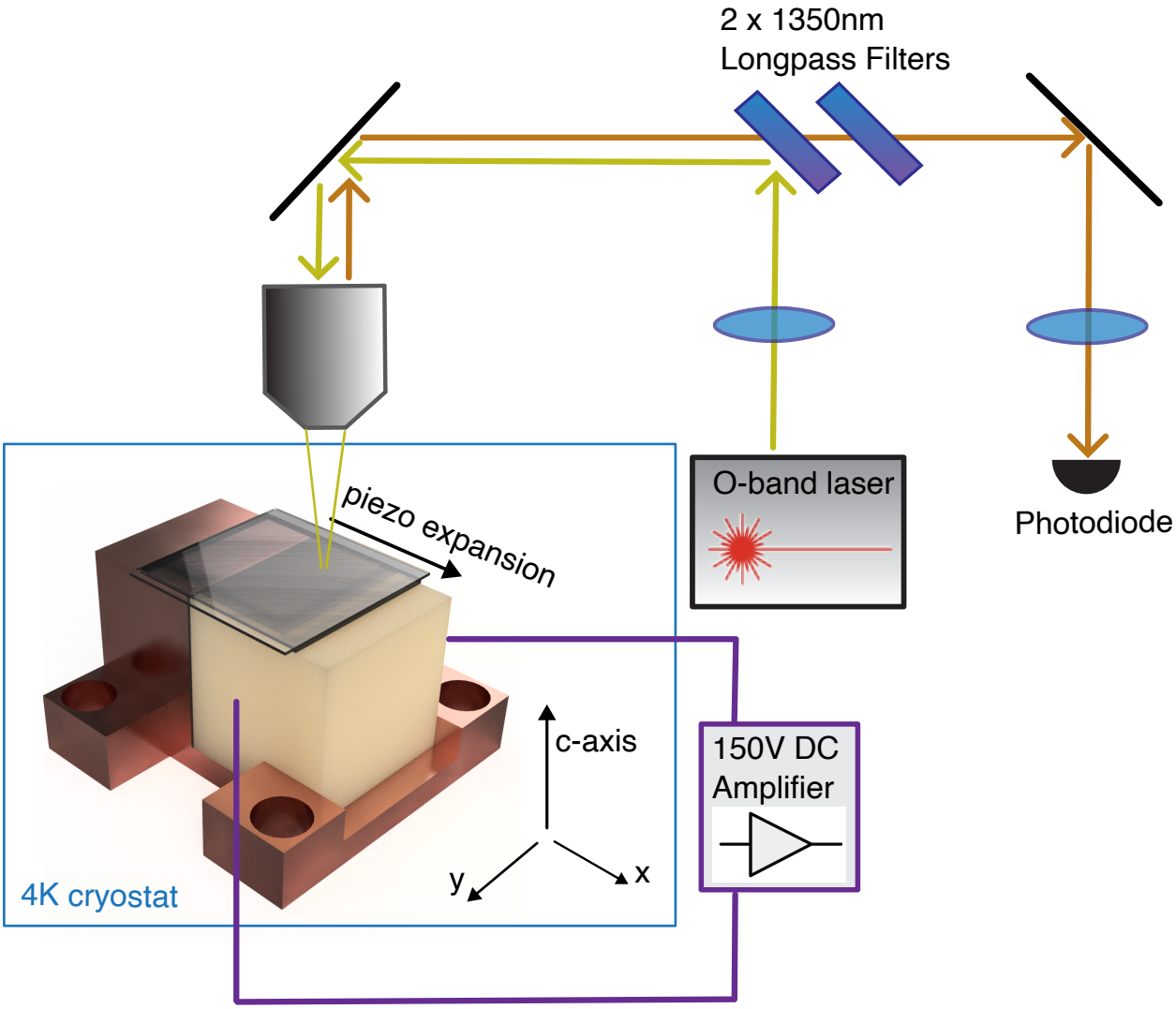

Figure 5.2: Setup used to measure strain susceptibility of V^{4+} in silicon carbide.

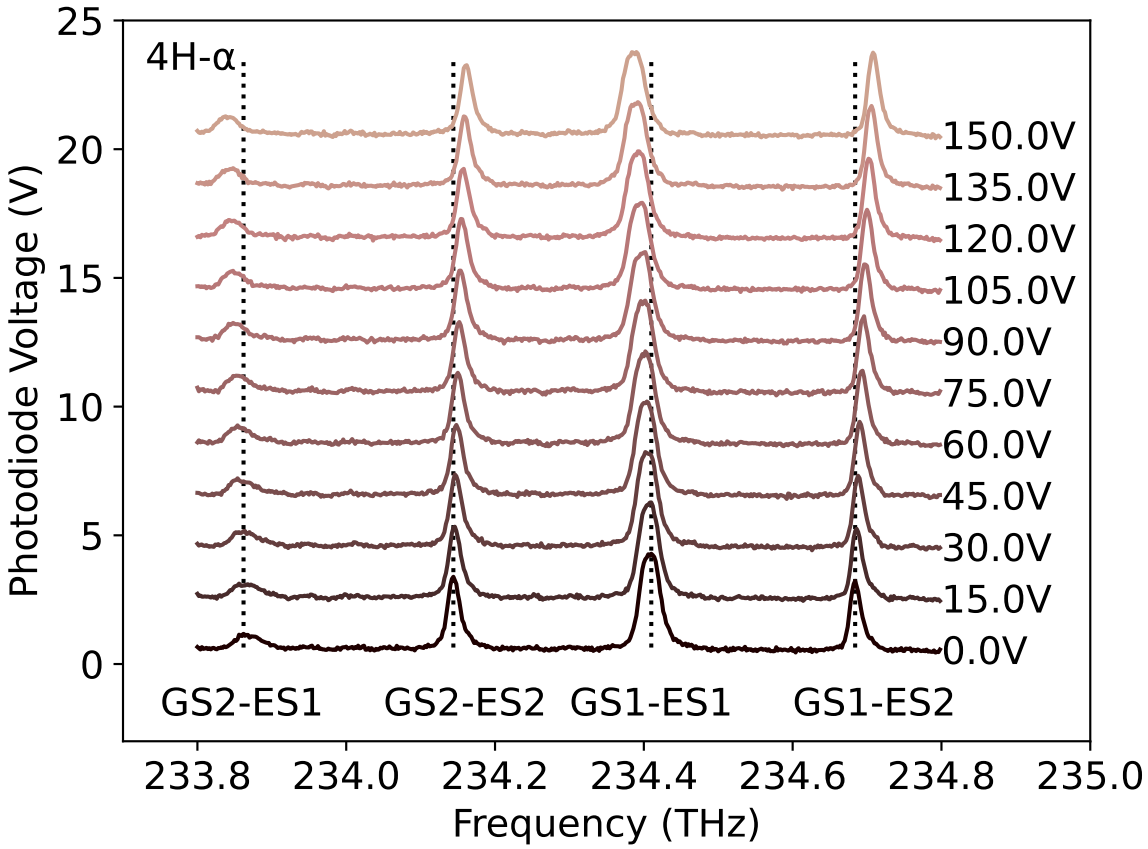

Figure 5.3: Strain tuning of the optical transitions for the 4H-alpha site of vanadium in silicon carbide.

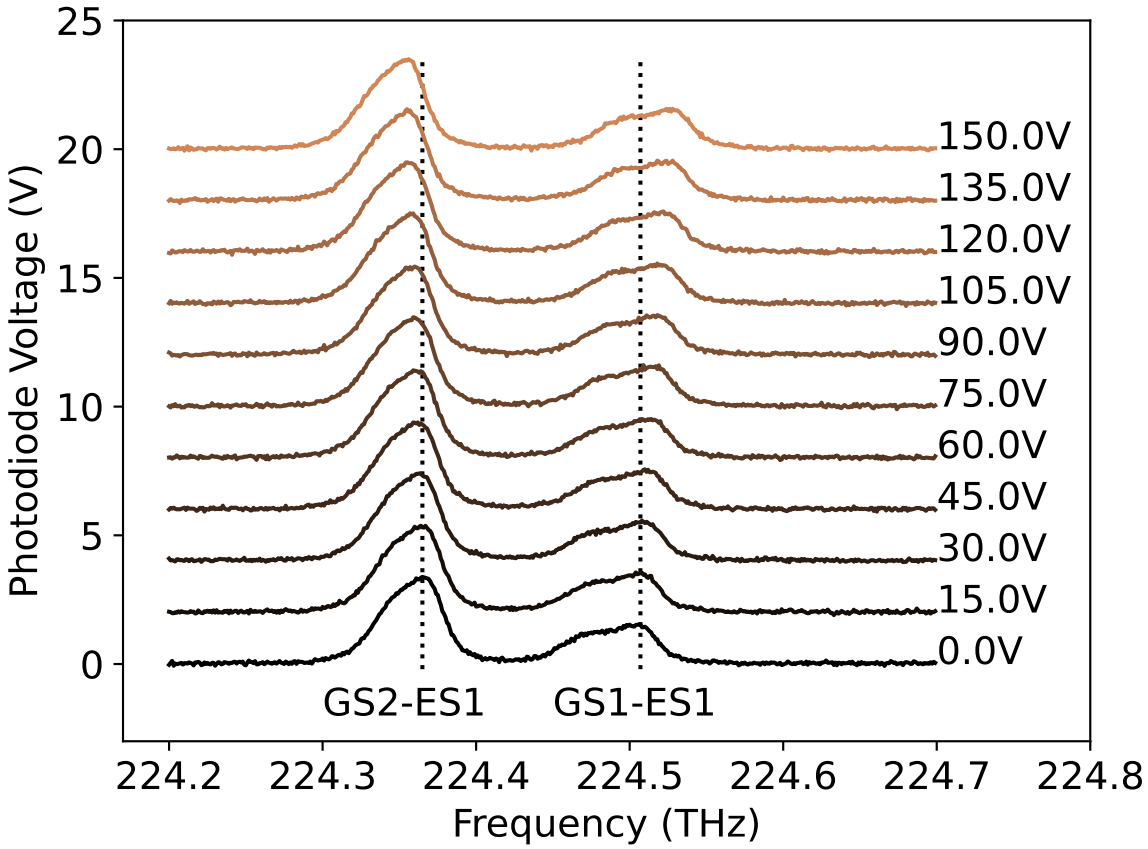

Figure 5.4: Strain tuning of the optical transitions for the 4H-beta site of vanadium in silicon carbide.

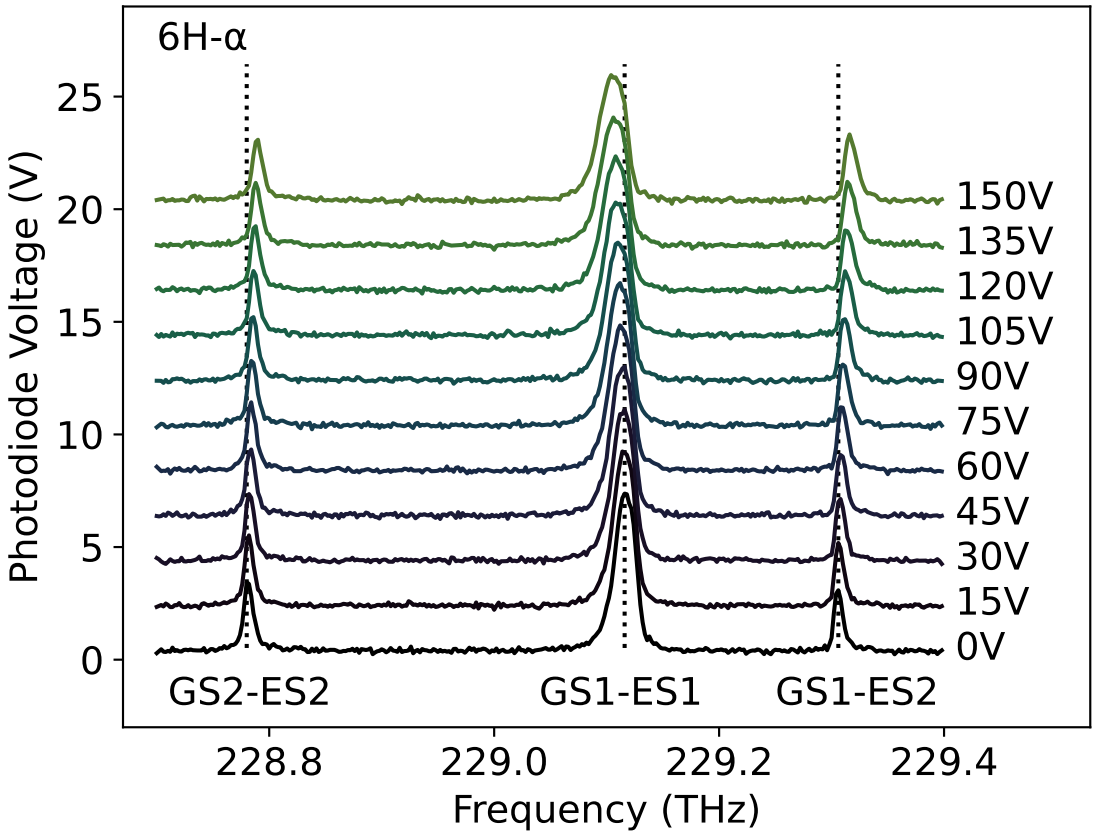

Figure 5.5: Strain tuning of the optical transitions for the 6H-alpha site of vanadium in silicon carbide.

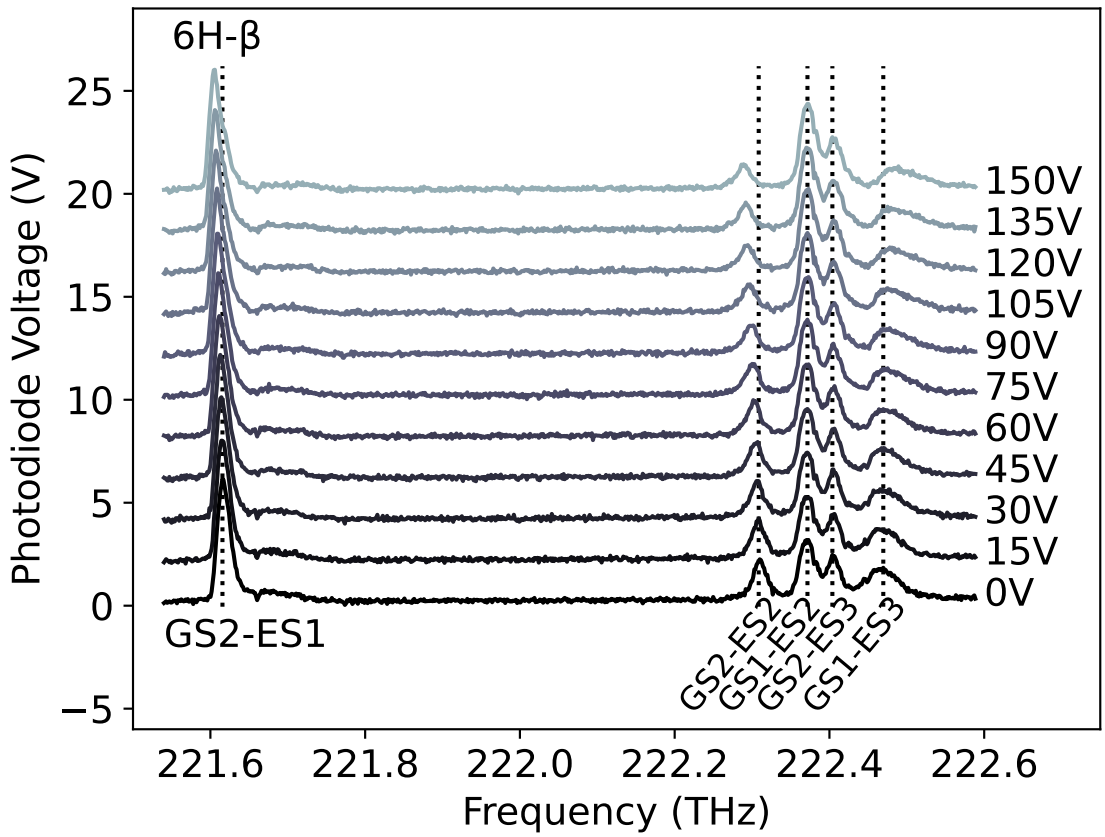

Figure 5.6: Strain tuning of the optical transitions for the 6H-beta site of vanadium in silicon carbide.

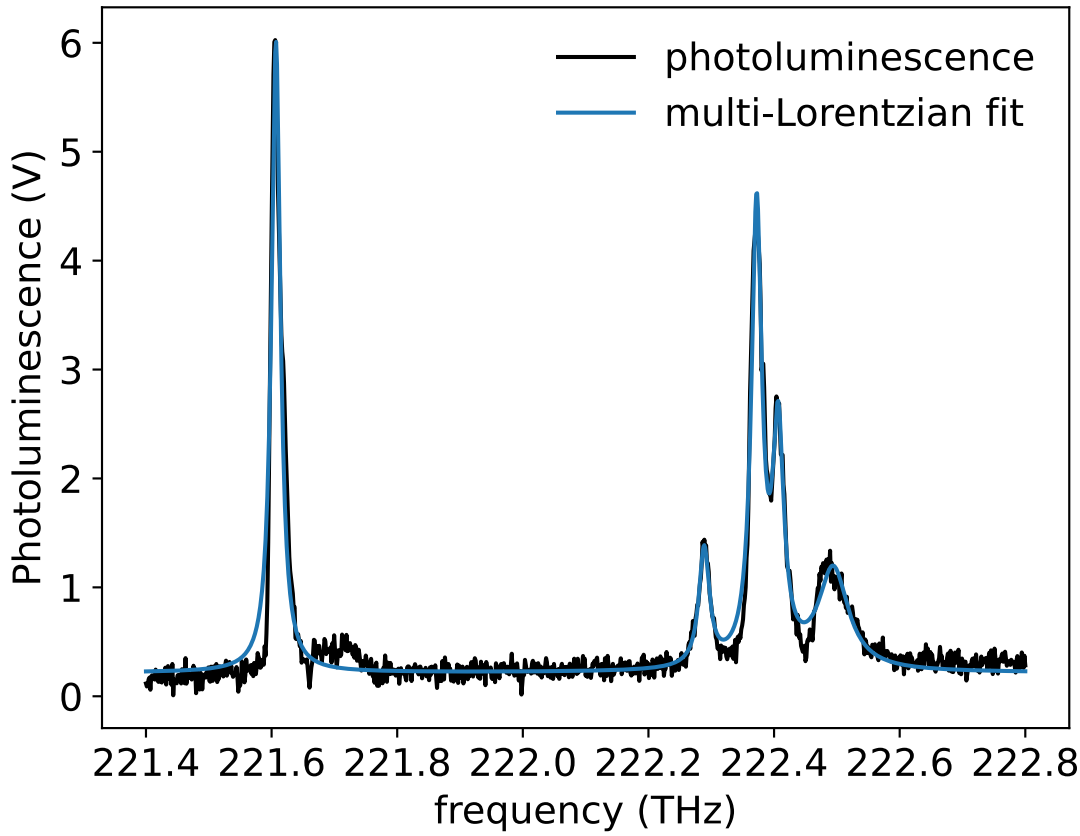

Figure 5.7: Multi-Lorentzian of the 6H-β spectrum at an applied piezo voltage of 150V. The GS1-ES1 transition is extremely weak and not fit.

DFT calculations of the defect wavefunctions.

Multi-Lorentzian fits are used to fit the optical transition center frequencies and peak intensities from the optical spectra for each site for each voltage. The standard fit errors for the center frequencies and Lorentzian amplitudes are used for the error bar in subsequent fits of the strain coupling parameters and intensities with strain. In general each peak is fit to a Lorentzian, with the exception of the 4H-β site. This is shown in 5.7 for the 6H-β site at an applied piezo voltage of 150V. We also observe a very weak GS1-ES1 transition for this site, and exclude it from the fit.

Figure 5.8 shows the fit of the 4H-β site at an applied piezo voltage of 150V. For the

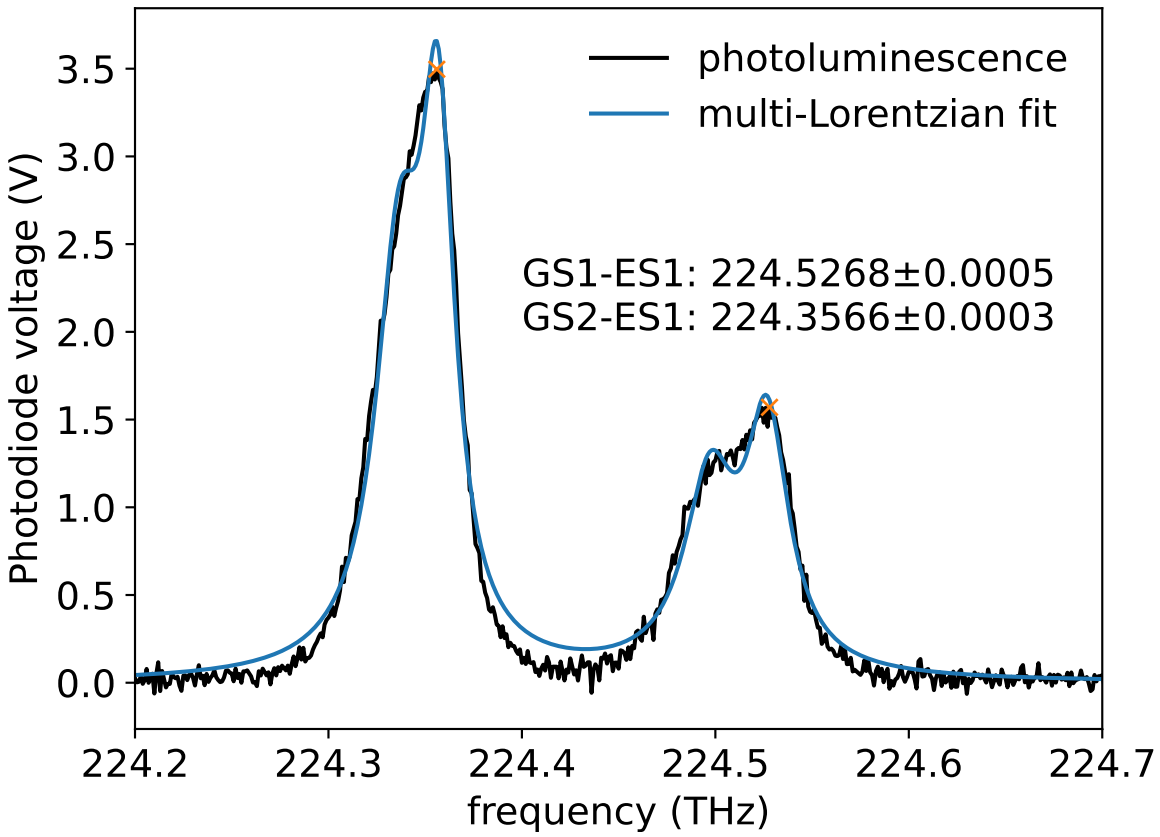

Figure 5.8: Optical spectra of the 4H-β site for an applied piezo voltage of 150V. A fit of two Lorentzian's to each peak is used to extract the optical transition center frequencies and peak intensities for the 4H-β site.

4H beta site we observe an asymmetric broadening of the lineshape into two peaks, at all voltages. To deal with this spectra, we fit two Lorentzians to each peak and use the frequencies and amplitudes corresponding to the highest peak (higher energy) peak to represent the transition. The chosen peak is indicated by the orange "x" in 5.8. Since this broadening occurs even at 0V, it may originate from the mechanical lapping process used to generate the 4H silicon carbide membrane or from an inhomogeneous effect of strain on the isotopically shifted peaks within the inhomogeneous line [77], with the strain induced in the membrane by thermal contraction of different elements (the piezo, stycast, and silicon carbide) during cooling of the sample to 4K. The mechanical lapping process may have generated microfractures within the material leading to distinct populations that experience slightly different strain magnitudes within our laser spot. However, it is worth mentioning that the spectra of the 4H-α site, which show a similar magnitude strain shift, were taken at this same position during the same cooldown, indicating that this pronounced effect on the optical spectra is pronounced due to unique interactions of the β site with strain. Clearly the double Lorentzian fits to the 4H-β site incur additional error on the peak amplitudes and wavelengths, which suggests a more complicated lineshape may be preferred to fit the spectrum, such as a Voigt lineshape. While this data and fitting procedure is sufficient for the subsequent analysis, a more detailed study on the lineshape of the 4H-β site under strain is warranted.

To fit the orbital strain susceptibilities it is necessary to know what strain is produced for a given voltage applied by the piezo. Calibration of strain is a central challenge in research related to the strain-susceptibility of defects. It is difficult to integrate strain gauges, and perform precise and accurate strain measurements in cryogenic experimental setups. As a result, most calibration methods rely on finite element modeling, either directly using strain estimates from simulation or combining strain estimates with experimentally measured parameters. In particular, a few studies have calibrated strain by combining the observed shifts of optical spectra with an FEM estimated strain from thermal contraction as a the

Table 5.1: Strain components at the experimental position estimated from FEM simulations of the thermal contraction piezo membrane setup.

Strain component	Strain
$\left(\epsilon_{xx}+\epsilon_{yy}\right)/2$	-2.784e-3
ϵ_{xz}	1.871e-6
ϵ_{yz}	5.548e-6
$\left(\epsilon_{yy}-\epsilon_{xx}\right)/2$	9.972e-5
ϵ_{xy}	-2.066e-4
ϵ_{zz}	-1.997e-4

sample is cooled to cryogenic temperatures. Knowing a single optical lineshift and estimated strain at a given experimental condition suffices to obtain a calibration of the strain, so long as the applied strain in linear in the experimental variable, and the optical shift is linear in the applied strain. We choose to employ a similar technique as we can already observe small shifts of the orbital splittings from their bulk value after cooling down our sample to 4 K.

For our calibration, we simulated the experimmental setup as closely as possible. In our setup a 6 mm x 6 mm x 100 μm 4H silicon carbide membrane is epoxied (using Stycast 2850FT epoxy) to a 5 mm x 5 mm x 5 mm PZT piezo from Thorlabs. The piezo is also epoxied to a copper mount, and the sample is glued such that $\sim$2 mm of the sample are epoxied to the copper, and $\sim$3 mm of the sample are expoxied to the piezo. The epoxy thickness below the membrane nominally $\sim$ 100 μm. A rendering of the 3D Comsol model used for the strain calibration is shown in Fig. 5.9. Thermal contraction coefficients for PZT, the Stycast epoxy, and the silicon carbide membrane are included in the model, which simulates cooling the system from room temperature to 4 K. We extract the strain calculated at the experimental measurement position shown in 5.10. Figure 5.11 shows the ϵ_{xy} strain component as a function of the position on the piezo and membrane surface. Table 5.1 shows these simulated strain components at the experimental position at 4K. Here we are using linear combinations of the strain components in accordance with the C_{3v} symmmetry of the defect, as discussed in [71].

We next use the model of the orbital eigenstate energies as a function of strain, given in

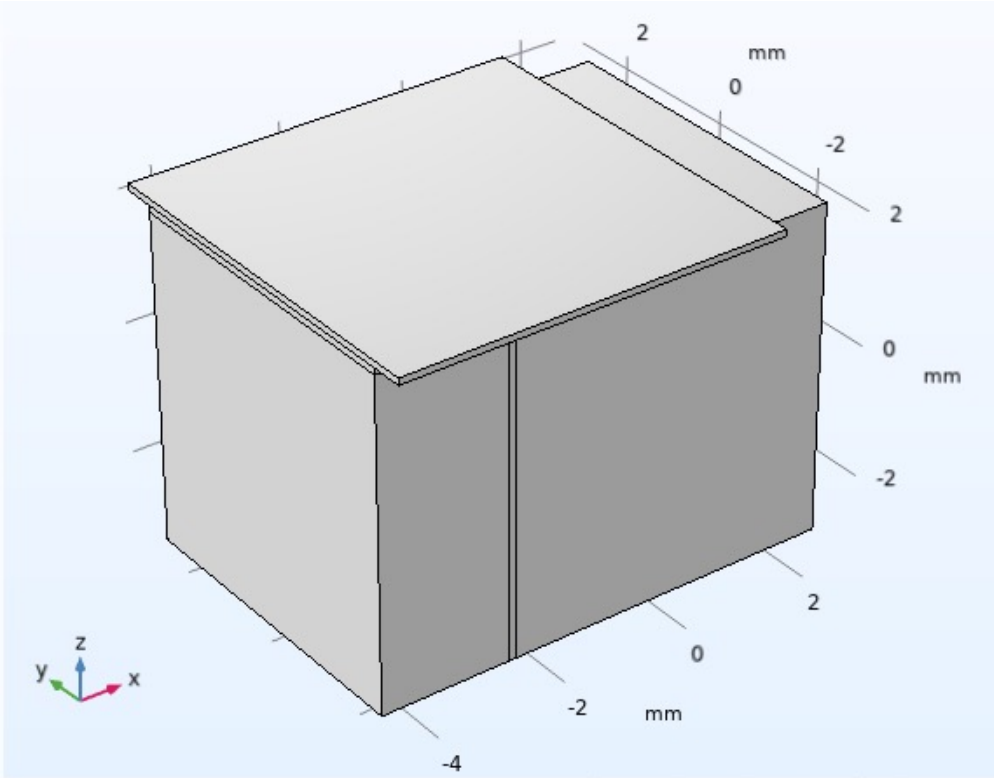

Figure 5.9: Rendering of 3D Comsol model used for strain calibration.

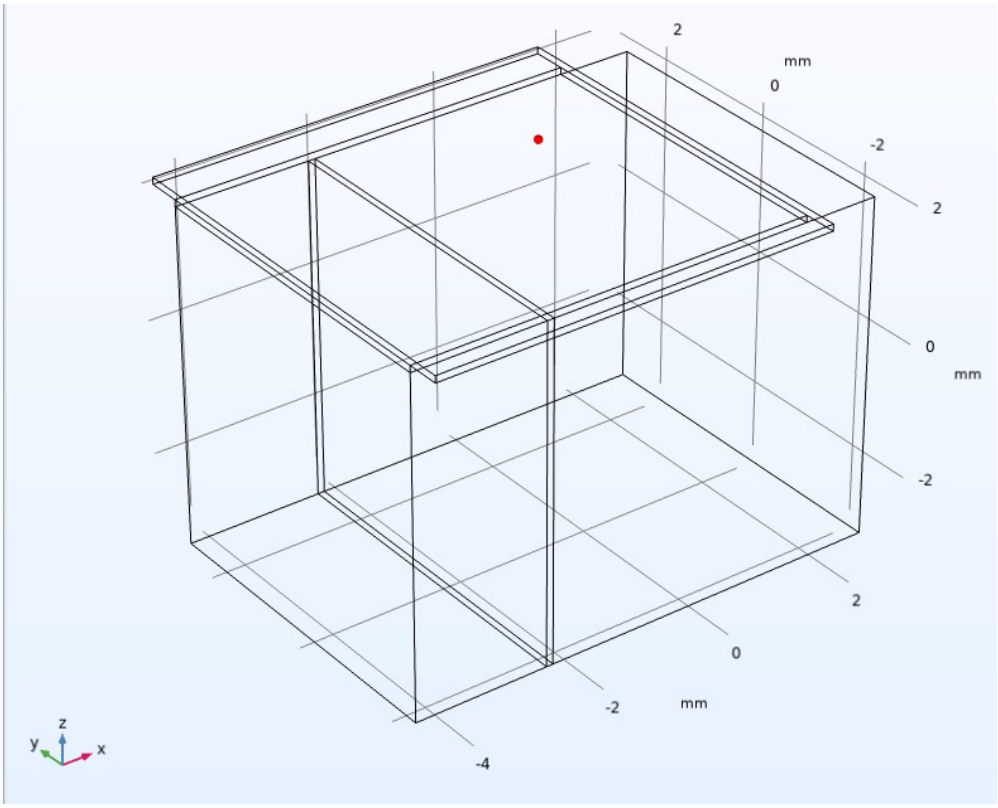

Figure 5.10: Illustration of the location of the laser spot in our experiment. The same location was selected in Comsol simluations to estimate the strain.

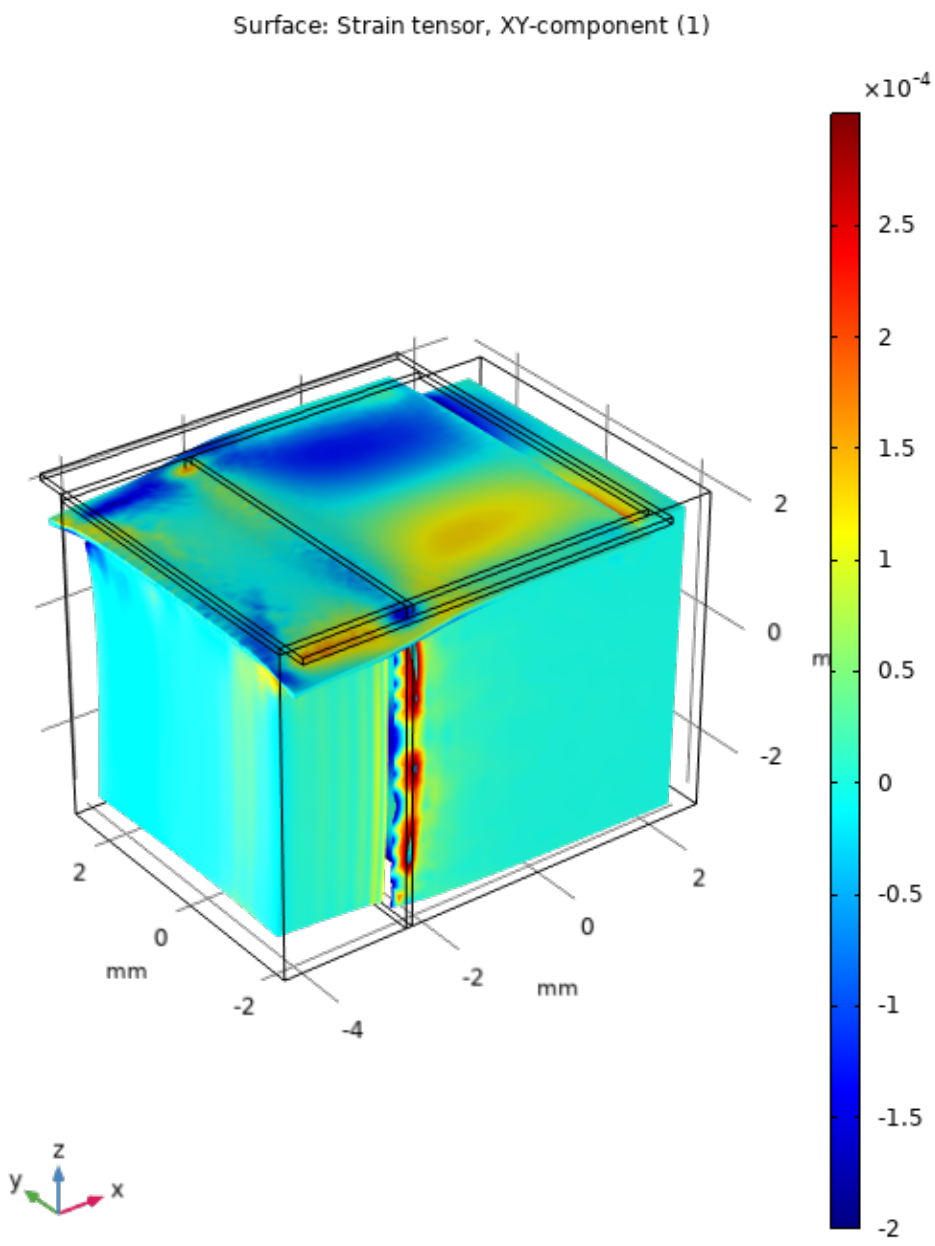

Figure 5.11: Plot of the XY strain component from Comsol simulations along the surface of the membrane and piezo.

reference [71] to estimate the additional orbital splitting from thermal contraction strain at 0V. The energy eigenvalues presented in reference [71] for the 4H-α site are:

$$E_n = \epsilon_n + \epsilon^z_{nn} + \frac{1}{2}\text{sign}\left(\lambda_n n^z\right)\Delta_n \tag{5.1}$$

$$\Delta_n = \sqrt{\left(\lambda^z_{nn}\right)^2 + 4\left(\epsilon^x_{nn}\right)^2 + 4\left(\epsilon^y_{nn}\right)^2} \tag{5.2}$$

$$\epsilon^x_{nm} = s^x_{nm}\epsilon_{xz} + s^x_{nm}{}'\frac{\left(\epsilon_{yy} - \epsilon_{xx}\right)}{2} \tag{5.3}$$

$$\epsilon^y_{nm} = s^x_{nm}\epsilon_{yz} + s^x_{nm}{}'\epsilon_{xy} \tag{5.4}$$

$$\epsilon^z_{nm} = s^z_{nm}\epsilon_{zz} + s^z_{nm}{}'\frac{\left(\epsilon_{yy} + \epsilon_{xx}\right)}{2} \tag{5.5}$$

Here ϵ_n is the energy of the crystal field state n (for $n = 1$ this is 0). $\lambda_n n^z$ is the spin orbit coupling within orbital doublet n. ϵ^x_{nn} and ϵ^y_{nn} are reduced components of the strain tensor in accordance with the C_{3v} symmetry of the defect. The units of the reduced strain components are in energy, and represent the energy shifts resulting from linear combinations of strain values and the strain orbital coupling parameters s^x_{nm}, $s^x_{nm}{}'$, s^z_{nm}, and $s^z_{nm}{}'$. It is clear from equation 5.1, that only the ϵ^x_{nn} and ϵ^y_{nn} components contribute to the orbital splitting, while the ϵ^z_{nn} components increase the splitting between the ground and excited state doublets. Even though our data in 5.1 shows significant values for $\frac{(\epsilon_{yy}+\epsilon_{xx})}{2}$ and ϵ_{zz}, we ignore those strain contributions in our calibration since and choose to use the values for the 4H-α GS1-GS2 orbital splitting. Also our experiment preferentially applies a $\frac{(\epsilon_{yy}-\epsilon_{xx})}{2}$ strain, so we focus on understanding the strains from thermal contraction that couple to $s^x_{nn}{}'$. However, it will ultimately be important to characterize s^z_{nm} and $s^z_{nm}{}'$ for applications

focusing on the tuning of optical wavelengths.

The additional GS1-GS2 splitting from strain induced by thermal contraction can be written as:

$$\Delta_1^{(0V)} = \sqrt{\left(\lambda_{11}^z\right)^2 + 4\left(\epsilon_{11}^{x(0V)}\right)^2 + 4\left(\epsilon_{11}^{y(0V)}\right)^2} \tag{5.6}$$

For $\epsilon_{11}^{x(0V)}$ and $\epsilon_{11}^{y(0V)}$ terms we consider the two largest strain components (except for those which couple to s_{nn}^z and $s_{nn}^z{}'$ terms, which can be seen from simulation to both couple to $s_{11}^x{}'$. These are $\left(\frac{\epsilon_{yy}-\epsilon_{xx}}{2}\right)^{(0V)}$ and $\epsilon_{xy}^{(0V)}$. Subtracting the spin orbit coupling we estimate an initial strain 107.9 GHz due to thermal contraction. Likewise we add our strain terms in quadrature according to the equation, and get an initial strain of 2.294e-4. This allows us to estimate $s_{11}^x{}' = 235.2$ THz/strain. We can solve for the strain/V ratio by substituting (strain/V)×(150V) into the equation for $\epsilon_{11}^{x(150V)}$, and substituting the GS1-GS2 splitting observed at 150V. The $\epsilon_{11}^{y(0V)}$ term remains unchanged as it is due purely to thermal contraction and not applied voltage to the piezo. Solving for (strain/V) yields 7.627e-7 strain/V. We use this strain to voltage relationship and the initial strain to form the piezo strain calibration in our remaining experiments.

For the 4H-α sample we fit the $s_{nn}^x{}'$ parameter. From our Comsol simulations for the spot probed on the membrane, we expect the $\frac{(\epsilon_{xx}-\epsilon_{yy})}{2}$ component to be an order of magnitude larger than the next largest strain component that contributes to the orbital splitting. Therefore we ignore the s_{nn}^x, $s_{nn}^y{}'$, and s_{nn}^y parameters under the assumption that the strain coupling to those parameters is negligible.

We also show how the photon selection rules are be impacted by added strain for transitions between states of different orbital symmetry. In agreement with the theoretical model, we showed the ability modulate the brightness of transitions by about 10 percent as a function of strain.

We showed qualitative agreement between the observed brightness change and the theo-

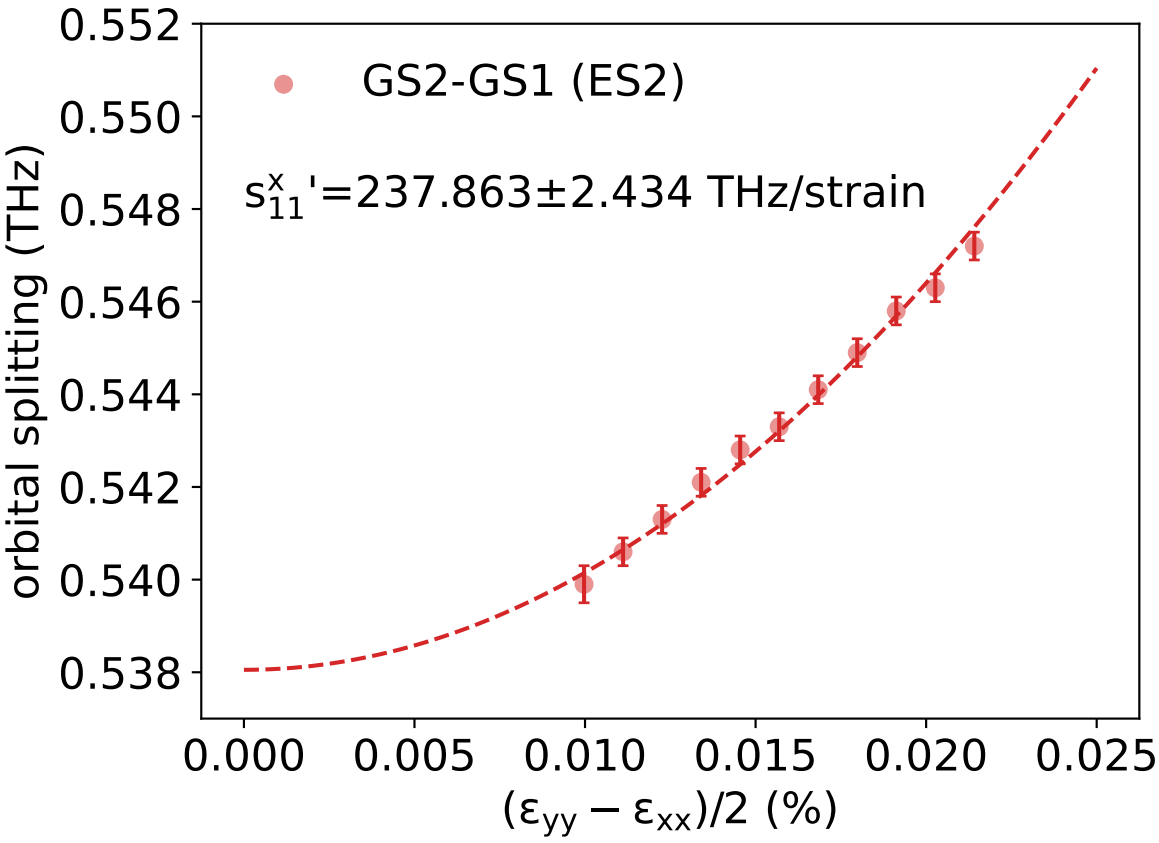

Figure 5.12: Fit of GS2-GS1 orbital splitting versus $\frac{\epsilon_{yy}-\epsilon_{xx}}{2}$ strain. The orbital splitting is calculated by taking the difference in energy between optical transitions to ES2. The ground state orbital doublet strain susceptibility $s_{11}^{x}{}' = 237.863 \pm 2.434$ THz/strain for the 4H-alpha site.

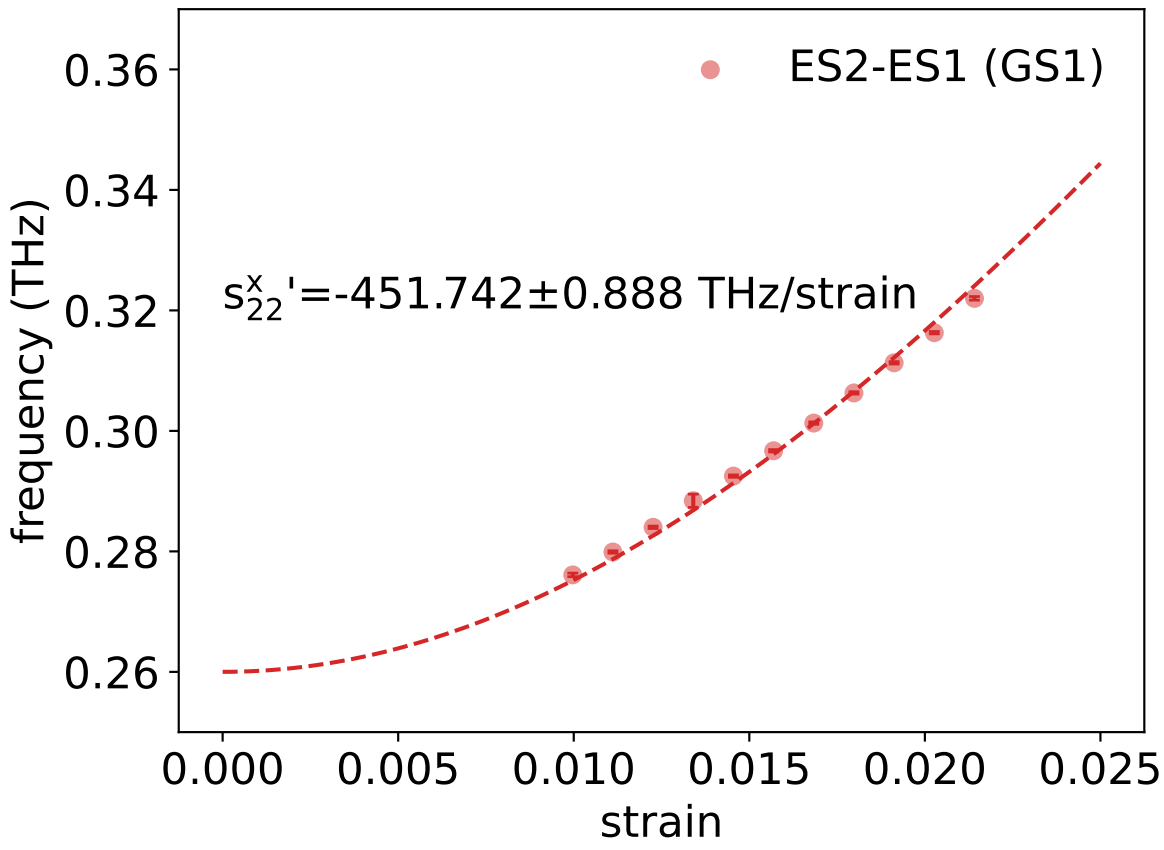

Figure 5.13: Fit of ES2-ES1 orbital splitting versus $\frac{\epsilon_{yy}-\epsilon_{xx}}{2}$ strain. The orbital splitting is calculated by taking the difference in energy between optical transitions from GS1. The excited state orbital doublet strain susceptibility $s_{22}^{x\prime} = -451.742 \pm 0.888$ THz/strain for the 4H-alpha site.

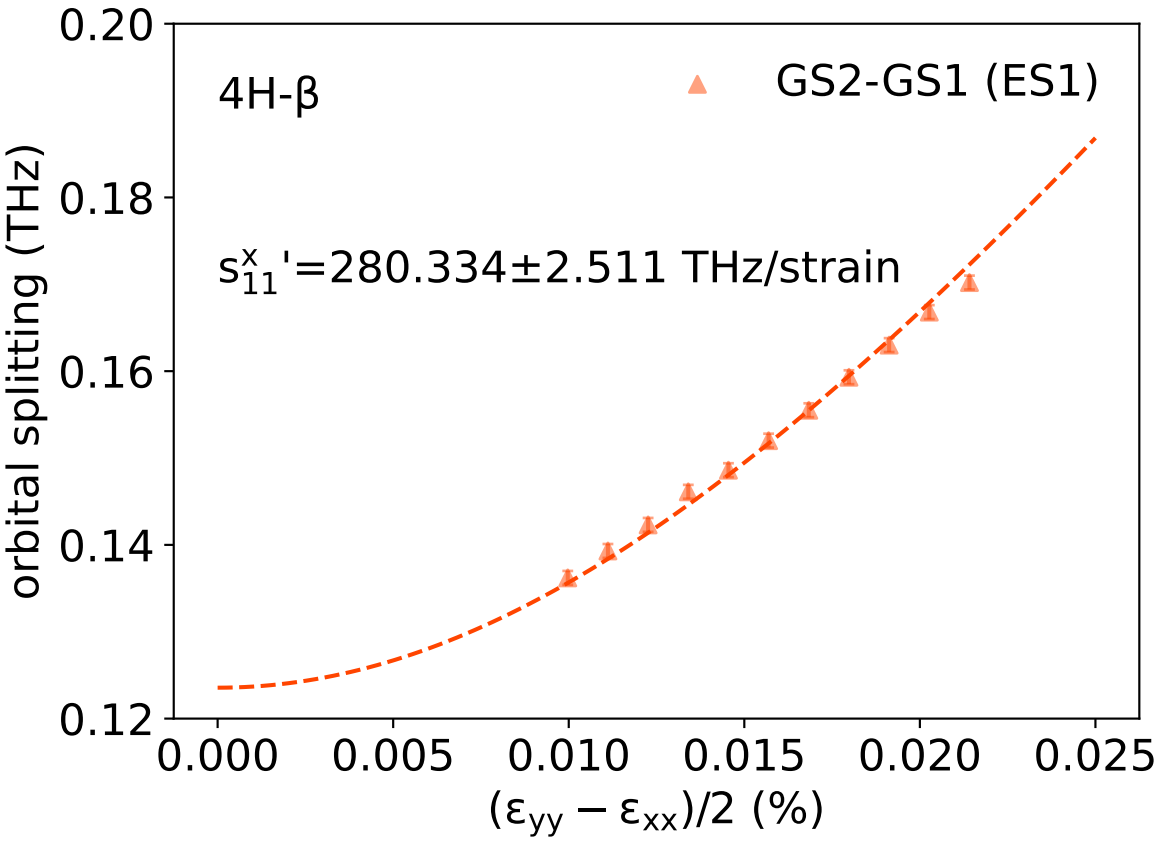

Figure 5.14: Fit of GS2-GS1 orbital splitting versus $\frac{\epsilon_{yy}-\epsilon_{xx}}{2}$ strain. The orbital splitting is calculated by taking the difference in energy between optical transitions to ES1. The ground state orbital doublet strain susceptibility $s_{11}^{x}{}' = 280.301 \pm 2.511$ THz/strain for the 4H-beta site.

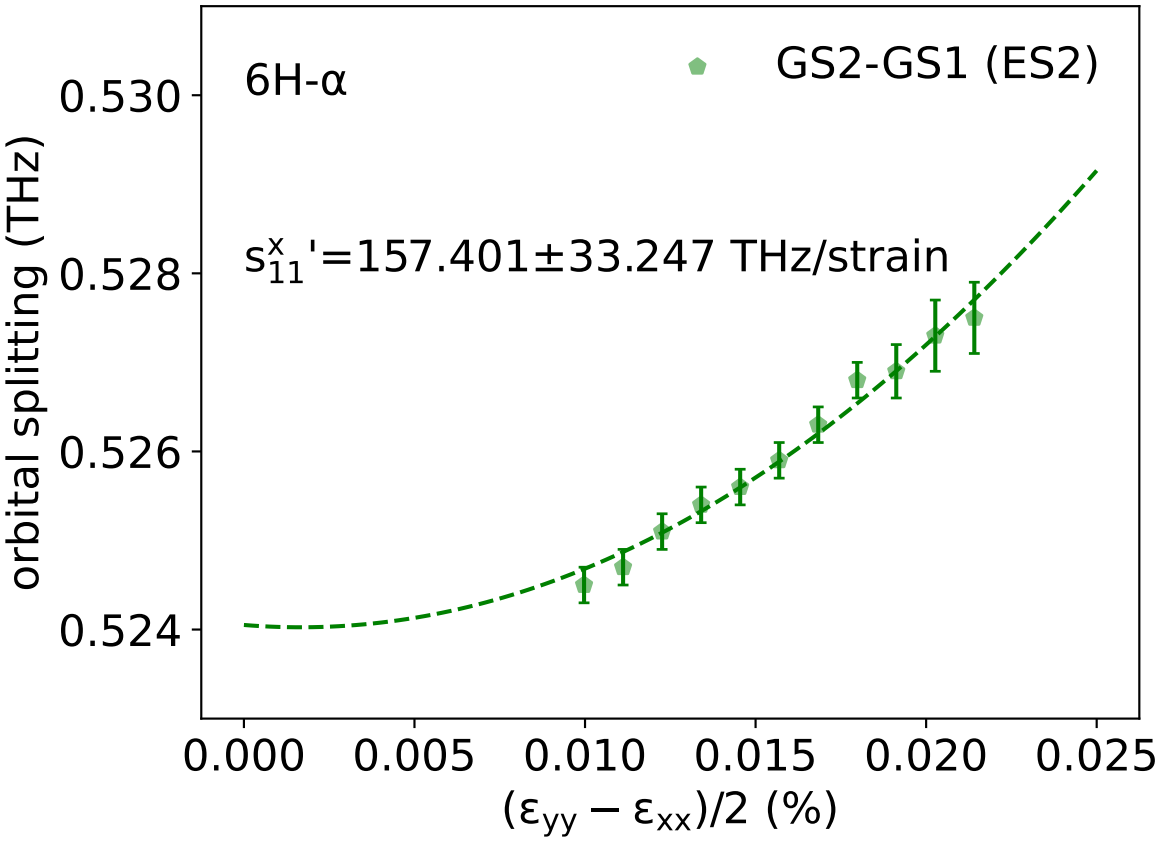

Figure 5.15: Fit of GS2-GS1 orbital splitting versus $\frac{\epsilon_{yy}-\epsilon_{xx}}{2}$ strain. The orbital splitting is calculated by taking the difference in energy between optical transitions to ES2. The ground state orbital doublet strain susceptibility $s_{11}^x{}' = 157.401 \pm 33.247$ THz/strain for the 6H-alpha site.

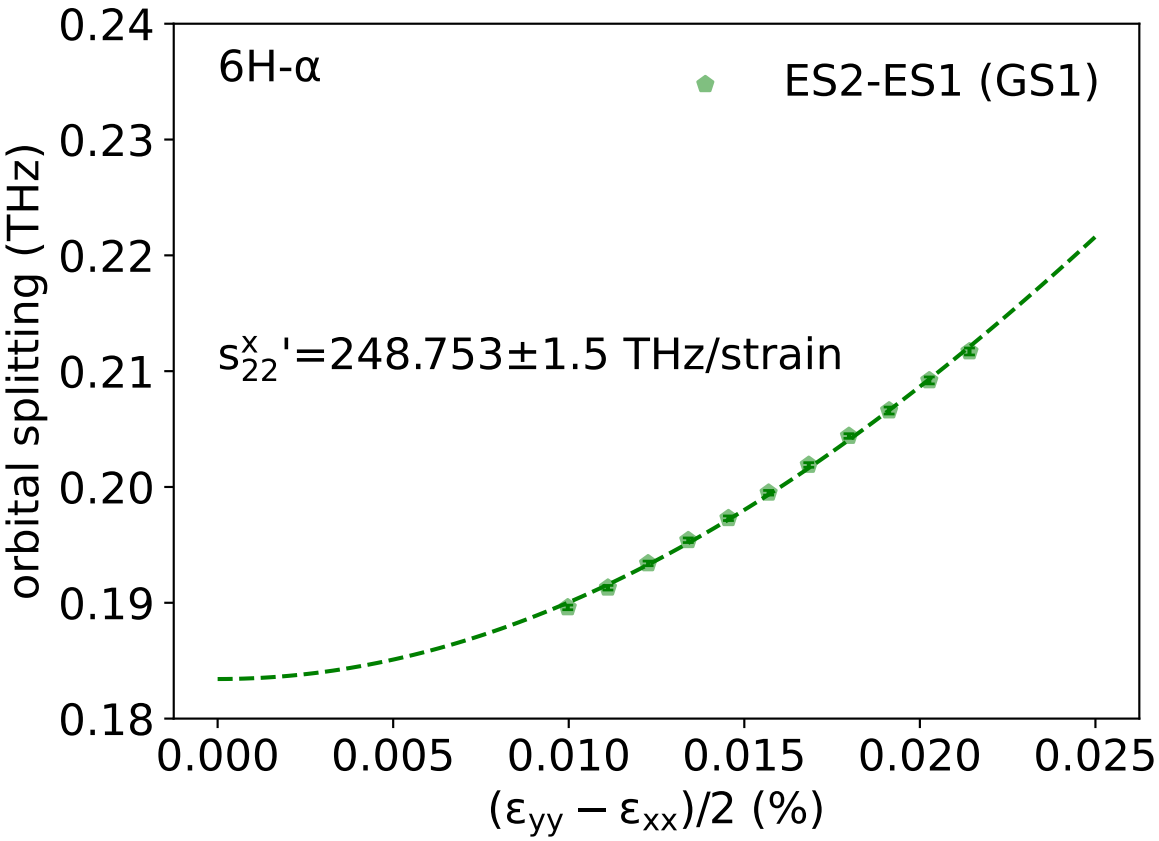

Figure 5.16: Fit of ES2-ES1 orbital splitting versus $\frac{\epsilon_{yy}-\epsilon_{xx}}{2}$ strain. The orbital splitting is calculated by taking the difference in energy between optical transitions from GS1. The excited state orbital doublet strain susceptibility $s_{22}^{x}{}' = 248.753 \pm 1.500$ THz/strain for the 6H-alpha site.

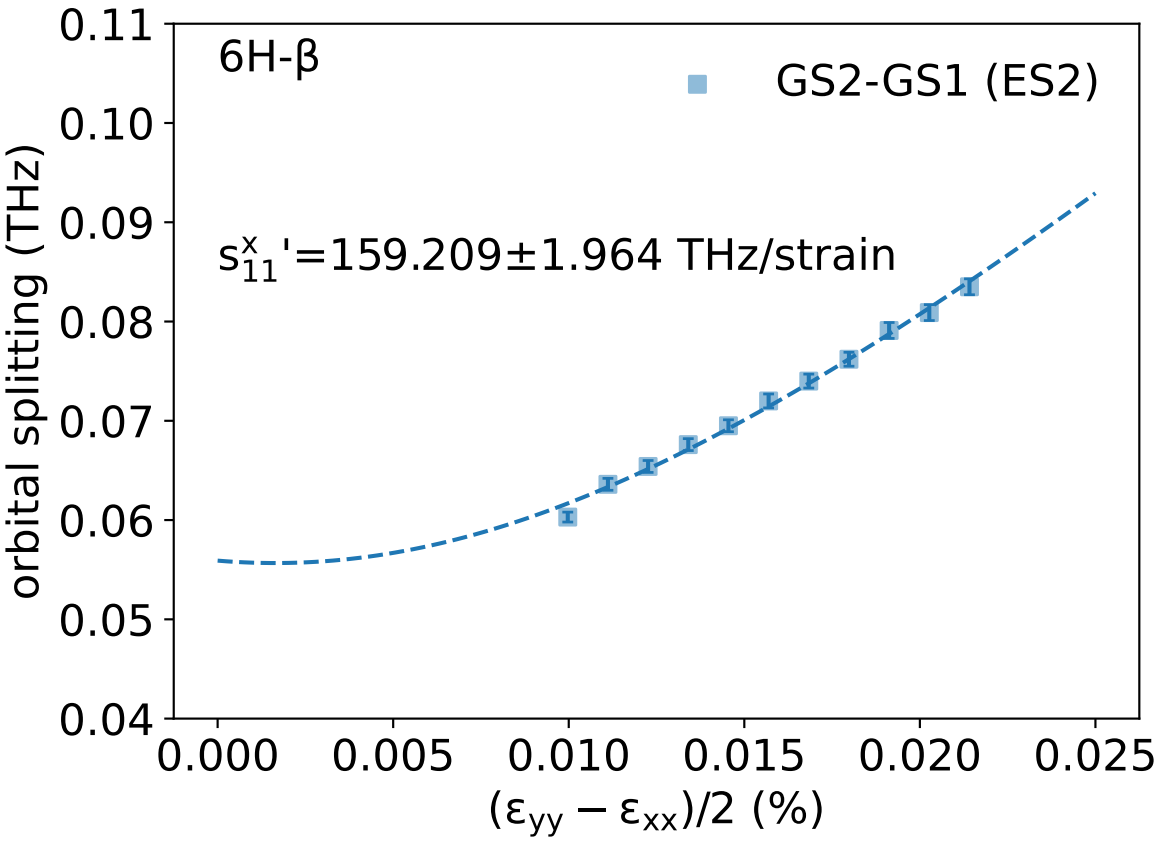

Figure 5.17: Fit of GS2-GS1 orbital splitting versus $\frac{\epsilon_{yy}-\epsilon_{xx}}{2}$ strain. The orbital splitting is calculated by taking the difference in energy between optical transitions to ES2. The ground state orbital doublet strain susceptibility $s_{11}^{x}{}' = 159.209 \pm 1.964$ THz/strain for the 6H-beta site.

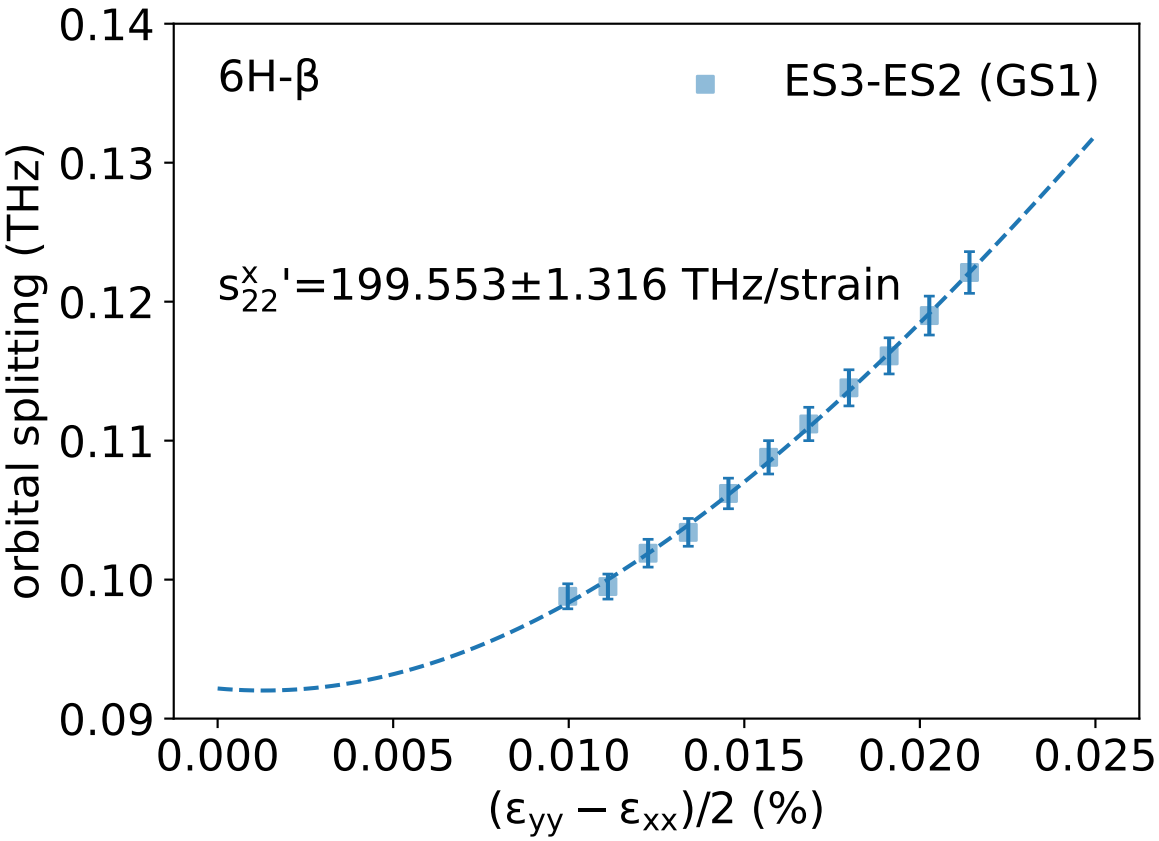

Figure 5.18: Fit of ES3-ES2 orbital splitting versus $\frac{\epsilon_{yy}-\epsilon_{xx}}{2}$ strain. The orbital splitting is calculated by taking the difference in energy between optical transitions from GS1. The excited state orbital doublet strain susceptibility $s_{22}^{x}{}' = 199.553 \pm 1.316$ THz/strain for the 6H-beta site.

retical model presented in [71] by plotting the square of the dipole moment, in accordance with Femi's Golden Rule. Fermi's Golden Rule states that the transition rate for a two level system will be proportional to the square of the dipole matrix element and the density states. In our fits, we fit the square of the dipole moment multiplied by an overall scale factor to account for the varying electric susceptibilities of each transition, the detection efficiency, and the conversion factor between the emission rate and detected voltage on our photodiode.

Electric dipole matrix elements different irreducible representations Γ_4 ground state and $\Gamma_{5/6}$, correspond to the following transitions 4H-α GS1-ES1 and GS2-ES2, 6H-α GS1-ES1 and GS2-ES2 and 6H-β GS1-ES3 and GS2-ES2. We fit these transitions to the square of the dipole moment, for polarization perpendicular to the c-axis, that is, an arbitrary combination of E_x and E_y electric fields, in accordance with our confocal measurement setup (we should have no E_z polarization). The functional form of the square of the dipole moment $|\langle e,\Gamma_{5,6}|H_{el}|g,\Gamma_4\rangle|^2 = |\langle e,\Gamma_4|H_{el}|g,\Gamma_{5,6}\rangle|^2$ and is given by:

$$\begin{aligned}|\langle e,\Gamma_{5,6}|H_{el}|g,\Gamma_4\rangle|^2 = \left(E^x_{ge}\right)^2 \times \Bigg[&\left(\sigma^2 E_x^2 + E_y^2\right)\cos^2\left(\frac{\theta_g}{2}\right)\cos^2\left(\frac{\theta_e}{2}\right) \\ &+ \Big[2\left(-\sigma^2 E_x^2 + E_y^2\right)\cos\left(\sigma\left(\psi_g+\psi_e\right)\right) - 4E_xE_y\sin\left(\sigma\left(\psi_g+\psi_e\right)\right)\Big] \\ &\times\cos\left(\frac{\theta_g}{2}\right)\cos\left(\frac{\theta_e}{2}\right)\sin\left(\frac{\theta_g}{2}\right)\sin\left(\frac{\theta_e}{2}\right) \\ &+ \left(\sigma^2 E_x^2 + E_y^2\right)\sin^2\left(\frac{\theta_g}{2}\right)\sin^2\left(\frac{\theta_e}{2}\right)\Bigg] \end{aligned} \tag{5.7}$$

Here $|e,\Gamma_{5,6}\rangle$ represents an excited state with $\Gamma_{5,6}$ irreducible representation, $|g,\Gamma_4\rangle$ represents a ground state with a Γ_4 irreducible representation. However, this equation also holds true for the case of where the ground state has a $\Gamma_{5,6}$ irreducible representation and the excited state has a Γ_4 irreducible representation. Furthermore, it does not matter whether the transition of interest originates from the excited state orbital singlet or doublet. E^x_{ge} represents the electric susceptibility for that transition, and σ represents the electric

pseudospin value $\{+1/2, -1/2\}$. While a fixed pseudospin value is not well defined for our ensemble measurements at 0 field, we set the pseudospin value used in the fit to $1/2$ as the dipole moment is functionally the same (provided it is the same in the ground and excited state). [71]. θ_g, θ_e, ψ_g, and ψ_e represent the strain mixing angles in the ground and excited state given by $\theta = \tan^{-1}\left(2\epsilon^x_{nn}\sqrt{1+\left(\epsilon^y_{nn}/\epsilon^x_{nn}\right)}/\lambda^z_{nn}\right)$ and $\psi = \tan^{-1}\left(\epsilon^y_{nn}/\epsilon^x_{nn}\right)$. E_x and E_y represent the strength of electric fields polarized along the x and y directions, where x is defined to be fixed to one of the bonds of the defect.

We also fit transitions between the same irreducible representations, these are the 4H-α GS1-ES2 and GS2-ES1, 6H-α GS1-ES2 and GS2-ES1,and 6H-β GS1-ES2, and GS2-ES3. Here, the functional form $|\langle e,\Gamma_4|H_{el}|g,\Gamma_4\rangle|^2 = |\langle e,\Gamma_{5,6}|H_{el}|g,\Gamma_{5,6}\rangle|^2$ and is given by:

$$\begin{aligned}|\langle e,\Gamma_4|H_{el}|g,\Gamma_4\rangle|^2 = \left(E^x_{ge}\right)^2 \times \Bigg[&\left(E_x^2-\sigma^2E_y^2\right)\cos^2\left(\frac{\theta_g}{2}\right)\cos^2\left(\frac{\theta_e}{2}\right)\\ &+\left[2\left(E_x^2-\sigma^2E_y^2\right)\cos\left(\sigma\left(\psi_g+\psi_e\right)\right)-4\sigma E_xE_y\sin\left(\sigma\left(\psi_g+\psi_e\right)\right)\right]\\ &\times\cos\left(\frac{\theta_g}{2}\right)\cos\left(\frac{\theta_e}{2}\right)\sin\left(\frac{\theta_g}{2}\right)\sin\left(\frac{\theta_e}{2}\right)\\ &+\left(E_x^2-\sigma^2E_y^2\right)\sin^2\left(\frac{\theta_g}{2}\right)\sin^2\left(\frac{\theta_e}{2}\right)\Bigg]\end{aligned} \tag{5.8}$$

Lastly, the optical dipole has a different mathematical dependence if it is a transition to the Γ_4 singlet excited state, as it is the case with the 4H- and 6H-β ES1. Furthermore, there is only a sinngle strain mixing angle in the ground state. The transition intensity for the β site GS1-ES1 has the functional dependence:

$$|\langle e,\Gamma_4|H_{el}|g,\Gamma_4\rangle|^2 = \left(E_{ge}^x\right)^2 \times \left[\left(E_x^2+E_y^2\right)\right.$$
$$\left.-2\left(E_y^2-E_x^2\right)\cos\left(\frac{\theta_g}{2}\right)\sin\left(\frac{\theta_g}{2}\right)\cos\left(\psi_g\right)\right] \tag{5.9}$$

For GS2-ES1 there is only a sign change:

$$|\langle e,\Gamma_4|H_{el}|g,\Gamma_4\rangle|^2 = \left(E_{ge}^x\right)^2 \times \left[\left(E_x^2+E_y^2\right)\right.$$
$$\left.+2\left(E_y^2-E_x^2\right)\cos\left(\frac{\theta_g}{2}\right)\sin\left(\frac{\theta_g}{2}\right)\cos\left(\psi_g\right)\right] \tag{5.10}$$

We note that for the 4H sites the ψ mixing angles are 0, due to estimating zero e_{nn}^y strain from our calibration. For the 4H-α,since the alignment of our sample is subject to small angular alignments, we fit the relative magnitudes of E_x and E_y. We find the best fit for the squared dipole matrix elements across all transitions for $E_y/E_x = 0.5$. The deviation of the GS1-ES1 and GS1-ES2 transitions from the model may originate from slight ellipticity of the beam used in optical excitation or the compounded effect of fit and calibration errors. Figure 5.20 shows the 4H-α fit extrapolated to 0.3 percent strain. At higher strain we expect to see the inversion of selection rules for transitions between the same and different irreducible representations.

For the 4H-β site, we observe that the brightness is only weakly dependent on strain. This may be due to inaccuracies in the fit of the double peak in the spectra. The fit is shown in figure 5.21.

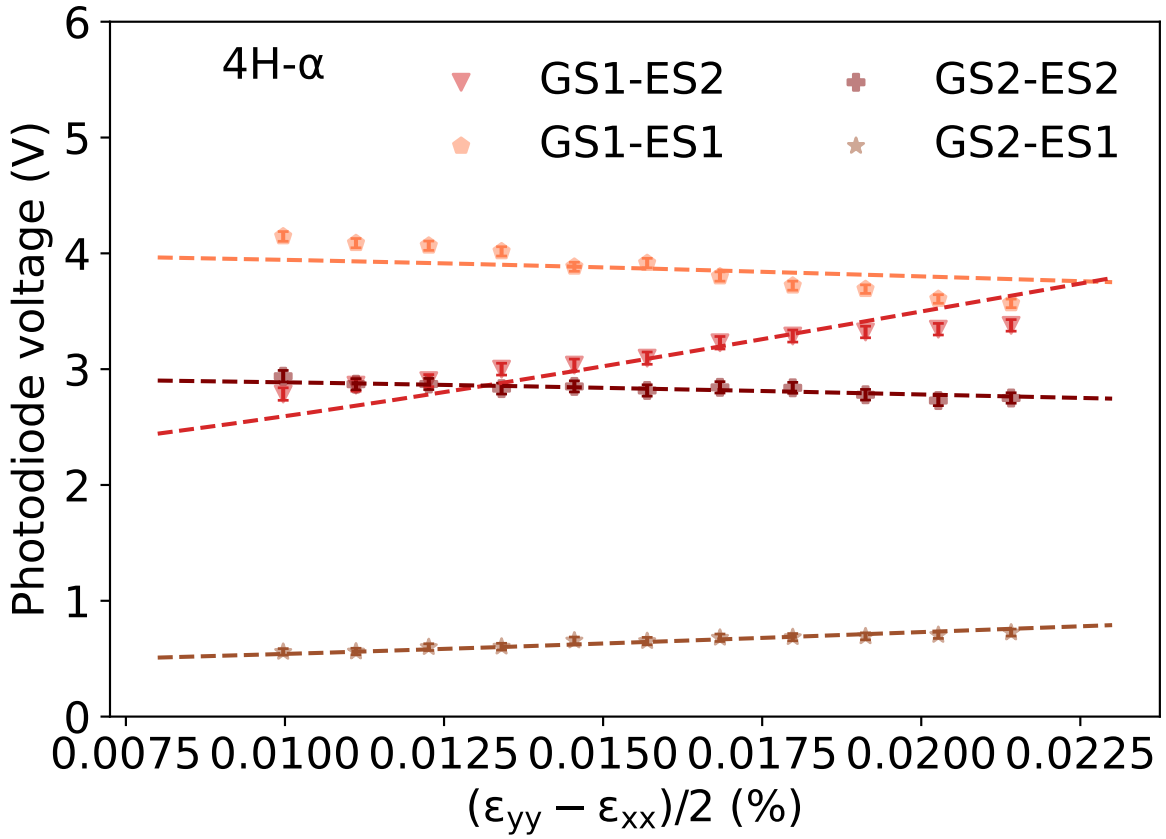

Figure 5.19: Photoluminescence intenstiy of 4H alpha optical transitions versus $\frac{\epsilon_{yy}-\epsilon_{xx}}{2}$ strain. The y-axis shows the measured voltage on a photodiode. The square of the transition dipole matrix element is fit for each site according to the irreducible representations of the ground state orbitals, with an overall scale factor.

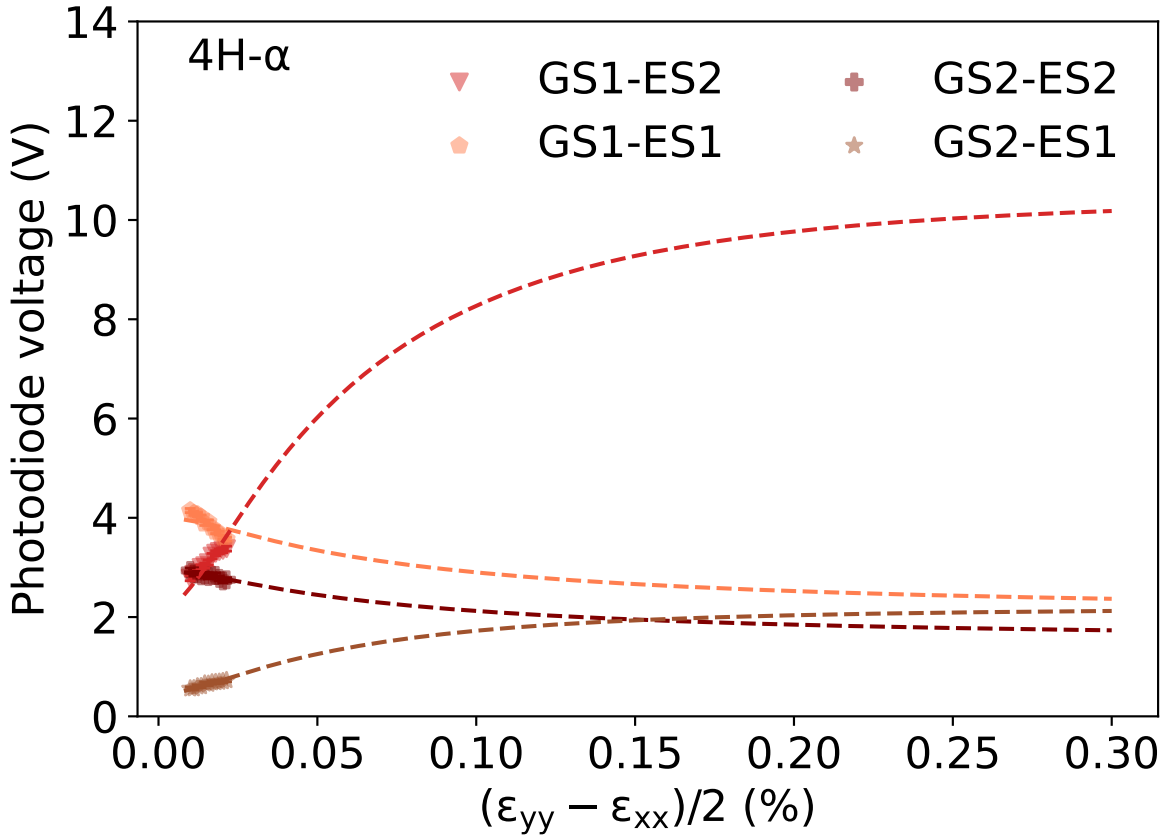

Figure 5.20: Photoluminescence intenstiy of 4H alpha optical transitions versus $\frac{\epsilon_{yy}-\epsilon_{xx}}{2}$ strain up to 0.3 percent. The y-axis shows the measured voltage on a photodiode. The square of the transition dipole matrix element is fit for each site according to the irreducible representations of the ground state orbitals, with an overall scale factor. At higher strains, the selection rules become inverted.

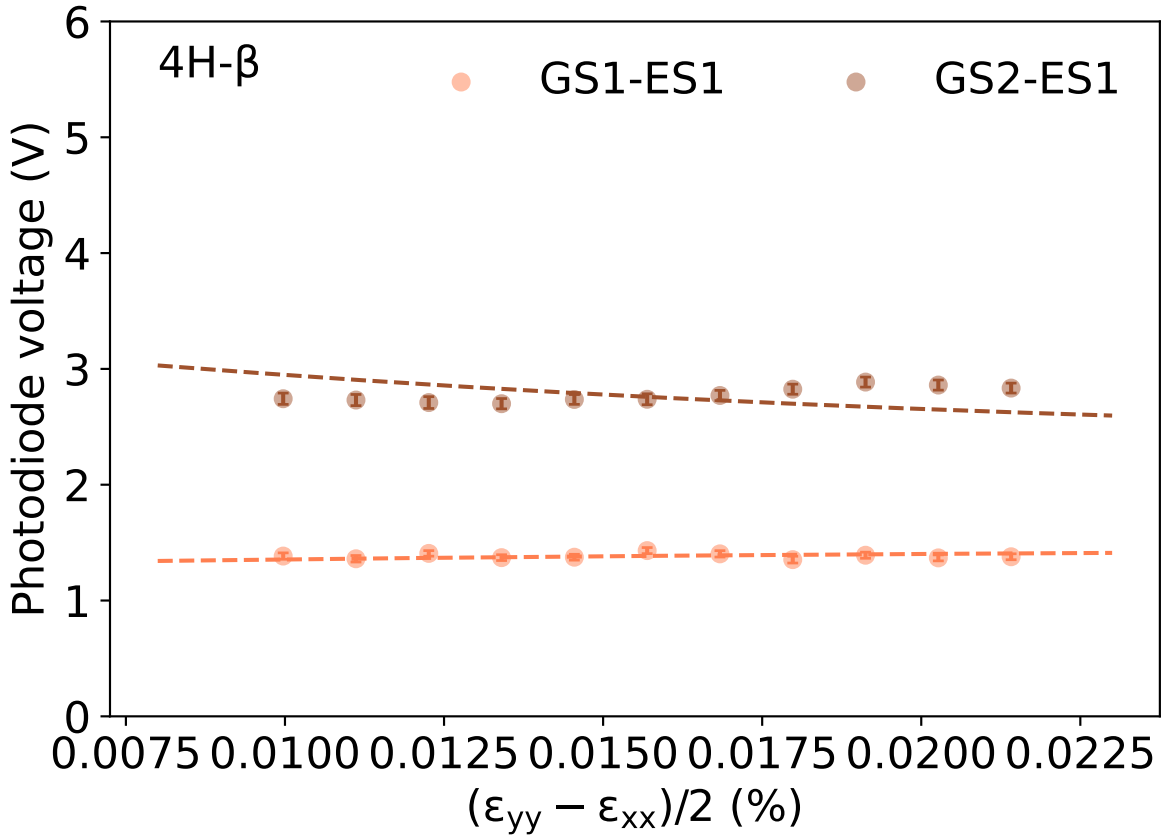

Figure 5.21: Photoluminescence intenstiy of 4H beta optical transitions versus $\frac{\epsilon_{yy}-\epsilon_{xx}}{2}$ strain. The y-axis shows the measured voltage on a photodiode. The square of the transition dipole matrix element is fit for each site according to the irreducible representations of the ground state orbitals, with an overall scale factor. At higher strains, the selection rules become inverted.

5.4 Estimating spin-strain susceptibilities

In this last section we estimate the spin-strain susceptibilities of SiC:V^{4+}. This is of particular interest, as the coherence of the spin states are often longer in these systems. Longer coherence of the spin state is promising for engineering coherent interactions between strain and a quantum two-level system.

We consider the case of an electron spin within an orbital sub level. The electron spin degeneracy is split by a magnetic field according to the Zeeman effect. According to perturbation theory, we expect the spin-strain coupling to be proportional to

$$\chi_{11}^{x\,\prime} \sim \frac{g\mu_B B}{\lambda_{nn}^{z}} \times s_{nn}^{x\,\prime} \tag{5.11}$$

Here μ_B is the Bohr magneton, B is the magnetic field amplitude, $\overset{z}{}_{nn}$ is the spin-orbit coupling for that particular orbital doublet, and $s_{nn}^{x\,\prime}$ is the orbital strain susceptibility parameter calculated in 5.3. Clearly, the spin-strain susceptibility will depend on the magnetic field provided $g\mu_B B << \lambda_{nn}^{z}$, and the spin-orbit coupling, the latter of which can vary significantly between sites. The computed spin-strain susceptibilities are shown in table 5.2.

Table 5.2: Strain susceptibilities and related parameters for the 4H and 6H silicon carbide α and β sites. Here the subscripts "11" and "22," label ground and excited state orbital doublets, respectively, such that for the 6H-β site the λ_{22}^z refers to the orbital splitting of the ES2 and ES3 states, and for the α sites λ_{22}^z refers to the splitting between ES1 and ES2. Spin-strain susceptibilities are calculated for a magnetic field of 250 mT. There is no ${s_{22}^x}'$ or λ_{22}^z value for the 4H-β site since the excited state orbital doublet lies above the conduction band. Values for λ_{nn}^z and g_{zz} are from [77], and are consistent with the orbital splittings measured in this experiment.

	4H-α	4H-β	6H-α	6H-β
${s_{11}^x}'$ (THz/strain)	237.863 ± 2.434	280.334 ± 2.511	157.401 ± 33.247	159.209 ± 1.964
${s_{22}^x}'$ (THz/strain)	-451.742 ± 0.888	-	248.753 ± 1.5	199.553 ± 1.316
λ_{11}^z (GHz)	529 ± 1	43 ± 1	524 ± 1	25 ± 1
λ_{22}^z (GHz)	181 ± 1	-	167 ± 1	72 ± 1
$g_{zz}^{(GS1)}$	1.748	1.870 ± 0.005	1.749	1.95
$g_{zz}^{(GS2)}$	-	2.035 ± 0.005	-	2.00 ± 0.02
$g_{zz}^{(ES1)}$	2.24	2.03 ± 0.02	2.24	2.0 ± 0.1
${\chi_{11}^{x,(GS1)}}'$ (THz/strain)	2.750 ± 0.029	42.657 ± 1.066	1.838 ± 0.388	43.4516 ± 1.819
${\chi_{11}^{x,(GS2)}}'$ (THz/strain)	-	46.421 ± 1.159	-	55.859 ± 2.332
${\chi_{22}^{x,(ES1)}}'$ (THz/strain)	-19.562 ± 0.115	-	11.675 ± 0.099	-

CHAPTER 6

ELECTRONIC STRUCTURE OF THE DIVACANCY DEFECT IN SIC

The divacancy defect in silicon carbide consists of a missing silicon atom located next to a missing carbon atom. There are 4 possible sites for the divacancy in 4H SiC, 6 possible sites for the divacancy in 6H, and only one possible site for 3C.

The individual silicon and carbon vacancies consituting the divacancy are labeled by local symmetry, whether that lattice site has a *quasi-cubic (k)* or *quasi-hexagonal (h)* symmetry. Divacancies are labeled by the symmetries for individual sites, with the carbon atom conventionally labeled first. So for 4H-SiC, the possible divacancies are *hh*, *kk*, *hk*, and *kh*.

In the silicon carbide lattice there are *c-axis* and *basal* divacancies. The layer stacking and bond angles of the SiC lattice are such that the c-axis divacancies are oriented along the c-axis, and the basal divacancies are oriented within a bilayer. In 4H-SiC c-axis divacancies have C_{3v} symmetry and the basal divacancies have C_{1h} symmetry.

6.1 Spin triplet ground state

The $VV0$ contains 6 dangling bonds that form two orbital singlets and two orbital doublet states. Each dangling bond contributes 1 electron to the system. The two orbital singlet states are lower in energy than the doublet states (which are degenerate in energy), causing 4 electrons to pair in the singlet levels and leaving the remaining two electrons unpaired in the two lowest energy orbital doublet states.

The remaining two electrons form a spin-1 system. Therefore the combined spin states of these electrons are either one of the spin triplet states:

$$|\uparrow\uparrow\rangle, m_s = 1 \tag{6.1}$$

$$|\downarrow\downarrow\rangle, m_s = -1 \tag{6.2}$$

$$\frac{|\uparrow\downarrow\rangle + |\downarrow\uparrow\rangle}{2}, m_s = 0 \tag{6.3}$$

with total spin $S = 1$. Here m_s labels the spin quantum number projection. The system can also exist in a spin singlet state $\left(\frac{|\uparrow\downarrow\rangle - |\downarrow\uparrow\rangle}{2}\right)$ with total spin $S = 0$ and $m_s = 0$.

The combined orbital and spin ground state wavefunction must be antisymmetric under exchange, resulting in a orbital singlet state (antisymmetric linear combination of the two lowest energy degenerate doublet states), and a spin triplet (symmetric linear combination of the spin state). This wavefunction is labeled $^3A_2$.

The Hamiltonian describing this S=1 system is:

$$H = S \cdot D \cdot S + \gamma_e B \cdot S + \sum_j S \cdot A_j \cdot I_j. \tag{6.4}$$

Here D is the zero-field splitting tensor, γ_e is the electron's gyromagnetic ratio ($g\mu_B$), S is the electron spin operator, B is the magnetic field vector, and A_j and I_j are the jth hyperfine tensor and nuclear spin operator, where j enumerates potentially many nuclear spins. For $VV0$, D describes a zero field splitting between the $m_s = 0$ and $m_s = \pm 1$ triplet spin states, while the $m_s = 1$ and $m_s = -1$ states are energetically degenerate. A_j includes both dipole-dipole coupling and Fermi contact interaction terms.

6.2 Off-resonant optical excitation

The optical spectra of the divacancy under off-resonant excitation is well known. Generally the divacancy emits optically in the near-IR between 1000nm and 1100nm. However the different defect sites within each polytype have slightly different optical and spin transition

energies, linewidths, brightness, and coherence. The optical transitions are labeled $PL1 - PL4$ in order of increasing energy, and previous work has identified the corresponding lattice sites.

The $VV0$ e states can also form other spin and orbital combinations denoted by ^1E and $^1A_1$. These two states form a spin singlet manifold, and lying energetically between the ground and excited spin triplet states. These states make up the *intersystem crossing*. The excited triplet states couple with different rates to this spin singlet manifold.

There are two consequences of spin-dependent coupling to the intersystem crossing. The first is optical initialization. If the defect is illuminated for sufficiently long under off-resonant light, the spins will eventually polarize into the $m_s = 0$ ground spin sublevel. Under optical illumination, relaxation occurs through a combination of radiative processes, and non-radiative transitions through the intersystem crossing. Therefore, the second result of spin-dependent coupling to the intersystem crossing is that the fluorescence intensity of the defect is dependent on it's initial spin state [22].

In an off-resonant excitation scheme, the excitation wavelength corresponds to a higher energy than the defect's zero phonon line, while long pass optical filtering separates the zero phonon line from the laser excitation and allows for collection of the entire zero phonon line and phonon sideband. ODMR could be performed by also adding a microwave drive to resonantly reshuffle the spin state populations. The population change from microwave driving will be reflected as a change in fluorescence, due to the spin dependent transition rates through the intersystem crossing.

The resultant ODMR spectra and contrast will depend on specifics of the defect including it's site within the lattice, and the polytype of silicon carbide. Existing literature shows that for divacancy ensembles, the ODMR contrast is on the order of a few percent or less.

CHAPTER 7

SPALLED 4H-SIC FILMS AS A QUBIT HOST MATERIAL

7.1 Introduction

Spalling uses controlled crack formation and propagation to deterministically fracture thin films from the surface of a wafer [8, 14]. 4H silicon carbide is an important substrate in the power electronics industry[61, 54]. 4H-SiC is also a leading wafer scale candidate for solid-state quantum coherent devices in quantum communications and sensing [77, 13]. However, spalling has yet to be demonstrated in 4H-SiC due to it's high fracture toughness.

The discussion in this section is adapted from reference [34]. Our efforts to spall silicon carbide marked the hardest material spalled to date [9]. The previous hardest spalled material was gallium nitride, which was 2.5 times less hard than silicon carbide. This innovation was possible through optimization of the stressor layer and crack initiation method. Tens of microns thick films of silicon carbide were successfully spalled from bulk wafers and transferred to other surfaces and substrates. We then benchmarked the coherence of neutral divacancy ($VV0$) qubit ensembles in the spalled films again bulk reference ships, and showed T_2^* and T_2 values the same order of magnitude as the bulk.

7.2 Spalling process

The first step of the spalling process is deposition of a thick metal stressor layer on top of the surface to be spalled [35]. This layer creates stress in the substrate just below the surface. Higher fracture toughness materials require thicker films to support spalling. The thickness required can be estimated using a theoretical model from Suo and Hutchinson [66]. Details of Suo and Hutchinson's model have also been described in Ref. [9].

In order for successful spalling to occur, an additional condition with regards to the critical strain energy release rate (G_c) must be satisfied [36]. The energy released during

spalling must be greater than the energy required for the bonds during the process. The definition of G_C is:

$$G_C = \frac{K_{IC}^2}{E(1-\nu^2)}, \tag{7.1}$$

where K_{IC} is the fracture toughness, E is Young's modulus, and ν is Poisson's ratio. Figure 7.1 shows the energy required to spall SiC compared to other materials that have previously been spalled.

7.3 Thickness of metal film and spalling crack nucleation

One key tuning knob in the spalling process is the thickness of the metal stressor layer. In particular the thickness of the spalled film must vary less than 10 percent across the sample, otherwise the spalling process becomes unpredictable. A uniform thickness is important as the conditions for crack initiation and propagation are independent of one another [78]. The stressor layer is a tens of microns thick electroplated nickel layer deposited on top of a Cr/Ti or Au/Ti seed layer. Electroplated nickel [67, 9, 46, 17] is ideal for spalling due to its high deposition rate and capability to tune the film stress [59]. While sputtering can be used to deposit very uniform films of nickel, the process takes prohibitively long and cannot generate films with sufficiently high stress.

Thickness nonuniformity issues can be dealt with by incorporating an auxiliary electrode, known as a thief, into the electroplating setup [60]. The thief has a window matching the substrate size and controls the current distribution around the edge of the substrate. In the electroplating setu, the substrate forms the cathode, and the thief is shorted to the substrate. The samples electroplated were 29 mm x 29 mm. Comsol modeling was used to optimize the thief design. The thief design was was used to optimize the nickel thickness at the center of the substrate and along the edges.

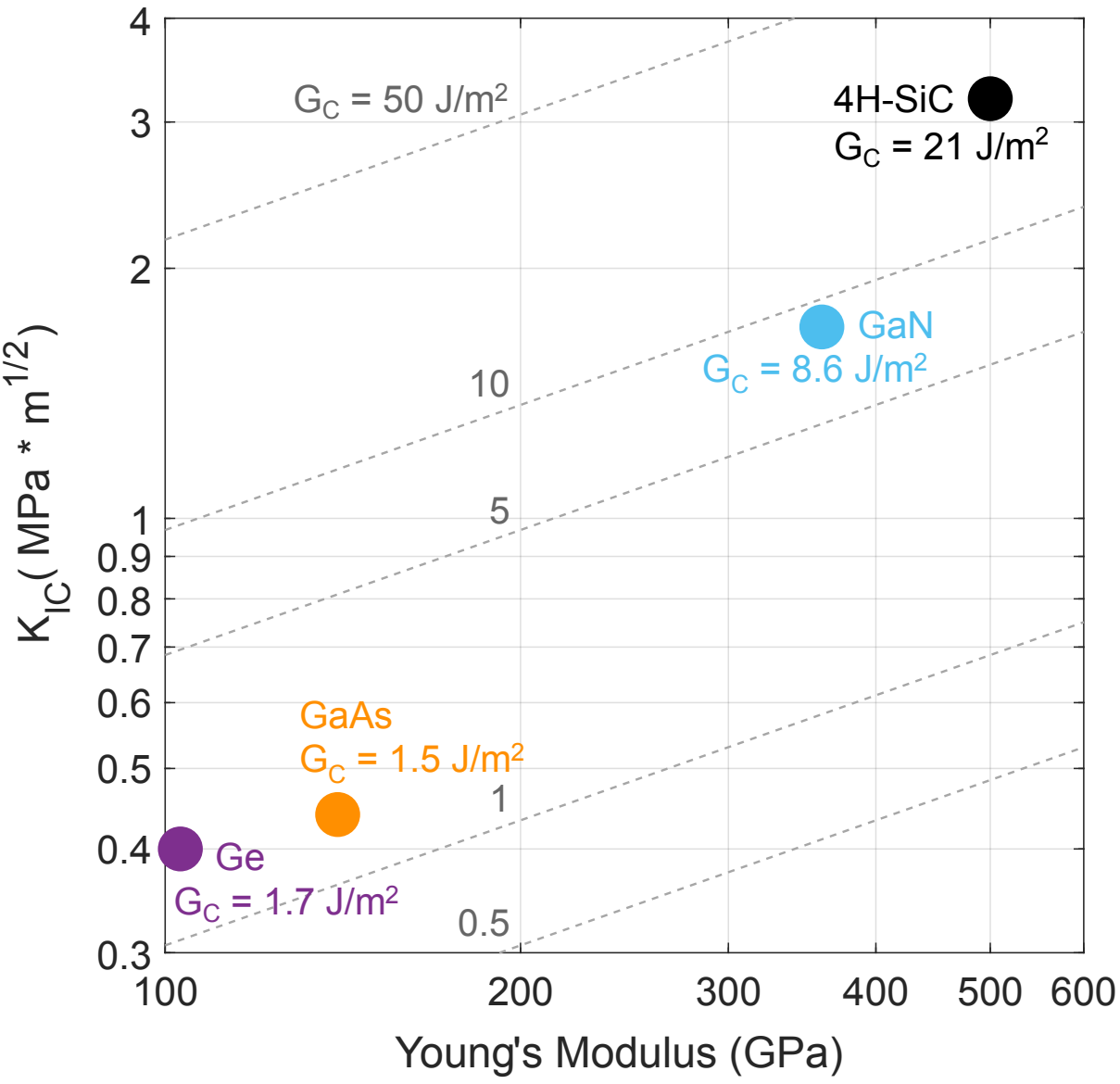

Figure 7.1: Reproduced from [34]. Plot of Young's modulus and fracture toughness for SiC compared to previously spalled materials.

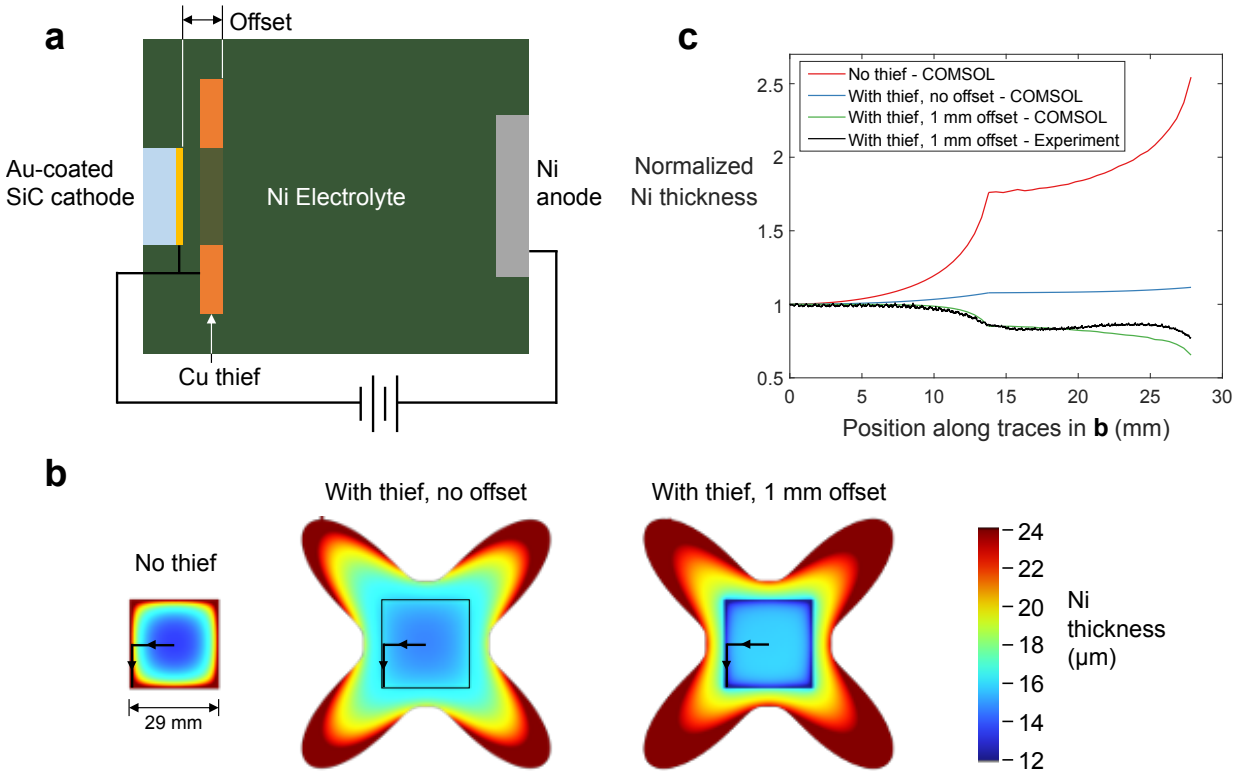

Figure 7.2: Figure reproduced from [3]. Schematic of the electroplating geometry and nickel thickness for different thief distances from cathode.

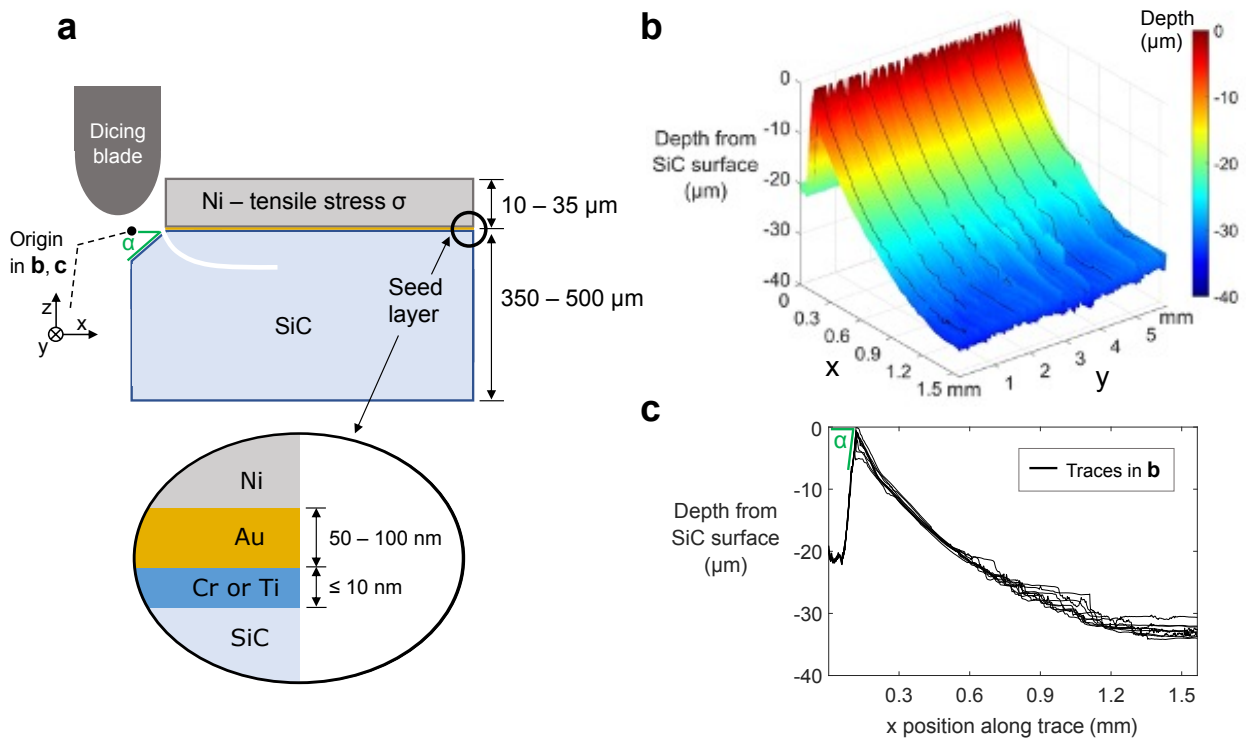

Figure 7.3: Figure reproduced from [34]. a Diagram showing the trench carved by a dicing saw. b 3D laser scanning confocal microscope map taken at the crack edge after spalling. c Black line traces in b.

It is also necessary to reliably be able to generate a crack in the substrate for the spalling process. Typically the crack is initiated by termination of the stressor layer away from the substrate edge [8, 9]. However, during initial attempts at the spalling process the film delaminated at the Au/Ni interface.

Delamination was avoided by using a dicing saw to create a trench at the edge of the nickel stressor layer. The dicing was performed after deposition of the Cr/Au or Ti/Au layer but before deposition of the nickel. Because of the elliptical shape of the dicing saw blade, it was possible to optimize the trench sidewall angles by varying the depth of the cut.

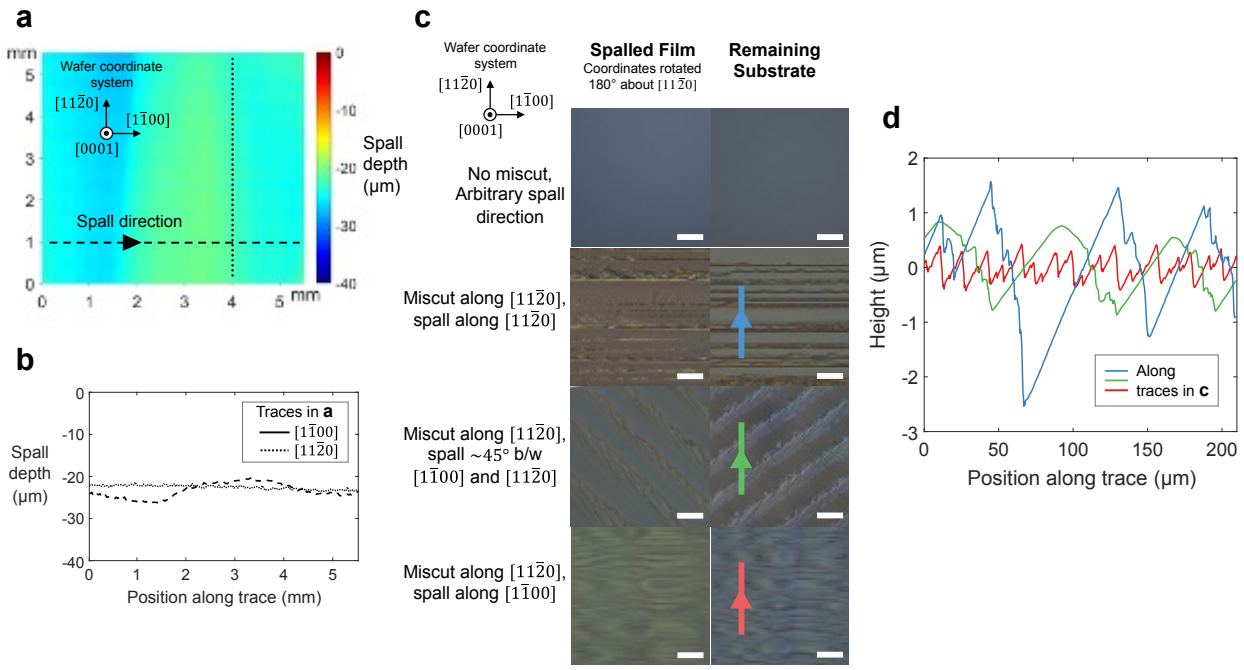

Figure 7.4: 3D laser scanning confocal microscopy of the substrates after the spalling process. Figure is reproduced from [34].

7.4 Characterization of films and substrate re-use

In these experiments, square dies were spalled, however, it is expected that the developed process could generalize to full wafers. 3D laser scanning microscopy was used to characterize the surface of the substrate left behind after spall, which is expected to mirror the surface morphology of the spalled film. A 5.5 mm x 5.5 mm area near the center of the of the substrate is shown in Figure 7.4.

The performance of spalling for different SiC substrates was compared between on-axis and off-axis grown substrates, for different spall directions. The on axis samples were shown to spall such that the remaining surface is smooth down to 10s of microns across the milimeter scale (Figure 7.4c). On the other hand, the miscut samples showed a corrugated pattern after spalling. The amount of roughness was reduced, but not entirely eliminated by spalling perpendicular to the miscut direction. Ionic semiconductors such as gallium arsenide and indium phosphide are known to spall along crystal planes [8, 14, 67, 55].

The spalling technique also allows for generation of multiple films through substrate reuse. Lapping and mechanical polishing was used to smooth the substrate following spalling. The mechanical polishing process consumed 10-20 microns of the substrate. Then, the spalling process was repeated on the polished substrate. The films generated from the spalling process generally have a thickness of 10 to 50 microns (see Figure 7.5).

7.5 Measurement of qubit properties in spalled films

Spalled silicon carbide is a promising host material for optically active spin defects in quantum science applications. Since the spalled films are directly fractured from the bulk wafer, they are also expected to host defects such as the vanadium ion [77], NV center [38], and divacancy [43] with favorable quantum properties.

The divacancy defect [24, 22] was used to benchmark the coherence of a spin defect system between the spalled films and bulk silicon carbide. A comparison of the continuous-wave optically detected magnetic resonance (ODMR) spectra between the bulk sample and spalled film are shown in Figure 7.6a. All experiments are performed in the absence of an applied external magnetic field. The resonance for the PL4 divacancies occurs at 1.353 GHz. Photoluminescence of all divacancy sites is shown in Figure 7.7. Measurements of the spin coherence times were then compared between the bulk wafer and spalled film. Rabi oscillations are driven at the PL4 resonance by sweeping the duration of a microwave pulse and detecting the change in fluorescence at the end of the pulse. The result is shown in Figure 7.6b. Furthermore, a Ramsey experiment was used to measure T_2^* as shown in Figure 7.6c. A $T_2^* = 1.31 \pm 0.03$ μs was measured in bulk and a $T_2^* = 1.02 \pm 0.03$ μs was measured in the film. Likewise Hahn-echo measurements found a slightly shorter $T_2 = 79.7 \pm 12.2$ s in the film compared to $T_2 = 117.4 \pm 41.8$ s in the bulk sample. The lower T_2^* and T_2 may be due to residual broadening of the ensemble film resonances. The residual broadening may be caused by dislocations or unresolved elastic strain within the film [25][23]. And additional

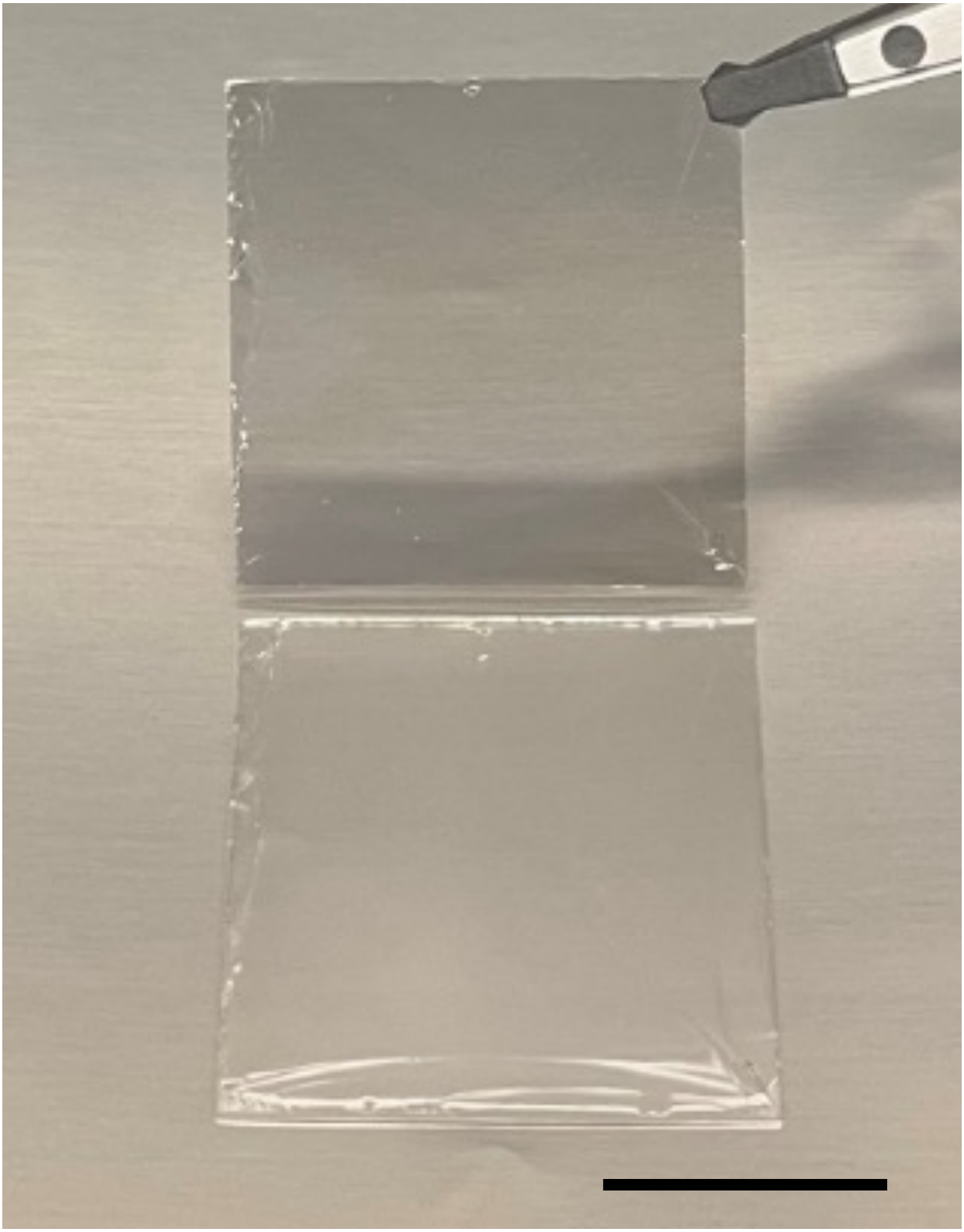

Figure 7.5: Figure is reproduced from reference [34]. The 30 m thick spalled film is held with a tweezer above the corresponding substrate which it originated from.

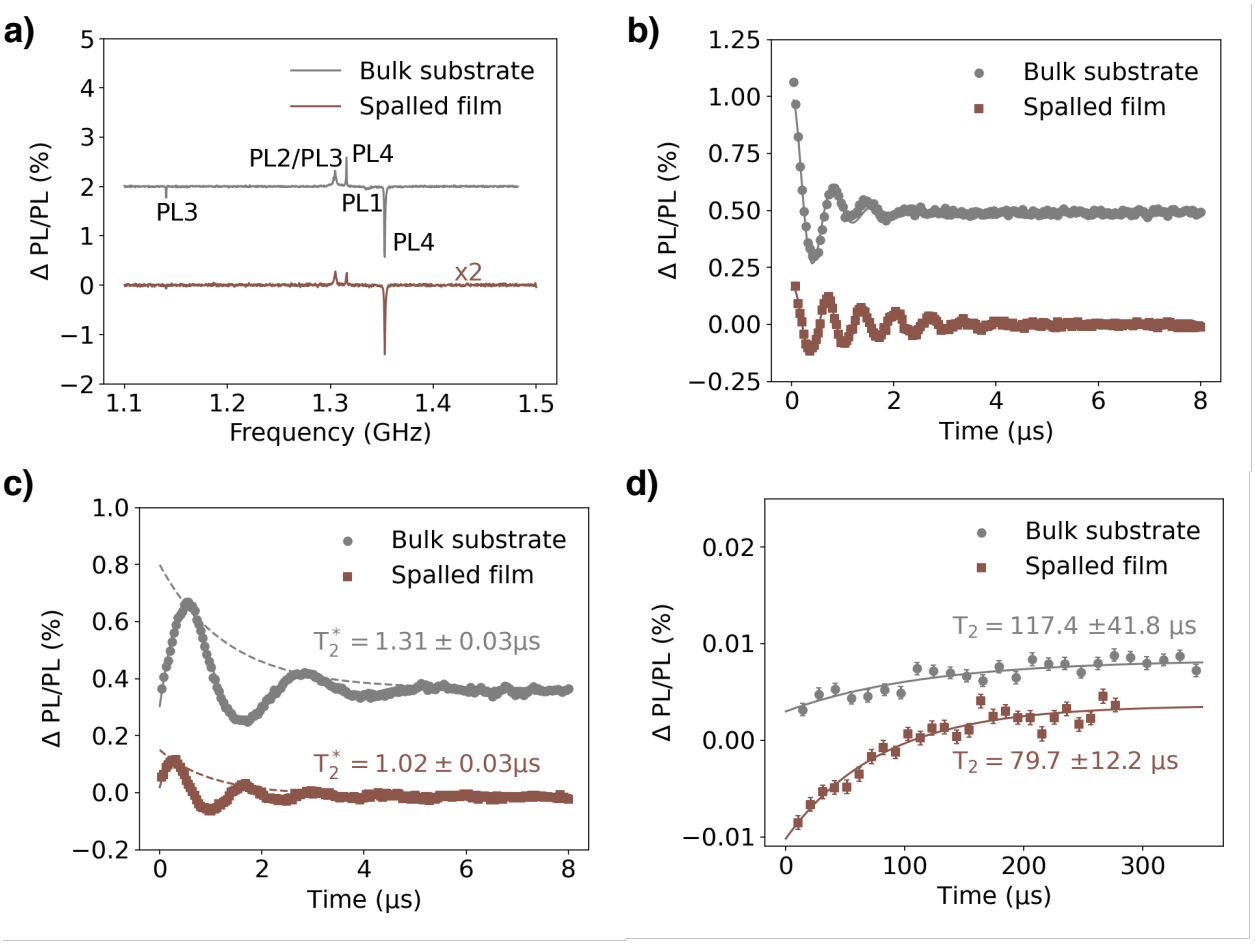

Figure 7.6: A comparison of CW ODMR spectra, Rabi oscillations, Ramsey decay envelopes, and Hahn echo recovery. Figure is reproduced from [3].

strain may have been induced in the film during transfer and mounting to a PCB for ODMR experiments.

Figure 7.8, shows the two different microwave driving modalities used in these experiments. Initial experiments used a draped wirebond with the goal of obtaining identical magnetic field profiles near the surface of the bulk wafer and spalled film (due to the two samples having a factor of 10 difference in thickness). However, it was difficult to repeatedly bond the wire close enough to the sample, and align the laser spot systematically for different samples and different bonds. This complicated measurement due to the fact that the magnetic field around the wire also falls off $\sim 1/r$. The final data was instead taken using

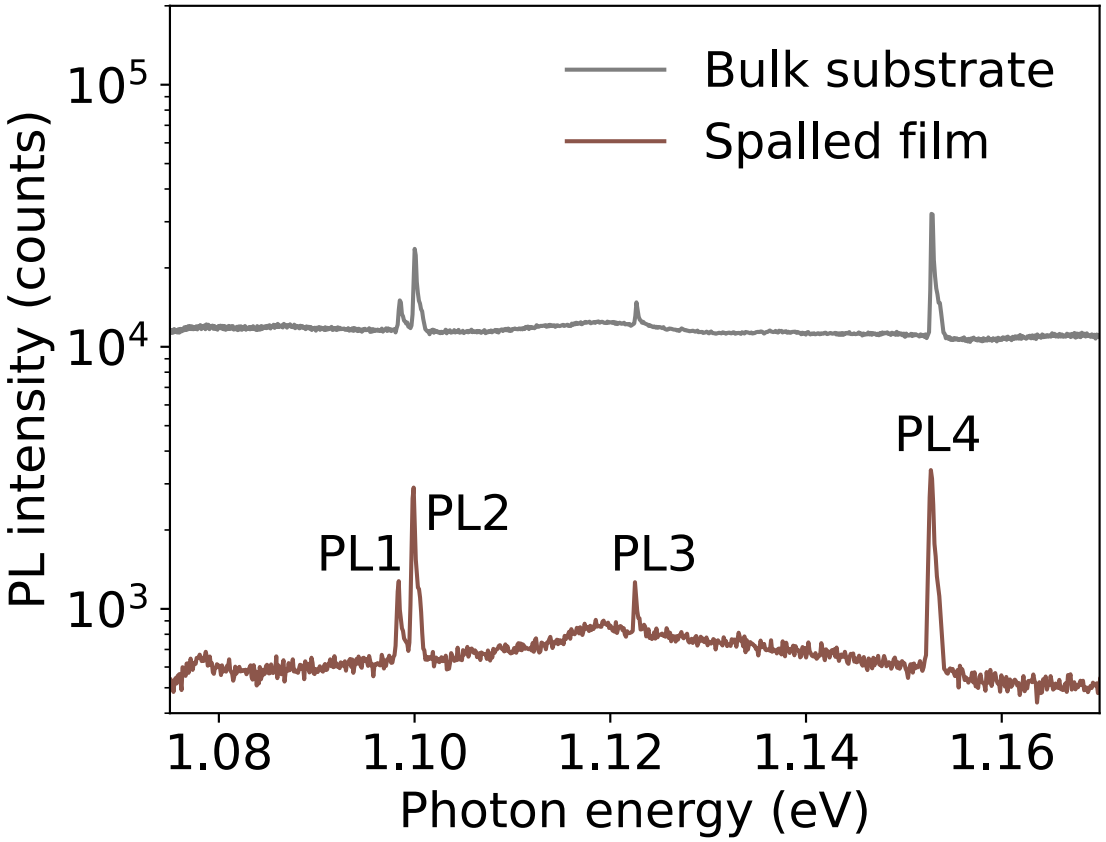

Figure 7.7: Comparison of PL spectra between the bulk substrate and a spalled film. Figure is reproduced from [3].

a coplanar waveguide on a PCB to generate a magnetic field concentrated at the backside of each sample. The PCB has a more uniform magnetic field between the ground plane and signal lines of the PCB. With the PCB alignment is repeatable across different samples, however, we do observe ensemble effects due to the different thicknesses of the samples, as the volume probed by the laser should be concentrated near the surface. For the spalled film the magnetic field is expected to be relatively uniform as a function of depth in the thin film. Divacancies in the bulk sample are expected to experience a range of different driving strengths depending on their distance from the PCB. This is one possible explanation for the rapid damping of the ensemble Rabi, and lower contrast of the ensemble Hahn echo recovery signal (as compared to the spalled film).

In these experiments, the lockin method was used to measure low contrast divacancy optically detected magnetic resonance signals on a noisy photodiode. Figure 7.9 shows the operational principle behind a lockin amplifier. In the time-domain a signal can be difficult to observe in the prescence of wideband frequency noise. In the lockin method, a measured experimental variable is temporally modulated by modulating an input parameter. The modulated output signal is mixed with a reference signal oscillating at the same frequency as the signal of interest. The signal being measured shifts to baseband, sufficiently far from noise signals (that are periodic at other frequencies). The remaining noise can be filtered out with a sufficiently narrow low pass filter, with the amplitude of the original signal mapped to the output of the lockin amplifier.

Figure 7.10 shows how the lockin method could be implemented to measure continuous wave optically detected magnetic resonance for the divacancy ensembles. Here a signal generator supplies an RF signal to drive the divacancy's spin. The microwave driving field is modulated on/off at a frequency of 500 Hz. The resulting modulation drives oscillation of the divacancy's spin population at the same frequency, which is detectable on a photodiode.

Figure 7.11 shows idealized time-domain input and output signals in a CW ODMR mea-

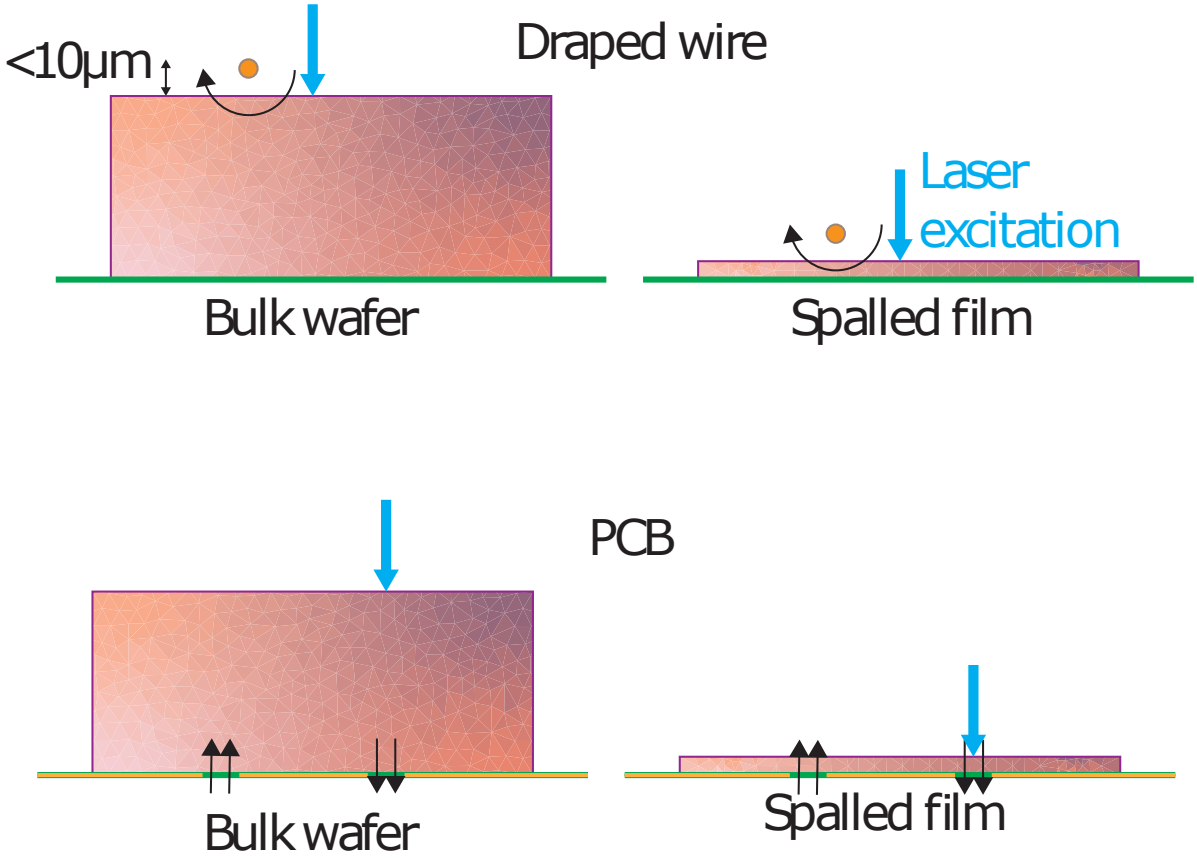

Figure 7.8: Schematic comparing the magnetic field spin driving between the the use of a stripline PCB and draped wirebond. Black arrows indicate the magnetic field direction.

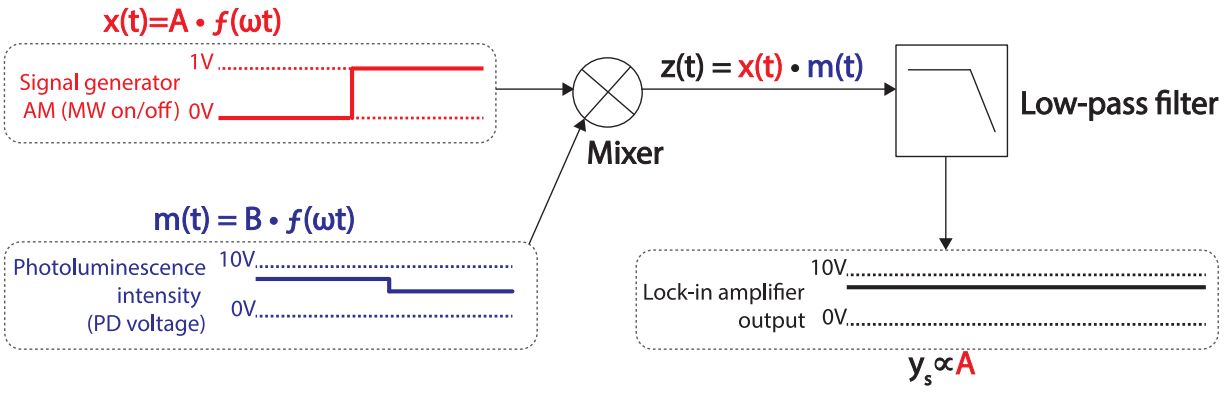

Figure 7.9: Operational principle behind a lockin amplifier.

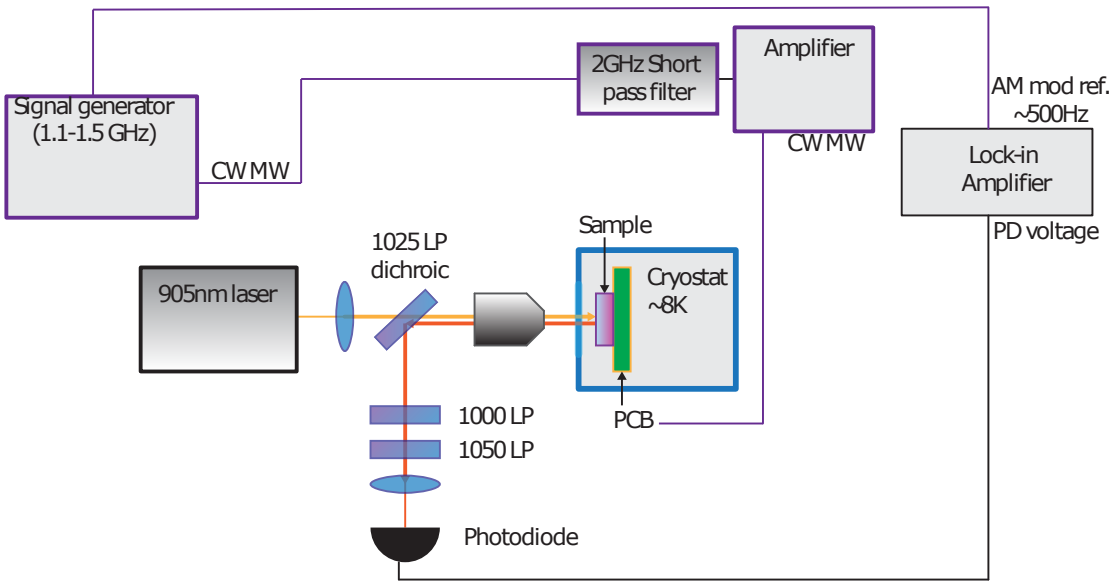

Figure 7.10: CW ODMR setup used to measure divacancy ensembles in Section 7.

surement of divacancy ensembles. The laser is on continuously while the microwave driving field is periodically modulated, leading to periodic changes in the ground state spin projection. Since the divacancy fluorescence is spin dependent, the detected fluorescence at the photodiode also oscillates with the same frequency. A complete CW ODMR spectrum can be obtained by measuring this percent change in detected intensity as a function of a frequency of the microwave driving field. Tuning the frequency will tune the microwave drive into resonance with different defects and transitions.

Figure 7.12 shows the pulsed optically detected magnetic resonance setup used to perform coherent control experiments on divacancy ensembles in this section. Pulses generated by an arbitrary waveform generator are either sent to an AOM to pulse the laser, or to an RF switch to pulse the microwave drive. These pulses are applied on top of the existing modulation provided by the signal generator for the lockin method. In general the modulation of the signal generator will occur slowly $\sim$ 500 Hz due to the limited bandwidth of the high gain photodiode, whereas the duration sequences, used for Rabi, and Ramsey experiments is less

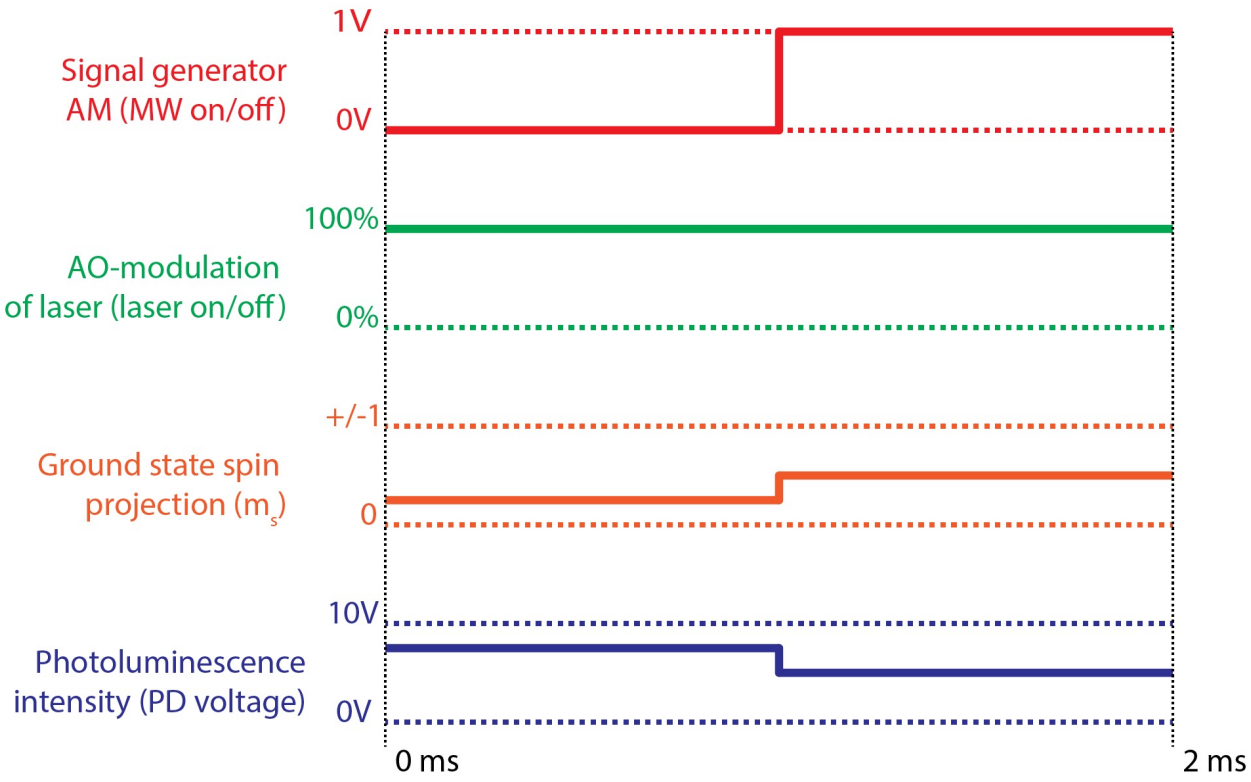

Figure 7.11: Idealized time-domain input and output signals in a CW ODMR measurement of divacancy ensembles.

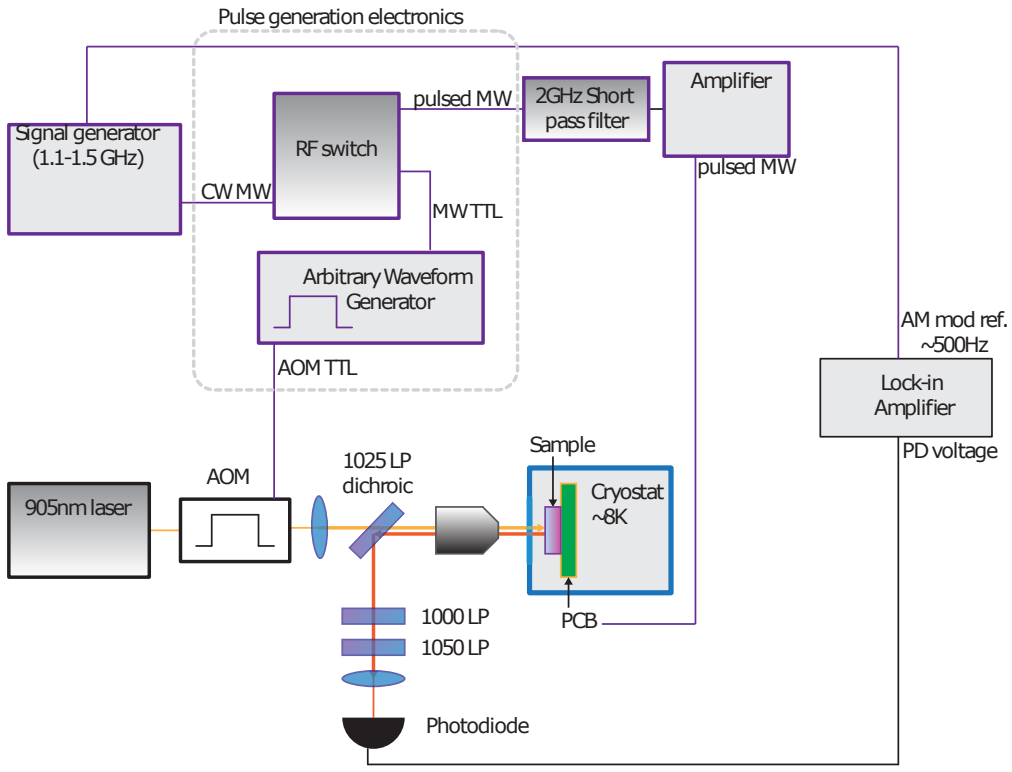

Figure 7.12: Pulsed ODMR setup used to perform Rabi, Ramsey (T_2^*), and Hahn-echo (T_2) experiments on divacancy ensembles.

than 20 μs. The pulsed microwave drive is sent through a 2 GHz short pass filter and then to a 40dB amplifier. The amplified RF signal is sent to the cryostat through coaxial feedthroughs to create a driving magnetic field on the PCB.

CHAPTER 8

OUTLOOK

Our studies of the temperature dependent lifetime of V^{4+} in SiC showed that this defect could satisfy several requirements for a spin photon interface: optical spin polarization and readout, and long spin T_1 times. There is also potential to engineer the relaxation rates at elevated temperatures by using strain to modulate the Orbach relaxation process. We also demonstrated strain tuning of the V^{4+} optical transitions and experimental characterization of the strain-orbital coupling parameters.

This will be one step towards practical deployment of V^{4+} for quantum technologies. Future studies of V^{4+} should focus on coherent control of the electron spin, interfacing single defects, and initialization and control of individual nuclear states [70, 2], which could potentially be used as a quantum register [65, 56, 30, 50]. The measured strain-orbital coupling parameters will allow us to design a setup to apply sufficiently high strain (0.1 percent) to enable operation of the V^{4+} defect at elevated temperatures. One possibility to apply higher strain could be through use of a diamond anvil cell. The strain orbital coupling can be used to compute the spin strain coupling parameters. We have the basic parameters to explore interesting acoustic driving experiments for both the optical and spin transitions [74]. Exploration of V^{4+} in electronic devices [4] is particularly interesting given the incomplete understanding of the V^{4+} ionization processes in 4H silicon carbide.

Spalling of 4H silicon carbide was demonstrated and near-bulk like coherence was measured for divacancy defects in the films. Spalling of such a hard fracture toughness material was enabled by several optimizations to the spalling process. Similar T_2^* and T_2, ~ 78 percent and ~ 68 percent respectively, were measured as compared to the bulk value.

The capability to transfer films and defect ensembles from the bulk motivates the integration the spalled silicon carbide films with other substrates, such as on-chip silicon photonics. This approach could also be used to transfer individual defects that are precharacterized in

the bulk, as this method is low cost and does not damage the substrate surface, which would be ideal when trying to transfer dilute defect ensembles prepared by ion implanation near the silicon carbide surface. This could be used to examine the spin strain interaction in single defects. Probing the spin-strain interaction directly is currently prohibited by the prescence of inhomogeneous broadening in our ensembles, making it impossible to resolve the electron spin states, with magnetic fields $<$400 G. The readily available silicon carbide membranes are promising for further exploration of experiments studying the strain interaction with defects such as vanadium. Furthermore, this work shows that the ODMR characterization methods provide a sensitive probe the host crystal strain, which could be deployed to understand the local strain environment affecting the V^{4+} ion in silicon carbide.

BIBLIOGRAPHY

[1] Anatole Abragam and Brebis Bleaney. *Electron paramagnetic resonance of transition ions*. Clarendon P., 1970.

[2] C Adambukulam et al. "Hyperfine Spectroscopy and Fast, All-Optical Arbitrary State Initialization and Readout of a Single, Ten-Level Ge 73 Vacancy Nuclear Spin Qudit in Diamond". In: *Physical Review Letters* 132.6 (2024), p. 060603.

[3] Jonghoon Ahn et al. "Extended spin relaxation times of optically addressed vanadium defects in silicon carbide at telecommunication frequencies". In: *Phys. Rev. Appl.* 22 (4 Oct. 2024), p. 044078. DOI: 10.1103/PhysRevApplied.22.044078. URL: https://link.aps.org/doi/10.1103/PhysRevApplied.22.044078.

[4] Christopher P Anderson et al. "Electrical and optical control of single spins integrated in scalable semiconductor devices". In: *Science* 366.6470 (2019), pp. 1225–1230.

[5] Thomas Astner et al. "Vanadium in silicon carbide: Telecom-ready spin centres with long relaxation lifetimes and hyperfine-resolved optical transitions". In: *Quantum Science and Technology* 9.3 (2024), p. 035038.

[6] J Baur, M Kunzer, and J Schneider. "Transition metals in SiC polytypes, as studied by magnetic resonance techniques". In: *physica status solidi (a)* 162.1 (1997), pp. 153–172.

[7] SL Bayliss et al. "Optically addressable molecular spins for quantum information processing". In: *Science* 370.6522 (2020), pp. 1309–1312.

[8] Stephen W. Bedell et al. "Kerf-Less Removal of Si, Ge, and III–V Layers by Controlled Spalling to Enable Low-Cost PV Technologies". In: *IEEE Journal of Photovoltaics* 2.2 (2012), pp. 141–147. DOI: 10.1109/JPHOTOV.2012.2184267.

[9] Stephen W. Bedell et al. "Layer transfer by controlled spalling". In: *Journal of Physics D: Applied Physics* 46.15 (Mar. 2013). DOI: 10.1088/0022-3727/46/15/152002. URL: https://iopscience.iop.org/article/10.1088/0022-3727/46/15/152002.

[10] L Bergeron et al. "Silicon-integrated telecommunications photon-spin interface". In: *PRX Quantum* 1.2 (2020), p. 020301.

[11] Eric Bersin et al. "Telecom Networking with a Diamond Quantum Memory". In: *PRX Quantum* 5 (1 Jan. 2024), p. 010303. DOI: 10.1103/PRXQuantum.5.010303. URL: https://link.aps.org/doi/10.1103/PRXQuantum.5.010303.

[12] Tom Bosma et al. "Identification and tunable optical coherent control of transition-metal spins in silicon carbide". In: *npj Quantum Information* 4.1 (2018), p. 48.

[13] Stefania Castelletto and Alberto Boretti. "Silicon carbide color centers for quantum applications". In: *Journal of Physics: Photonics* 2.2 (2020). DOI: 10.1088/2515-7647/ab77a2.

[14] Jie Chen and Corinne E. Packard. "Controlled spalling-based mechanical substrate exfoliation for III-V solar cells: A review". In: *Solar Energy Materials and Solar Cells* 225 (2021), p. 111018. ISSN: 0927-0248. DOI: https://doi.org/10.1016/j.solmat.2021.111018. URL: https://www.sciencedirect.com/science/article/pii/S0927024821000623.

[15] Pasquale Cilibrizzi et al. "Ultra-narrow inhomogeneous spectral distribution of telecom-wavelength vanadium centres in isotopically-enriched silicon carbide". In: *Nature Communications* 14 (8448 Dec. 2023). DOI: 10.1038/s41467-023-43923-7. URL: https://www.nature.com/articles/s41467-023-43923-7.

[16] Pasquale Cilibrizzi et al. "Ultra-narrow inhomogeneous spectral distribution of telecom-wavelength vanadium centres in isotopically-enriched silicon carbide". In: *Nature Communications* 14.1 (2023), p. 8448.

[17] Dustin Crouse et al. "Increased fracture depth range in controlled spalling of (100)-oriented germanium via electroplating". In: *Thin Solid Films* 649 (2018), pp. 154–159.

ISSN: 0040-6090. DOI: https://doi.org/10.1016/j.tsf.2018.01.031. URL: https://www.sciencedirect.com/science/article/pii/S0040609018300476.

[18] Andras Csore and Adam Gali. "Ab initio determination of pseudospin for paramagnetic defects in SiC". In: *Physical Review B* 102.24 (2020), p. 241201.

[19] A. M. Dibos et al. "Atomic Source of Single Photons in the Telecom Band". In: *Phys. Rev. Lett.* 120 (24 June 2018), p. 243601. DOI: 10.1103/PhysRevLett.120.243601. URL: https://link.aps.org/doi/10.1103/PhysRevLett.120.243601.

[20] Berk Diler et al. "Coherent control and high-fidelity readout of chromium ions in commercial silicon carbide". In: *NPJ quantum information* 6.1 (2020), p. 11.

[21] Anaıs Dréau et al. "Quantum Frequency Conversion of Single Photons from a Nitrogen-Vacancy Center in Diamond to Telecommunication Wavelengths". In: *Phys. Rev. Appl.* 9 (6 June 2018), p. 064031. DOI: 10.1103/PhysRevApplied.9.064031. URL: https://link.aps.org/doi/10.1103/PhysRevApplied.9.064031.

[22] Abram L. Falk. "Addressing spin states with infrared light". In: *Science* 357.6352 (2017), pp. 649–649. DOI: 10.1126/science.aan8807. eprint: https://www.science.org/doi/pdf/10.1126/science.aan8807. URL: https://www.science.org/doi/abs/10.1126/science.aan8807.

[23] Abram L. Falk et al. "Electrically and Mechanically Tunable Electron Spins in Silicon Carbide Color Centers". In: *Physical Review Letters* 112.187601 (2014). DOI: 10.1103/PhysRevLett.112.187601.

[24] Abram L. Falk et al. "Polytype control of spin qubits in silicon carbide". In: *Nature Communications* 4.1819 (2013). DOI: 10.1038/ncomms2854. URL: https://www.nature.com/articles/ncomms2854.

[25] Reyhaneh Ghassemizadeh et al. “Stability and electronic structure of NV centers at dislocation cores in diamond”. In: *Phys. Rev. B* 106 (17 Nov. 2022), p. 174111. DOI: 10.1103/PhysRevB.106.174111. URL: https://link.aps.org/doi/10.1103/PhysRevB.106.174111.

[26] Carmem M Gilardoni et al. “Hyperfine-mediated transitions between electronic spin-1/2 levels of transition metal defects in SiC”. In: *New Journal of Physics* 23.8 (2021), p. 083010.

[27] Carmem M Gilardoni et al. “Spin-relaxation times exceeding seconds for color centers with strong spin–orbit coupling in SiC”. In: *New Journal of Physics* 22.10 (2020), p. 103051.

[28] A. A. Golubov, M. Yu. Kupriyanov, and E. Il’ichev. “The current-phase relation in Josephson junctions”. In: *Rev. Mod. Phys.* 76 (2 Apr. 2004), pp. 411–469. DOI: 10.1103/RevModPhys.76.411. URL: https://link.aps.org/doi/10.1103/RevModPhys.76.411.

[29] BL Green et al. “Neutral silicon-vacancy center in diamond: Spin polarization and lifetimes”. In: *Physical Review Letters* 119.9 (2017), p. 096402.

[30] Jonathan A Gross. “Designing codes around interactions: The case of a spin”. In: *Physical Review Letters* 127.1 (2021), p. 010504.

[31] Xinghan Guo et al. “Microwave-Based Quantum Control and Coherence Protection of Tin-Vacancy Spin Qubits in a Strain-Tuned Diamond-Membrane Heterostructure”. In: *Physical Review X* 13.4 (2023), p. 041037.

[32] S. L. N. Hermans et al. “Qubit teleportation between non-neighbouring nodes in a quantum network”. In: *Nature* 605 (May 2022), pp. 663–668. DOI: 10.1038/s41586-022-04697-y. URL: https://www.nature.com/articles/s41586-022-04697-y.

[33] Daniel B Higginbottom et al. “Optical observation of single spins in silicon”. In: *Nature* 607.7918 (2022), pp. 266–270.

[34] Connor P. Horn et al. “Controlled Spalling of 4H Silicon Carbide with Investigated Spin Coherence for Quantum Engineering Integration”. In: *ACS Nano* (Oct. 2024). DOI: 10.1021/acsnano.4c10978. URL: https://pubs.acs.org/doi/10.1021/acsnano.4c10978.

[35] John W. Hutchinson. “Mixed mode fracture mechanics of interfaces”. In: *Metal-Ceramic Interfaces, Acta-Scripta Metallurgical Proceedings Series* 4 (1990), pp. 295–306.

[36] G. R. Irwin. “Fracture Dynamics,Fracturing of Metals”. In: *American Society for Metals* (1948), pp. 147–166.

[37] Kay D Jahnke et al. “Electron–phonon processes of the silicon-vacancy centre in diamond”. In: *New Journal of Physics* 17.4 (2015), p. 043011.

[38] Zhengzhi Jiang et al. “Quantum sensing of radio-frequency signal with NV centers in SiC”. In: *Science Advances* 9.20 (2023), eadg2080. DOI: 10.1126/sciadv.adg2080. eprint: https://www.science.org/doi/pdf/10.1126/sciadv.adg2080. URL: https://www.science.org/doi/abs/10.1126/sciadv.adg2080.

[39] B Kaufmann, A Dörnen, and FS Ham. “Crystal-field model of vanadium in 6H silicon carbide”. In: *Physical Review B* 55.19 (1997), p. 13009.

[40] H. J. Kimble. “The quantum internet”. In: *Nature* 453 (June 2008), pp. 1023–1030. DOI: 10.1038/nature07127. URL: https://www.nature.com/articles/nature07127.

[41] Marco Klotz et al. “Prolonged Orbital Relaxation by Locally Modified Phonon Density of States for the Si V- Center in Nanodiamonds”. In: *Physical Review Letters* 128.15 (2022), p. 153602.

[42] C. M. Knaut et al. "Entanglement of nanophotonic quantum memory nodes in a telecom network". In: *Nature* 629 (May 2024), pp. 573–578. DOI: 10.1038/s41586-024-07252-z. URL: https://www.nature.com/articles/s41586-024-07252-z.

[43] William F. Koehl et al. "Room temperature coherent control of defect spin qubits in silicon carbide". In: *Nature* 479 (2011), pp. 84–87. DOI: 10.1038/nature10562. URL: https://www.nature.com/articles/nature10562.

[44] M Kunzer, HD Müller, and U Kaufmann. "Magnetic circular dichroism and site-selective optically detected magnetic resonance of the deep amphoteric vanadium impurity in 6H-SiC". In: *Physical Review B* 48.15 (1993), p. 10846.

[45] Kazuhiro Kuruma et al. "Engineering phonon-qubit interactions using phononic crystals". In: *arXiv preprint arXiv:2310.06236* (2023).

[46] Ning Li et al. "Single Crystal Flexible Electronics Enabled by 3D Spalling". In: *Advanced Materials* 29.18 (2017), p. 1606638. DOI: https://doi.org/10.1002/adma.201606638. eprint: https://onlinelibrary.wiley.com/doi/pdf/10.1002/adma.201606638. URL: https://onlinelibrary.wiley.com/doi/abs/10.1002/adma.201606638.

[47] Daniil M Lukin et al. "4H-silicon-carbide-on-insulator for integrated quantum and nonlinear photonics". In: *Nature Photonics* 14.5 (2020), pp. 330–334.

[48] Smarak Maity et al. "Coherent acoustic control of a single silicon vacancy spin in diamond". In: *Nature Communications* 11.193 (2020). DOI: 10.1038/s41467-019-13822-x.

[49] Srujan Meesala et al. "Strain engineering of the silicon-vacancy center in diamond". In: *Phys. Rev. B* 97.205444 (2018). DOI: 10.1103/PhysRevB.97.205444.

[50] Cathryn P Michaels et al. "Multidimensional cluster states using a single spin-photon interface coupled strongly to an intrinsic nuclear register". In: *Quantum* 5 (2021), p. 565.

[51] WC Mitchel et al. "Vanadium donor and acceptor levels in semi-insulating 4H-and 6H-SiC". In: *Journal of applied physics* 101.1 (2007).

[52] R Orbach. "Spin-lattice relaxation in rare-earth salts". In: *Proceedings of the Royal Society of London. Series A. Mathematical and Physical Sciences* 264.1319 (1961), pp. 458–484.

[53] Salim Ourari et al. "Indistinguishable telecom band photons from a single Er ion in the solid state". In: *Nature* 620.7976 (2023), pp. 977–981.

[54] E. Papanasam et al. "A Comprehensive Review of Recent Progress, Prospect and Challenges of Silicon Carbide and its Applications". In: *Silicon* 14 (2022), pp. 12887–12900. DOI: 10.1007/s12633-022-01998-9.

[55] Honghwi Park et al. "Layer-resolved release of epitaxial layers in III-V heterostructure via a buffer-free mechanical separation technique". In: *Science Advances* 8.3 (2022), eabl6406. DOI: 10.1126/sciadv.abl6406. eprint: https://www.science.org/doi/pdf/10.1126/sciadv.abl6406. URL: https://www.science.org/doi/abs/10.1126/sciadv.abl6406.

[56] Ryan A Parker et al. "A diamond nanophotonic interface with an optically accessible deterministic electronuclear spin register". In: *Nature Photonics* (2023), pp. 1–6.

[57] William D. Phillips. "Nobel Lecture: Laser cooling and trapping of neutral atoms". In: *Rev. Mod. Phys.* 70 (3 July 1998), pp. 721–741. DOI: 10.1103/RevModPhys.70.721. URL: https://link.aps.org/doi/10.1103/RevModPhys.70.721.

[58] Benjamin Pingault et al. "Coherent control of the silicon-vacancy spin in diamond". In: *Nature Communications* 8.1 (2017), p. 15579.

[59] William H. Safranek and H. Reed Alan. "The Properties of Electrodeposited Metals and Alloys. A Handbook". In: *Journal of The Electrochemical Society* 122 (1975). DOI:

10.1149/1.2134416. URL: https://iopscience.iop.org/article/10.1149/1.2134416/pdf.

[60] M. Schlesinger and M. Paunovic. *Modern Electroplating*. John Wiley Sons, Ltd, 2010. ISBN: 9780470602638. DOI: https://doi.org/10.1002/9780470602638. eprint: https://onlinelibrary.wiley.com/doi/pdf/10.1002/9780470602638. URL: https://onlinelibrary.wiley.com/doi/abs/10.1002/9780470602638.

[61] Xu She et al. "Review of Silicon Carbide Power Devices and Their Applications". In: *IEEE Transactions on Industrial Electronics* 64.10 (2017), pp. 8193–8205. DOI: 10.1109/TIE.2017.2652401.

[62] KN Shrivastava. "Theory of spin–lattice relaxation". In: *physica status solidi (b)* 117.2 (1983), pp. 437–458.

[63] Young-Ik Sohn et al. "Controlling the coherence of a diamond spin qubit through its strain environment". In: *Nature Communications* 9.1 (2018), p. 2012.

[64] L. Spindlberger et al. "Optical Properties of Vanadium in 4H Silicon Carbide for Quantum Technology". In: *Phys. Rev. Appl.* 12 (1 July 2019), p. 014015. DOI: 10.1103/PhysRevApplied.12.014015. URL: https://link.aps.org/doi/10.1103/PhysRevApplied.12.014015.

[65] P-J Stas et al. "Robust multi-qubit quantum network node with integrated error detection". In: *Science* 378.6619 (2022), pp. 557–560.

[66] Zhigang Suo and John W. Hutchinson. "Steady-state cracking in brittle substrates beneath adherent films". In: *International Journal of Solids and Structures* 25.11 (1989), pp. 1337–1353. ISSN: 0020-7683. DOI: https://doi.org/10.1016/0020-7683(89)90096-6. URL: https://www.sciencedirect.com/science/article/pii/0020768389900966.

[67] Cassi A. Sweet et al. “Controlled exfoliation of (100) GaAs-based devices by spalling fracture”. In: *Applied Physics Letters* 108.1 (Jan. 2016), p. 011906. ISSN: 0003-6951. DOI: 10.1063/1.4939661. eprint: https://pubs.aip.org/aip/apl/article-pdf/doi/10.1063/1.4939661/12853514/011906_1_online.pdf. URL: https://doi.org/10.1063/1.4939661.

[68] Benedikt Tissot and Guido Burkard. “Hyperfine structure of transition metal defects in SiC”. In: *Physical Review B* 104.6 (2021), p. 064102.

[69] Benedikt Tissot and Guido Burkard. “Spin structure and resonant driving of spin-1/2 defects in SiC”. In: *Physical Review B* 103.6 (2021), p. 064106.

[70] Benedikt Tissot et al. “Nuclear spin quantum memory in silicon carbide”. In: *Physical Review Research* 4.3 (2022), p. 033107.

[71] Benedikt Tissot et al. “Strain engineering for transition-metal defects in SiC”. In: *Physical Review B* 109.5 (2024), p. 054111.

[72] Matthew E Trusheim et al. “Transform-limited photons from a coherent tin-vacancy spin in diamond”. In: *Physical Review Letters* 124.2 (2020), p. 023602.

[73] HJ Von Bardeleben et al. “Transition metal qubits in 4 H-silicon carbide: A correlated EPR and DFT study of the spin S= 1 vanadium V 3+ center”. In: *Physical Review Materials* 3.12 (2019), p. 124605.

[74] Samuel J Whiteley et al. “Spin–phonon interactions in silicon carbide addressed by Gaussian acoustics”. In: *Nature Physics* 15.5 (2019), pp. 490–495.

[75] Gary Wolfowicz et al. “Optical charge state control of spin defects in 4H-SiC”. In: *Nature Communications* 8.1 (2017), p. 1876.

[76] Gary Wolfowicz et al. “Quantum guidelines for solid-state spin defects”. In: *Nature Review Materials* 6 (Oct. 2021), pp. 906–925. DOI: 10.1038/s41578-021-00306-y. URL: https://www.nature.com/articles/s41578-021-00306-y.

[77] Gary Wolfowicz et al. “Vanadium spin qubits as telecom quantum emitters in silicon carbide”. In: *Science Advances* 6.18 (2014). DOI: 10.1126/sciadv.aaz1192.

[78] H.-H. Yu, M.Y. He, and J.W. Hutchinson. “Edge effects in thin film delamination”. In: *Acta Materialia* 49.1 (2001), pp. 93–107. ISSN: 1359-6454. DOI: https://doi.org/10.1016/S1359-6454(00)00293-7. URL: https://www.sciencedirect.com/science/article/pii/S1359645400002937.